8-12-2016

Exoplanets in Open Clusters and Binaries: New Constraints on Planetary Migration

Samuel N. Quinn
Georgia State University

EXOPLANETS IN OPEN CLUSTERS AND BINARIES:
NEW CONSTRAINTS ON PLANETARY MIGRATION

by

SAMUEL NOAH QUINN

Under the Direction of Russel J. White

ABSTRACT

In this dissertation, we present three complementary studies of the processes that drive planetary migration. The first is a radial-velocity survey in search of giant planets in adolescent ($< 1\,\mathrm{Gyr}$) open clusters. While several different mechanisms may act to drive giant planets inward, only some mechanisms will excite high eccentricities while doing so. Measuring the eccentricities of young hot Jupiters in these clusters (at a time before the orbits have had a chance to circularize due to tidal friction with their host stars) will allow us to identify which mechanisms are most important. Through this survey, we detect the first 3 hot Jupiters in open clusters (and at least 4 long-period planets), and we measure the occurrence rate of hot Jupiters in clusters to be similar to that of the field ($\sim$1%). We determine via analyses of hot

Jupiter eccentricities and outer companions in these systems that high eccentricity migration mechanisms (those requiring the presence of a third body) are important for migration. The second project, an adaptive optics imaging survey for stellar companions to known hot Jupiter hosts, aims to determine the role that stellar companions in particular play in giant planet migration. Through a preliminary analysis, we derive a lower limit on the binary frequency of 45% (greater than that of the typical field star), and we find that the presence of a companion is correlated with misalignment of the spin-orbit angle of the planetary system, as would be expected for stellar Kozai-Lidov migration: at least 74% of misaligned systems reside in binaries. We thus conclude that among high eccentricity migration mechanisms, those requiring a stellar companion play a significant role. Finally, we describe simulations of measurements of the planet population expected to be discovered by TESS, and use these to demonstrate that a strong constraint on the obliquity distribution of small planets can be derived using only TESS photometry, Gaia astrometry, and $v \sin i_\star$ measurements of the host stars. This obliquity distribution will be a key piece of evidence to help detemine the likely formation and migration histories of small planets, and can contribute to the assessment of the potential for Earth-like planets to harbor life.

INDEX WORDS: planets and satellites: detection, planets and satellites: dynamical evolution and stability, planets and satellites: formation, planet-star interactions, open clusters, binaries: close

EXOPLANETS IN OPEN CLUSTERS AND BINARIES: NEW CONSTRAINTS ON PLANETARY MIGRATION

by

SAMUEL NOAH QUINN

A Dissertation Submitted in Partial Fulfillment of the Requirements for the Degree of

Doctor of Philosophy

in the College of Arts and Sciences

Georgia State University

2016

EXOPLANETS IN OPEN CLUSTERS AND BINARIES:
NEW CONSTRAINTS ON PLANETARY MIGRATION

by

SAMUEL NOAH QUINN

Committee Chair:	Russel J. White
Committee:	David W. Latham
	Douglas R. Gies
	Sebastien Lepine
	Joshua Von Korff

Electronic Version Approved:

Office of Graduate Studies

College of Arts and Sciences

Georgia State University

August 2016

DEDICATION

This dissertation is dedicated to my wife, Larissa, for exhibiting unmatched patience during all the times when I enthusiastically—and long-windedly—described my work, for taking enough interest in those expositions that she can now give my elevator pitch at parties, for supporting and encouraging me even when my work interfered with our family time, and for always having my back. Larissa, other astronomers may know you best as an irregular rubble pile orbiting Neptune, but to me, you're so much more.

I also dedicate this disseration to my daughter, Madeleine, for being the most joy-filled distraction from work I could ever imagine.

I love you both!

ACKNOWLEDGMENTS

I would also like to thank:

My advisor, Dr. Russel White, for his mentorship, good discussions, scientific perspective, and friendship, and for his expert guidance in helping me find my way through graduate school—and to some good places to take a break in the city of Atlanta.

Dr. David Latham, for recognizing and fostering my potential as a scientist, for his immeasurable influence on my approach to science, for his advocacy and support, for serving as an exemplary role model and mentor, and for taking responsibility for my early education in wine.

The other members of my committee—Dr. Douglas Gies, Dr. Sebastien Lepine, and Dr. Joshua Von Korff—for discussion, support, advice, and of course, their time so generously donated.

My fellow graduate students, for soldiering on with me while hidden away in Kell Hall, while laboring through the qualifying exams, and while battling gridlock at HLCO public nights.

And last but not least, my many scientific collaborators not yet mentioned, without whom there would simply be no dissertation.

TABLE OF CONTENTS

LIST OF TABLES

LIST OF FIGURES

CHAPTER 1
INTRODUCTION & MOTIVATION

For many years, our theories of planet formation were informed largely by the only planetary system of which we knew—our own Solar System. When the first exoplanets (planets orbiting stars other than the Sun) were discovered more than two decades ago, their properties immediately hinted at the diversity of planetary systems produced in nature. These early discoveries—a very massive gas giant (HD 114762 b; Latham et al. 1989), planets orbiting pulsars (PSR1257+12 bc; Wolszczan & Frail 1992), and a Jupiter-sized planet that orbits close to its star with a period of only 4.23 days (51 Peg b; Mayor & Queloz 1995)—were vastly different from the planets in the Solar System. Subsequent planet searches have further revealed the diversity of planetary systems, including rich populations of short-period super-Earths in multi-planet systems (e.g., Latham et al. 2011; Batalha et al. 2013), circumbinary planets (e.g., Doyle et al. 2011), closely spaced planets near orbital resonances (e.g., Carter et al. 2012), planets orbiting giant stars (Jones et al. 2014), massive directly-imaged planets on very wide orbits (e.g., Marois et al. 2008, 2010; Kuzuhara et al. 2013), free-floating planets (e.g., Luhman 2014), and many more. While some of these planets are compatible with existing formation theory, many require additional explanation. In this way, our understanding of the planet formation process has become more complete as the field of exoplanets has blossomed, often spurred along by having to explain previously unobserved classes of planets.

One of the major realizations to emerge from the study of exoplanets was that planets

often migrate after formation. This became clear soon after the discovery of the first short period giant planet (or "hot Jupiter"). Hot Jupiters occupy a region of orbital space ($a \lesssim 0.1\,\mathrm{AU}$) in which the protoplanetary disk has a low surface density and a temperature that is too high for the survival of ices and volatiles (Boss 1998), which are critical for the accretion of a massive core (Kennedy & Kenyon 2008). These planets are therefore presumed to have formed beyond the ice line (located at several AU for a Sun-like star; Martin & Livio 2013) and subsequently migrated inward. While the existence of hot Jupiters was not a complete surprise (see, for example, the brief but prescient discussion of transiting hot Jupiters by Struve 1952), only after their discovery was significant effort dedicated to explaining the mechanism by which they migrate. Possible mechanisms include "Type II" migration (through a gas disk; Lin & Papaloizou 1986), planet-planet scattering (Rasio & Ford 1996), Kozai-Lidov cycles (Kozai 1962; Lidov 1962; Fabrycky & Tremaine 2007) and the eccentric Kozai-Lidov effect (Naoz 2016), or secular chaos (Wu & Lithwick 2011). Type II migration operates when a giant planet clears a gap in the protoplanetary disk and migrates inward on the viscous diffusion timescale of the disk. Planet-planet scattering occurs when, as the name implies, two planets experience a close approach and gravitationally scatter, sending one planet toward the host star on a highly eccentric orbit with pericenter close enough to the star to cause the orbit to tidally decay and circularize. Kozai-Lidov cycles describe the process of periodic exchange of eccentricity and inclination of the orbit due to interaction with a distant, massive, inclined companion (a star or planet). Similar to planet-planet scattering, when the inner planet reaches a high eccentricity with a small pericenter

distance, the orbit shrinks and circularizes via tidal friction. Secular chaos can occur in multiple planet systems, causing a gradual increase in the eccentricity of the inner planet as the sytem drifts toward equipartition of angular momentum deficit. As in other mechanisms, the highly eccentric planet circularizes via tides. These can therefore be broadly classified into two categories: gentle Type II disk migration, which is generally expected to preserve low-eccentricity orbits; and processes involving additional massive bodies, which are expected to excite high eccentricities (and inclinations) before tidal interaction with the host star at periastron passage shrinks and circularizes the orbit. Consequently, the latter processes are often collectively referred to as high eccentricity migration (HEM).

Understanding the orbital evolution of giant planets is important for planetary systems more generally, as the orbits of giant planets can strongly sculpt the architectures of smaller planets. In our own Solar System, Jupiter accounts for about 71% of the planetary mass and about 60% of the total angular momentum. Had Jupiter migrated inward to the Sun, it surely would have disrupted the terrestrial planets, and our Solar System would have been unlikely to host a habitable planet. It is also prudent to bear in mind that the importance of giant planet migration for terrestrial planets goes beyond catastrophic scattering events, and may represent a relatively common influence in the final properties of terrestrial planets. It has been suggested based on simulations of the early Solar System that Jupiter did migrate inward briefly — sculpting the population of small bodies in the inner Solar System and dictating the subsequent growth of the terrestrial planets — before retreating to its current position (the so-called "Grand Tack" model; Walsh et al. 2011). Even modest migration of

giant planets (or lack thereof) can therefore drastically affect the properties of potentially habitable worlds. Of course, giant planets need not migrate inward; the particular properties of the planet and gas disk may result in outward migration or no migration at all. The detailed characterization of giant planet migration can thus be used to help us understand the likely properties of potentially habitable terrestrial worlds. This is particularly relevant as the next generation of planet searches begins to discover them in greater numbers.

There are many ways in which one might attempt to characterize the importance of migration mechanisms. While Type II and HEM predict different properties for newly established hot Jupiters, we expect many of these differences to be erased over time by tidal interaction with the host stars. Initially eccentric orbits produced via HEM will circularize for short period planets, and initially inclined orbits may realign with the stellar spin. Therefore, one way to evaluate migration mechanisms is to compare the properties of young hot Jupiters, before subsequent interactions obfuscate the original system properties. Unfortunately, searches for hot Jupiters orbiting the youngest stars ($\lesssim$ 10-20 Myr) have been inhibited by their rapid rotation and activity (Bailey et al. 2012; Crockett et al. 2012). Although at least one promising candidate has been identified (PTFO 8-85961; van Eyken et al. 2012; Barnes et al. 2013), it was later shown to be a likely false positive (Yu et al. 2015). As a result of these difficulties, most known planets are much too old to expect the initial orbits to remain unchanged.

Instead, some authors have attempted to take large populations of older planets and account for the expected effect of tidal interactions. Albrecht et al. (2012b), for example,

find that while most hot Jupiters orbiting cool stars are well-aligned with the stellar spin axis, those orbiting hot stars possess a wide range of obliquities. The authors suggest that most hot Jupiters initially occupy non-zero obliquities, but because of the short tidal timescale of cool stars, those systems are able to re-align. This result would favor HEM as an important mechanism for giant planet migration. On the other hand, Socrates et al. (2012) point out that planets undergoing HEM should, for a time, possess extreme eccentricities, so one can predict the number of such super-eccentric planets that should be detected. Dawson et al. (2015) find that among the *Kepler* sample, there is a paucity of such systems, and they place an upper limit of $\sim$44% on the fraction of hot Jupiters formed via the star-planet Kozai mechanism. They conclude that either planet-planet interactions or disk migration could be responsible for the remaining systems. Other authors have demonstrated that simulations can be used in a complementary manner to generate planetary systems via one particular migration channel and compare the properties of such planets to observed populations. In this way, Naoz et al. (2012) find that the Kozai mechanism can account for about 30% of hot Jupiters. Thus far, we have considered only the properties of the planets themselves, but it is important to note that planetary systems will not, in general, only consist of a single star and and single planet; Type II and HEM differ not just in predicted properties of a migrating planet, but also in the predicted architecture of the system as a whole. HEM requires the presence of a massive outer body (be it a star or a planet), so the architectures of hot Jupiter systems can also help constrain the mechanisms by which they migrate. For example, in their survey for outer companions in hot Jupiter systems, Knutson et al. (2014)

and Ngo et al. (2015) find that $72\% \pm 16\%$ of hot Jupiters are part of multi-planet and/or multi-star systems. However, while the stellar companion fraction is slightly larger than for typical field stars, they find no correlation between the presence of stellar companions and the misalignment of hot Jupiter orbits and are therefore unable to confidently ascribe hot Jupiter migration to the Kozai mechanism. Larger samples may help this effort.

In this dissertation, I will describe three complementary projects aimed at constraining planetary migration processes. The first, a radial-velocity survey for giant planets in nearby open clusters, will take advantage of the young ages of these stars to characterize planetary properties and system architectures that have not yet been affected significantly by post-migration evolution. The properties of such planets can quantify the relative importance of HEM and disk migration. The selection of targets and the survey design are discussed in Chapters 2 and 3, and results and discussion are presented in Chapters 4 through 6. The second, an adaptive optics imaging search for stellar companions to known hot Jupiter host stars, will provide a census of system architectures in order to determine the importance of the Kozai mechanism. This survey is described in Chapter 7. The third project is a simulation that demonstrates a technique to characterize the obliquity distribution of planets discovered by the upcoming NASA TESS mission. Many small planets are expected to be included in this sample, so this latter project is not limited to giant planets. Building upon the legacy of *Kepler*, which has enabled some of the first observational constraints on the formation and migration histories of small planets, we move toward a more complete description of planet formation and migration at all sizes. As larger populations of potentially habitable

Earth-like planets are discovered, this work can help assess their potential to harbor life. This project is described in Chapter 8.

CHAPTER 2

SELECTION OF OPEN CLUSTERS AND THE STELLAR SAMPLE

2.1 The Observational Challenges Associated with a Precision RV Survey of Open Cluster Stars

While a survey for planets in young open clusters may produce benchmark planetary systems and contribute important constraints to planetary migration theory, there are practical challenges to observing young cluster stars that do not affect surveys of old field stars. Understanding these limitations is important for designing a successful survey.

The first challenge of an open cluster survey is that the selection of nearby clusters is limited. While traditional RV surveys have had access to thousands of bright, nearby stars, open cluster stars will be, on average, much farther away and thus much fainter for a given type of star. In practical terms, this type of survey will require larger or more efficient telescopes, or more telescope time. Alternatively, it will limit the number of targets that can be surveyed or will restrict observations to the brighter, more massive stars.

Also of note is that an open cluster subtends only a small angle on the sky, and all members of a cluster will therefore only be observable for a (sometimes small) fraction of a night at many times of the year. In contrast with field star surveys, for which at least one target is almost always near the meridian and for which classical time allocations of several consecutive days is well-suited to the survey, open cluster surveys may require more flexibility in scheduling observations. A queue schedule, in which targets can be observed throughout the year when visible and whenever a new observation is needed to improve the

phase coverage of an orbit, rather than in a single contiguous block of allocated time, would be better suited for an open cluster survey.

Besides the practical considerations of telescope scheduling and time allocation, there are serveral observational challenges to overcome, arising from the physical properties of cluster stars. For example, because the stellar space density in open clusters is higher than in the rest of the Solar neighborhood, we can expect an elevated incidence of close visual companions. If the light from these companions enters the slit or fiber, the spectral lines of these nearby stars can prevent the accurate derivation of precise RVs. Worse still, it might not be immediately apparent that there is a second star present if the two stars have a similar radial velocity and the lines are heavily blended. (This is expected to often be the case for two cluster members, which will share the space motion of the cluster as a whole.) To minimize this contamination, high-resolution imaging can be used to remove close visual binaries from the sample.

Finally, the main reason young stars are typically excluded from planet surveys is that youth is associated with rapid rotation and enhanced magnetic activity, which manifests as a greater incidence of surface inhomogeneities like spots, plages and faculae. Rapid rotation by itself adversely affects RV precision, as rotationally broadened spectral lines make the identification of the line centers more difficult (see, e.g., Beatty & Gaudi 2015). More importantly for active young stars, as the star rotates, the disappearance and reappearance of surface features modulates the spectral line shapes, which results in an apparent shift in the line centers (and thus the derived RVs). A rotating dark spot, for example, first

blocks the blue-shifted limb of the star and then the red-shifted limb, periodically resulting in apparent redshifts and blueshifts. In this way, a spot can be mistaken for an orbiting planet (e.g., Queloz et al. 2001). While such a scenario can be identified through careful analysis of the line shapes and stellar activity and/or follow-up observations, the efficacy of such indicators will depend on instrument resolution and the quality and quantity of the data. When the observational sampling is not good enough, or the measurements aren't precise enough, or the star has many active surface regions, or those regions are variable on short timescales, a single periodicity may be hard to identify and the RVs will simply exhibit a scatter beyond the expected measurement errors. This excess stellar "jitter" is a hallmark of young stars, and effectively degrades measurement precision, making planet detection much more difficult in such systems.

2.2 Selection of Optimal Clusters

Given the above considerations, we should aim to observe clusters that maximize our expected observational success and, ultimately, the planet yield. Our ideal clusters will therefore be nearby — we choose $d < 200\,\mathrm{pc}$ because beyond this distance, Solar-type stars become too faint for modestly sized telescopes to survey in reasonable time allocations — and will be well-studied by previous surveys to confirm cluster membership and establish stellar properties (e.g., spectral type, multiplicity, and rotational velocity). They will also be young ($\lesssim 1\,\mathrm{Gyr}$) so that planet discoveries can provide insight into the early evolution of planetary systems, but not so young ($\lesssim 100\,\mathrm{Myr}$) that stellar jitter would be expected to be

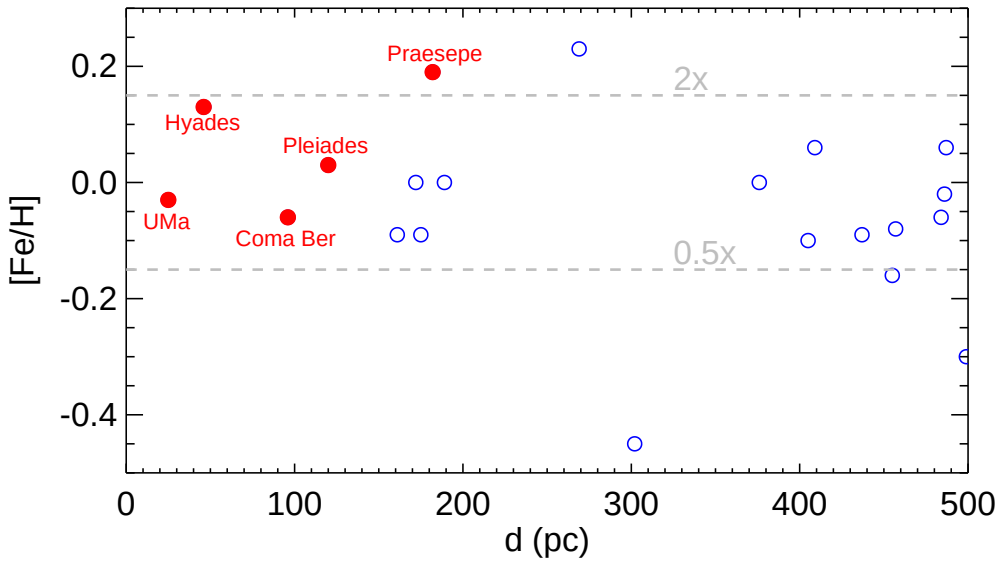

Figure 2.1 The metallicities of nearby open clusters plotted against their distance from the Sun. Horizontal dashed lines indicate the expected enhancement of the giant planet occurrence rate according to the relation derived by Fischer & Valenti (2005). Red circles indicate clusters that pass our selection criteria of $100 \lesssim t \lesssim 1000\,\mathrm{Myr}$ and $d < 200\,\mathrm{pc}$.

similar in magnitude to the orbital amplitudes of giant planets (many tens of $\mathrm{m\,s^{-1}}$ or more; e.g., Paulson & Yelda 2006); we refer to these as adolescent age clusters. Finally, there is a well-documented correlation between stellar metallicity and giant planet occurrence (e.g., Fischer & Valenti 2005), so we should expect that clusters with high metallicities will host more giant planets.

Figure 2.1 shows the clusters near the Sun plotted as a function of approximate distance and metallicity. The best targets for our survey — nearby and metal-rich — reside towards the top and the left of the plot. Among these, the clusters that also satisfy our age requirement ($100 \lesssim t \lesssim 1000\,\mathrm{Myr}$) are Praesepe, the Hyades, Coma Berenices, the Pleiades, and the Ursa Major moving group. We list basic properties of these clusters in Table 2.1, and

describe them in the following sections. Members of these clusters will comprise the parent sample from which we will select our final survey targets.

Table 2.1: Properties of Open Clusters

Cluster	Distance[1] (pc)	Age (Myr)	[Fe/H] (dex)
Praesepe	182	580[2]	+0.19[6]
Hyades	46	625[3]	+0.13[7]
Coma Berenices	87	590[4]	−0.06[8]
Ursa Major Moving Group	$\lesssim 25$	450[5]	−0.03[9]

Note — The source of each measurement is as follows: (1) van Leeuwen (2009); (2) Delorme et al. (2011); (3) Perryman et al. (1998); (4) Collier Cameron et al. (2009); (5) King et al. (2003), Jones et al. (2015); (6) Quinn et al. (2012); (7) Paulson et al. (2003); (8) Boesgaard et al. (2003); (9) Ammler-von Eiff & Guenther (2009)

2.3 The Stellar Sample

To select the target stars for our survey, we take advantage of previous photometric, spectroscopic and high spatial resolution imaging studies of these clusters, with the goal of observing only bright, slowly rotating, bona fide cluster members without known binary companions. We note that while our primary goal is to detect planets, our observations can contribute to characterization of the stellar populations of the clusters surveyed, including their (projected) rotations, activity levels, cluster membership, and binarity.

2.3.1 Praesepe Stars

Praesepe is a nearby ($\sim$182 pc;) open cluster with approximately 1000 identified probable members (Kraus & Hillenbrand 2007), a well-determined age ($\sim$600 Myr; Hambly et al. 1995;

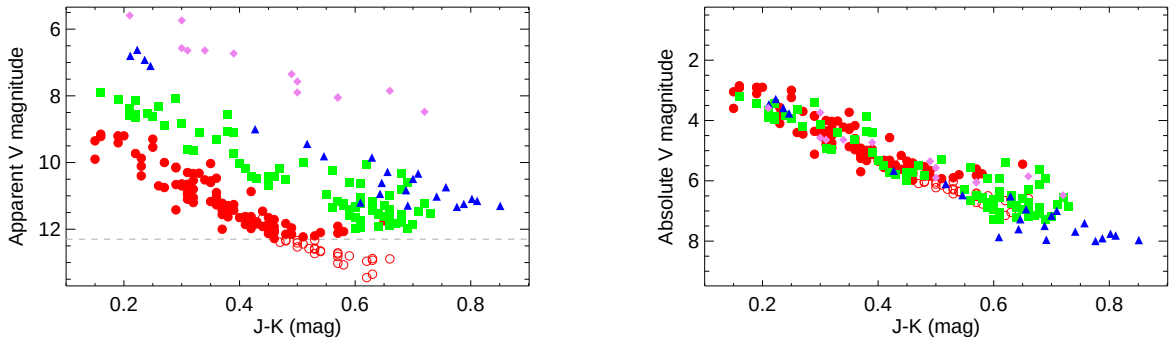

Figure 2.2 *Left*: The CMD of Praesepe (red circles), Coma Berenices (green squares), Hyades (blue triangles), and Ursa Major (violet diamonds) stars included in our survey. We plot the apparent V magnitudes against the $J - K$ colors (except for Ursa Major, for which we plot $M_{\rm bol} + 2$, because its intrinsic distance spread causes large scatter in the color-apparent magnitude sequence). We also show fainter Praesepe stars (red open circles) that we will observe once as reconnaissance for a inclusion in a deeper survey. *Right*: Same as the left, but this time with absolute magnitudes, calculated using the cluster distances given by van Leeuwen (2009), and bolometric magnitudes in Ursa Major, as reported by Ammler-von Eiff & Guenther (2009). In both plots, it is clear that the stellar populations being surveyed are different in each cluster, due (at least) to our magnitude cutoff and the fact that most Hyades stars have already been surveyed.

Kraus & Hillenbrand 2007; An et al. 2007; Gáspár et al. 2009; Delorme et al. 2011), and significantly elevated metallicity ([Fe/H] $= +0.27 \pm 0.10$ dex, Pace et al. 2008; [Fe/H] $= +0.11 \pm 0.03$, An et al. 2007). A metallicity as high as +0.27 dex would imply an increase in giant planet frequency of a factor of nearly 4 relative to solar metallicity (out to orbital periods of at least 4 years; Fischer & Valenti 2005).

In Praesepe, we drew our sample from the Kraus & Hillenbrand (2007) membership list, for which membership probabilities were calculated on the basis of proper motions and positions in an H-R diagram (for which stellar properties were derived via SED fits to literature photometry). From this list, we excluded stars with close visual companions ($< 2\farcs5$) identified by Bouvier et al. (2001) and Patience et al. (2002), as well as spectroscopic

binaries identified by Mermilliod et al. (2009). To enable precise RVs and practical telescope time requests, we also rejected stars with $V > 12.3$ (corresponding to a spectral type of about K0V), or for which $v \sin i_\star$ had previously been measured to be greater than $30\,\mathrm{km\,s^{-1}}$. We did include stars without previously published $v \sin i_\star$ measurements that meet the rest of our criteria, with the intention of obtaining an initial spectrum to assess their rotational velocities before surveying them in earnest. These stars are shown (along with those from other clusters) on a color-magnitude diagram (CMD) in Figure 2.2. In addition to these stars, we obtained single spectra of low probability members to confirm their membership status, as well as a number of fainter stars as reconnaissance for a potential expanded survey of fainter Praesepe stars. A list of all of these stars is provided in Table 2.2.

Table 2.2: Praesepe Target List

Name	2MASS	RA	DEC	V	J	K	J-K
Pr0009	J08282095+1950386	127.0872753	+19.8440595	10.60	9.780	9.427	0.353
Pr0014	J08295363+2226322	127.4734465	+22.4422948	9.90	8.939	8.781	0.158
Pr0017	J08305546+1933197	127.7310989	+19.5554781	10.55	9.725	9.369	0.356
Pr0021	J08312172+2202512	127.8405106	+22.0475856	10.54	9.557	9.231	0.326
Pr0024	J08321507+1813425	128.0627989	+18.2284637	11.10	9.975	9.663	0.312
Pr0035	J08332733+1634472	128.3638533	+16.5797945	10.70	9.120	8.819	0.301
Pr0036	J08334227+2015094	128.4261095	+20.2526303	10.52	9.428	9.079	0.349
Pr0044	J08345963+2105492	128.7484456	+21.0969970	11.20	10.012	9.684	0.328
Pr0047	J08351780+1938101	128.8241927	+19.6361842	11.83	10.497	10.012	0.485
Pr0051	J08355455+1808577	128.9772945	+18.1493570	10.89	9.757	9.445	0.312
Pr0058	J08362782+1754535	129.1159018	+17.9148703	10.96	9.720	9.405	0.315
Pr0062	J08364003+2036352	129.1667853	+20.6097964	11.86	10.492	10.077	0.415
Pr0065	J08364572+2007262	129.1905118	+20.1239470	11.65	10.340	9.938	0.402
Pr0076	J08371148+1948132	129.2978586	+19.8036784	11.29	10.075	9.686	0.389
Pr0079	J08371829+1941564	129.3262100	+19.6989962	11.44	10.175	9.802	0.373
Pr0081	J08372222+2010373	129.3426148	+20.1770150	11.40	10.187	9.803	0.384
Pr0084	J08372755+1937033	129.3647953	+19.6175653	11.65	10.252	9.806	0.446
Pr0085	J08372793+1933451	129.3664192	+19.5625448	9.30	8.717	8.464	0.253
Pr0086	J08372819+1909443	129.3674812	+19.1623387	9.54	8.657	8.400	0.257
Pr0092	J08374660+1926181	129.4442086	+19.4383384	10.65	9.591	9.276	0.315
Pr0093	J08374739+1906247	129.4474662	+19.1068762	12.28	10.666	10.202	0.464
Pr0095	J08375208+1959138	129.4670286	+19.9871773	11.26	10.079	9.689	0.390
Pr0096	J08375703+1914103	129.4876409	+19.2362167	11.84	10.470	10.038	0.432
Pr0098	J08380808+2026223	129.5336853	+20.4395417	11.72	10.358	9.932	0.426
Pr0100	J08381497+2034041	129.5624077	+20.5678325	11.45	10.106	9.717	0.389
Pr0107	J08384447+1748294	129.6852898	+17.8081956	12.00	10.519	10.144	0.375
Pr0115	J08390523+2007018	129.7718056	+20.1171698	9.41	8.603	8.413	0.190
Pr0119	J08391096+1810335	129.7956974	+18.1759906	10.30	9.307	8.994	0.313
Pr0120	J08391217+1906561	129.8007274	+19.1156117	10.14	9.555	9.258	0.297
Pr0121	J08392155+2045293	129.8397889	+20.7581381	11.86	10.476	10.026	0.450

Name	2MASS	RA	DEC	V	J	K	J-K
Pr0123	J08392498+1927336	129.8540892	+19.4593542	10.47	9.357	8.997	0.360
Pr0125	J08393042+2004087	129.8767565	+20.0690534	10.32	9.140	8.807	0.333
Pr0126	J08393203+2039203	129.8834998	+20.6556556	12.07	10.360	9.771	0.589
Pr0128	J08393553+1852367	129.8980833	+18.8768762	10.80	9.657	9.329	0.328
Pr0133	J08394575+1922011	129.9406333	+19.3669900	10.64	9.565	9.259	0.306
Pr0135	J08394960+1820506	129.9566474	+18.3474267	9.15	8.436	8.279	0.157
Pr0136	J08395084+1933020	129.9618124	+19.5505748	11.84	10.421	9.996	0.425
Pr0138	J08395506+2003541	129.9794315	+20.0650248	10.11	9.199	8.961	0.238
Pr0143	J08400171+1859595	130.0070948	+18.9998417	10.03	9.053	8.698	0.355
Pr0147	J08400771+2103458	130.0321136	+21.0627298	9.21	8.541	8.347	0.194
Pr0149	J08400968+1937170	130.0403403	+19.6214264	11.98	10.556	10.133	0.423
Pr0157	J08402743+1916409	130.1143324	+19.2780381	11.17	10.012	9.655	0.357
Pr0160	J08403169+1951010	130.1320256	+19.8502864	11.63	10.294	9.911	0.383
Pr0162	J08403347+1938009	130.1394353	+19.6336014	12.20	10.706	10.169	0.537
Pr0163	J08403357+2118547	130.1398648	+21.3151864	11.56	10.467	10.097	0.370
Pr0164	J08403360+1840282	130.1399977	+18.6744903	11.62	10.249	9.832	0.417
Pr0165	J08403623+2133421	130.1509724	+21.5617164	11.64	10.386	9.974	0.412
Pr0168	J08403992+1940092	130.1663271	+19.6692203	10.87	9.610	9.189	0.421
Pr0169	J08404248+1933576	130.1770000	+19.5660073	11.34	10.091	9.706	0.385
Pr0172	J08404761+1854119	130.1983974	+18.9033164	11.46	10.126	9.686	0.440
Pr0173	J08404832+1955189	130.2013406	+19.9219131	11.03	9.864	9.507	0.357
Pr0174	J08405487+1956067	130.2286315	+19.9351737	12.09	10.597	10.132	0.465
Pr0177	J08405669+1944052	130.2362133	+19.7347798	12.23	10.719	10.213	0.506
Pr0179	J08405967+1822044	130.2486506	+18.3678745	11.91	10.261	9.683	0.578
Pr0185	J08411105+2049579	130.2960492	+20.8327459	11.92	10.568	10.120	0.448
Pr0194	J08413384+1958087	130.3909550	+19.9690864	11.71	10.392	9.928	0.464
Pr0201	J08414382+2013368	130.4325668	+20.2268700	10.33	9.463	9.142	0.321
Pr0202	J08414549+1916023	130.4395512	+19.2672912	10.16	9.223	8.933	0.290
Pr0203	J08414776+1924439	130.4490295	+19.4121820	11.42	10.386	10.096	0.290
Pr0206	J08415199+2010013	130.4665939	+20.1669759	12.04	10.554	10.086	0.468
Pr0208	J08415587+1941229	130.4827900	+19.6896756	11.05	9.869	9.544	0.325
Pr0210	J08415924+2055072	130.4968368	+20.9186489	11.27	10.067	9.705	0.362
Pr0211	J08421149+1916373	130.5479103	+19.2770025	12.15	10.660	10.173	0.487
Pr0218	J08422162+2010539	130.5900524	+20.1816448	9.22	8.444	8.280	0.164
Pr0219	J08422269+2007063	130.5945174	+20.1184084	12.10	10.457	9.914	0.543
Pr0222	J08424021+1907590	130.6675468	+19.1330792	12.15	10.685	10.186	0.499
Pr0223	J08424071+1932354	130.6696609	+19.5431875	9.87	8.951	8.721	0.230
Pr0225	J08424250+1905589	130.6770753	+19.0997037	11.62	10.302	9.881	0.421
Pr0226	J08424372+1937234	130.6821545	+19.6231567	12.12	10.371	9.800	0.571
Pr0227	J08424441+1934479	130.6850574	+19.5799575	9.73	8.857	8.633	0.224
Pr0228	J08424525+1851362	130.6885192	+18.8600564	10.90	9.530	9.168	0.362
Pr0232	J08430241+1910031	130.7600692	+19.1675689	12.13	10.615	10.158	0.457
Pr0235	J08431076+1931346	130.7948495	+19.5262870	11.78	10.439	10.007	0.432
Pr0240	J08433463+1837199	130.8942965	+18.6222012	11.75	10.259	9.601	0.658
Pr0246	J08441195+1754079	131.0498500	+17.9021814	10.00	9.049	8.776	0.273
Pr0253	J08450735+2023418	131.2806292	+20.3949689	11.91	10.502	10.050	0.452
Pr0254	J08451468+2059512	131.3111474	+20.9975845	10.40	8.717	8.482	0.235
Pr0255	J08451801+1853254	131.3250368	+18.8903589	9.20	8.801	8.601	0.200
Pr0259	J08452794+2139128	131.3664265	+21.6535859	10.66	9.551	9.257	0.294
Pr0260	J08455330+2102172	131.4720792	+21.0381156	11.96	10.466	9.968	0.498
Pr0264	J08463327+1845394	131.6386477	+18.7609656	9.20	8.444	8.253	0.191
Pr0266	J08464732+1938410	131.6971824	+19.6447245	10.75	9.621	9.342	0.279
Pr0269	J08471411+1623473	131.8088403	+16.3964756	10.70	9.561	9.294	0.267
Pr0270	J08473577+2155364	131.8990642	+21.9268006	12.00	10.773	10.316	0.457
Pr0272	J08482783+1820439	132.1160080	+18.3455317	11.43	10.164	9.772	0.392
Pr0274	J08490670+1941113	132.2779539	+19.6864964	11.93	10.533	10.068	0.465
Pr0276	J08493389+2030290	132.3912518	+20.5080914	9.35	8.527	8.369	0.158
Pr0277	J08495998+1821541	132.4999321	+18.3650131	11.22	10.015	9.640	0.375
Pr0025	J08322347+2059449	128.0978003	+20.9958103	12.82	11.043	10.470	0.573
Pr0029	J08325223+1958359	128.2176612	+19.9766459	13.07	11.145	10.560	0.585
Pr0033	J08331542+2042089	128.3142559	+20.7024920	12.71	11.015	10.436	0.579
Pr0039	J08340436+2034303	128.5181859	+20.5750989	12.80	11.038	10.442	0.596
Pr0057	J08362269+1911293	129.0945580	+19.1914848	12.41	10.763	10.257	0.506

Name	2MASS	RA	DEC	V	J	K	J-K
Pr0060	J08362830+2013429	129.1179380	+20.2285909	12.65	10.982	10.441	0.541
Pr0063	J08364182+2024399	129.1742489	+20.4110895	12.89	11.183	10.523	0.660
Pr0069	J08365411+1845247	129.2254533	+18.7568517	12.73	11.003	10.469	0.534
Pr0073	J08370037+2232470	129.2515771	+22.5464023	12.60	10.983	10.448	0.535
Pr0091	J08374640+1935575	129.4433795	+19.5992931	12.33	10.725	10.244	0.481
Pr0108	J08384610+2034363	129.6921074	+20.5767798	12.44	10.825	10.313	0.512
Pr0109	J08384973+1815571	129.7071992	+18.2658559	12.58	10.920	10.396	0.524
Pr0113	J08390228+1919343	129.7595089	+19.3262445	12.39	10.730	10.259	0.471
Pr0122	J08392185+1951402	129.8410500	+19.8612067	12.53	10.874	10.369	0.505
Pr0134	J08394707+1949395	129.9461124	+19.8276331	12.74	11.006	10.435	0.571
Pr0180	J08410262+2027278	130.2609168	+20.4577012	12.35	10.780	10.291	0.489
Pr0190	J08412258+1856020	130.3440850	+18.9338748	12.96	11.162	10.536	0.626
Pr0230	J08424847+2034244	130.7019586	+20.5734309	12.57	10.793	10.262	0.531
Pr0239	J08433239+1944378	130.8849265	+19.7438162	12.33	10.755	10.218	0.537
Pr0244	J08435467+1853369	130.9778124	+18.8935889	12.67	10.961	10.412	0.549
Pr0248	J08441706+1844119	131.0711186	+18.7366042	12.34	10.766	10.262	0.504
Pr0249	J08442031+1802595	131.0846518	+18.0498617	13.35	11.128	10.490	0.638
Pr0252	J08444870+2017259	131.2029586	+20.2905539	13.02	11.080	10.508	0.572
Pr0261	J08461307+2043432	131.5544512	+20.7286773	13.45	11.116	10.494	0.622
Pr0285	J08391664+1727465	129.8193512	+17.4629209	11.67	10.400	9.965	0.435
Pr0286	J08402624+1913099	130.1093762	+19.2194239	12.88	11.088	10.461	0.627
Pr0287	J08404439+1839235	130.1849848	+18.6565231	12.93	11.126	10.500	0.626

Note — Stars below the line break are the faint targets that we will observe only once in order to vet them for future surveys.

2.3.2 Hyades Stars

The Hyades is similar to Praesepe in size, age (625 Myr; Perryman et al. 1998), and metallicity ([Fe/H] = $+0.13 \pm 0.01$, Paulson et al. 2003; though Liu et al. 2016 find a metallicity higher by $\sim$0.04 dex on average, and with an intrinsic dispersion of 0.021), but it sits more than 4 times closer ($d = 46$ pc; van Leeuwen 2009). The resulting increase in brightness makes the Hyades an excellent target, as high SNR can be achieved in short exposures, and a much wider range of stellar masses will satisfy our magnitude cuts.

The Hyades had been previously observed with high-precision RVs in search of planets (see the series of papers describing the survey: Cochran et al. 2002; Paulson et al. 2004a,b). However, in an effort to observe a wide range of stellar masses, the authors were unable to include all FGK members of the cluster in their survey, so we aim to complement this work by observing any remaining FGK Hyads. To identify suitable targets for our survey,

we began with a list assembled for the Harvard-Smithsonian Center for Astrophysics (CfA) Hyades binary survey (R. Stefanik, private communication). Since 1979, the CfA team has been monitoring over 600 stars in the Hyades field, extending to a magnitude of $V = 15$. Originally the program consisted of stars drawn from the Hyades lists of van Bueren (1952), van Altena (1966), and Pels et al. (1975). Over the years additional stars were added to the observing program if there was some suggestion that the stars were possible members based on photometric, proper motion, or radial velocity investigations of the cluster. Also added to the CfA program were the companion stars of Hyades visual binaries. From this parent list, the sample surveyed here was determined after excluding close ($< 1\farcs0$) visual binaries revealed by high-resolution imaging (Patience et al. 1998), the 94 stars previously surveyed by Paulson et al. (2004b), rapid rotators ($v \sin i_\star > 30\,\mathrm{km\,s^{-1}}$), faint targets ($V > 12$), and spectroscopic binaries (with orbits or long-term trends) from the literature and the CfA survey. The final target list (Table 2.3) contained 27 FGK Hyades members, which are plotted on the CMD in Figure 2.2.

Table 2.3: Hyades Target List

Name	2MASS	RA	DEC	V	J	K	J-K
J202A	J03172284+2618545	049.3449683	+26.3158967	11.11	8.390	7.417	0.973
H24098C	J03501320-0131093	057.5550353	-01.5192859	11.20	11.133	10.524	0.609
L7	J03524101+2548159	058.1708774	+25.8044464	11.15	8.704	7.893	0.811
G7-73C	J04011285+1205479	060.3036053	+12.0966784	11.30	9.710	8.907	0.803
L15	J04070122+1520062	061.7551074	+15.3350309	10.49	8.365	7.665	0.700
L18	J04083620+2346071	062.1508889	+23.7686137	9.44	7.840	7.323	0.517
VB13	J04104233+1825236	062.6765168	+18.4232531	6.62	5.795	5.572	0.223
VB14	J04112030+0531228	062.8345086	+05.5230489	5.73	5.062	4.821	0.241
H111	J04145191+1303178	063.7164003	+13.0549587	10.74	8.445	7.688	0.757
L26	J04172512+1901478	064.3548006	+19.0299095	10.83	8.597	7.909	0.688
H210	J04193684+1237274	064.9036433	+12.6243281	9.81	8.110	7.564	0.546
H246	J04213478+1424352	065.3949792	+14.4097878	6.61	5.784	5.595	0.189
L38	J04240740+2207079	066.0309515	+22.1188689	11.02	8.627	7.886	0.741
H342	J04250024+1659057	066.2510250	+16.9848900	10.28	8.486	7.830	0.656
L58	J04264760+2114059	066.6984100	+21.2349162	11.24	8.724	7.936	0.788
G7-227	J04275674+1903390	066.9865274	+19.0608275	11.29	9.045	8.354	0.691
H422	J04281085+1628155	067.0452912	+16.4709342	11.09	8.560	7.758	0.802
H469	J04293033+1751475	067.3764612	+17.8631628	6.92	6.045	5.809	0.236

Name	2MASS	RA	DEC	V	J	K	J-K
H472	J04293098+1614413	067.3791353	+16.2447825	10.33	8.224	7.515	0.709
VB86	J04305716+1045063	067.7382153	+10.7517703	7.10	6.139	5.893	0.246
G8-64	J04470892+2052564	071.7872259	+20.8823153	9.85	7.966	7.337	0.629
AK2-1315	J04471851+0627113	071.8271189	+06.4532106	11.33	8.651	7.875	0.776
VB116	J04490351+1838285	072.2646912	+18.6412431	9.00	7.486	7.059	0.427
L96	J04500069+1624436	072.5029656	+16.4120628	10.61	8.485	7.839	0.646
+23755	J04530112+2329133	073.2547789	+23.4869928	10.56	8.591	7.959	0.632
L101	J04570066+1354446	074.2528162	+13.9123625	10.94	8.762	8.119	0.643
VB128	J04594432+1555002	074.9346768	+15.9167325	6.80	5.856	5.645	0.211

2.3.3 Coma Berenices Stars

Coma Berenices is another adolescent cluster (∼450-600 Myr Hambly et al. 1995; Collier Cameron et al. 2009), though it is smaller than the Hyades and Praesepe (Kraus & Hillenbrand 2007 identify only 149 candidate members), and its metallicity is lower, possibly even slightly sub-Solar ([Fe/H] = −0.06; Boesgaard et al. 2003). It is located about twice as close as Praesepe (87 pc; van Leeuwen 2009), though, so our target stars are brighter. Coma Berenices therefore represents an opportunity to obtain inexpensive observations of stars in a more sparsely populated cluster at a similar age. Any differences in planetary populations that we observe may be due to the dynamical environment (and metallicity, of course).

Like we did in Praesepe, we selected our Coma Berenices targets from the membership lists of Kraus & Hillenbrand (2007), supplemented by stars that appear to be probable members according to Casewell et al. (2006) and Collier Cameron et al. (2009). We employed similar cuts as in Praesepe and the Hyades, excluding binaries identified by Mermilliod et al. (2009) and stars with $V > 12$ or, when known, $v \sin i_\star > 30\,\mathrm{km\,s^{-1}}$. We adjusted our magnitude cutoff here because Coma Berenices is closer than Praesepe; we actually survey redder stars in Coma Berenices despite our more stringent cutoff, and given that telescope

time is a limited resource, a somewhat brighter, smaller sample keeps total exposure time down. Moreover, we expect that a large number of these redder possible members will turn out to be contaminating background giants, because, as noted by Kraus & Hillenbrand (2007), the proper motion of the cluster is low. Therefore, evolved background stars may lie near the main sequence on a color-magnitude diagram yet still have proper motions consistent with membership. Fortunately, we will not have to expend significant resources on non-members, as the RV that we derive from the first spectrum of each star will provide an easy way to rule out stars with discrepant space motions, and the surface gravity that we derive from an analysis of the spectrum will provide confirmation that the star is evolved. Our target list is given in Table 2.4 and these stars are included in the CMD of Figure 2.2.

Table 2.4: Coma Berenices Target List

Name	2MASS	RA	DEC	V	J	K	J-K
CB0001	J11483770+2816305	177.1570865	+28.2751645	10.47	9.015	8.585	0.430
CB0002	J11553336+2943417	178.8890033	+29.7282631	11.52	9.692	9.057	0.635
CB0003	J12005224+2719237	180.2176736	+27.3232670	11.61	9.674	8.996	0.678
CB0004	J12042326+2449145	181.0969839	+24.8206912	10.19	8.750	8.343	0.407
CB0005	J12061393+2646503	181.5579950	+26.7806659	11.73	10.003	9.394	0.609
CB0006	J12075391+2555455	181.9746359	+25.9292895	11.48	9.332	8.626	0.706
CB0007	J12075772+2535112	181.9904803	+25.5865017	11.17	9.534	8.906	0.628
CB0008	J12091244+2639390	182.3018856	+26.6608092	11.63	9.829	9.184	0.645
CB0009	J12110738+2559249	182.7807600	+25.9901723	9.62	8.387	8.073	0.314
CB0010	J12113516+2922444	182.8965071	+29.3790259	11.35	9.575	8.979	0.596
CB0011	J12122488+2722482	183.1037295	+27.3800981	8.12	7.274	7.082	0.192
CB0012	J12125324+2615014	183.2217895	+26.2504009	11.58	9.577	8.990	0.587
CB0013	J12134391+2253168	183.4329098	+22.8879967	8.13	7.211	6.990	0.221
CB0014	J12140814+2250273	183.5339583	+22.8409370	11.56	9.651	8.992	0.659
CB0015	J12160249+2802553	184.0104203	+28.0486784	8.37	7.414	7.200	0.214
CB0016	J12161909+2655375	184.0795056	+26.9271137	10.32	8.477	7.798	0.679
CB0017	J12172544+2714323	184.3559809	+27.2423331	11.18	9.714	9.142	0.572
CB0018	J12175090+2534167	184.4621124	+25.5713434	7.89	7.086	6.928	0.158
CB0019	J12181778+2338327	184.5741056	+23.6424584	11.53	9.764	9.105	0.659
CB0022	J12190147+2450461	184.7561409	+24.8461681	8.83	7.837	7.537	0.300
CB0023	J12192836+2417033	184.8681574	+24.2842517	9.07	7.867	7.492	0.375
CB0024	J12204557+2545572	185.1898795	+25.7658659	9.10	7.974	7.649	0.325
CB0025	J12211561+2609140	185.3150700	+26.1539081	11.57	9.614	8.972	0.642
CB0026	J12214901+2632568	185.4542798	+26.5490981	9.31	8.214	7.857	0.357
CB0027	J12215616+2718342	185.4840203	+27.3095070	8.53	7.565	7.325	0.240
CB0028	J12222475+2227509	185.6031539	+22.4641420	8.55	7.604	7.387	0.217
CB0029	J12223138+2549424	185.6307992	+25.8285239	8.55	7.406	7.024	0.382
CB0030	J12225224+2504000	185.7176856	+25.0667092	10.61	8.646	7.959	0.687
CB0031	J12225237+2638243	185.7181965	+26.6401064	11.89	9.777	9.115	0.662
CB0032	J12225941+2458584	185.7475683	+24.9829223	11.24	9.396	8.674	0.722

Name	2MASS	RA	DEC	V	J	K	J-K
CB0033	J12231198+2914597	185.7999548	+29.2499642	10.99	9.127	8.474	0.653
CB0034	J12232820+2553400	185.8675359	+25.8944342	11.84	9.920	9.260	0.660
CB0035	J12232870+2250559	185.8695403	+22.8488256	10.60	8.600	8.008	0.592
CB0036	J12234101+2658478	185.9208771	+26.9799312	8.37	7.461	7.253	0.208
CB0037	J12234722+2314444	185.9467359	+23.2457025	11.42	9.677	9.018	0.659
CB0038	J12240572+2607430	186.0238892	+26.1286028	10.19	9.080	8.611	0.469
CB0039	J12241037+2929196	186.0432321	+29.4887809	11.53	10.065	9.327	0.738
CB0040	J12241714+2419281	186.0714392	+24.3245409	10.00	8.417	7.903	0.514
CB0041	J12242581+2136175	186.1075874	+21.6048870	11.24	9.388	8.779	0.609
CB0042	J12245359+2343048	186.2232771	+23.7180639	11.34	9.385	8.824	0.561
CB0043	J12250226+2533383	186.2594048	+25.5606650	8.09	7.051	6.762	0.289
CB0044	J12251014+2739448	186.2922862	+27.6624459	11.56	9.567	8.930	0.637
CB0045	J12252249+2313447	186.3437350	+23.2290895	8.61	7.644	7.392	0.252
CB0046	J12255195+2646359	186.4664700	+26.7766692	8.38	7.411	7.205	0.206
CB0047	J12262401+2515430	186.6001374	+25.2619734	11.98	10.193	9.589	0.604
CB0048	J12265103+2616018	186.7126165	+26.2671789	11.86	9.855	9.156	0.699
CB0049	J12270081+2936380	186.7533812	+29.6105548	11.65	9.803	9.201	0.602
CB0050	J12270627+2650445	186.7760868	+26.8457037	10.03	8.642	8.246	0.396
CB0051	J12272068+2319475	186.8362056	+23.3298517	10.41	8.912	8.451	0.461
CB0052	J12274829+2811397	186.9512292	+28.1944098	9.74	8.436	8.050	0.386
CB0053	J12282110+2802259	187.0879674	+28.0405739	10.52	8.943	8.465	0.478
CB0054	J12283429+2332304	187.1428730	+23.5418164	11.06	9.473	8.861	0.612
CB0055	J12285643+2632573	187.2351112	+26.5492898	10.97	9.208	8.661	0.547
CB0057	J12294216+2837147	187.4256677	+28.6207795	11.40	9.791	9.198	0.593
CB0058	J12310309+2743491	187.7629071	+27.7303395	8.59	7.612	7.404	0.208
CB0059	J12310477+2415454	187.7699045	+24.2626428	10.63	8.809	8.197	0.612
CB0060	J12320807+2854064	188.0336706	+28.9017959	11.43	9.623	8.995	0.628
CB0061	J12323108+3519523	188.1294683	+35.3311973	9.64	8.407	8.086	0.321
CB0062	J12330062+2742447	188.2526109	+27.7124253	11.32	9.470	8.866	0.604
CB0063	J12332002+2224234	188.3333792	+22.4064978	10.41	8.855	8.402	0.453
CB0064	J12333019+2610001	188.3757924	+26.1666892	11.29	9.241	8.591	0.650
CB0065	J12334212+2556340	188.4254962	+25.9427781	10.68	9.031	8.584	0.447
CB0067	J12340646+3201367	188.5269739	+32.0269103	8.33	7.281	7.022	0.259
CB0068	J12341422+2822419	188.5593150	+28.3783139	11.83	10.065	9.395	0.670
CB0070	J12345429+2727202	188.7262256	+27.4556284	9.10	7.897	7.510	0.387
CB0071	J12350033+3011337	188.7513871	+30.1926684	8.65	7.673	7.454	0.219
CB0072	J12351702+2603218	188.8209815	+26.0560684	11.24	9.513	8.925	0.588
CB0073	J12354306+2555227	188.9294474	+25.9230017	11.91	10.127	9.492	0.635
CB0074	J12360464+2757356	189.0193503	+27.9599239	11.96	9.903	9.297	0.606
CB0075	J12374817+2657472	189.4507795	+26.9631184	10.82	8.846	8.163	0.683
CB0076	J12381493+2621280	189.5622598	+26.3578098	10.25	8.564	7.998	0.566
CB0077	J12394200+2134578	189.9250139	+21.5827725	11.99	9.488	8.799	0.689
CB0078	J12395243+2546331	189.9684580	+25.7758362	11.25	9.232	8.651	0.581
CB0079	J12421455+2836128	190.5606283	+28.6035209	10.07	8.258	7.634	0.624
CB0080	J12423510+4105276	190.6463239	+41.0910153	11.79	9.956	9.273	0.683
CB0081	J12432507+2647077	190.8544686	+26.7855012	11.71	9.831	9.174	0.657
CB0082	J12490041+2521356	192.2517495	+25.3598823	11.77	9.750	9.069	0.681
CB0083	J12493043+2532109	192.3768071	+25.5364234	11.56	9.613	8.931	0.682
CB0084	J12500170+2103121	192.5071153	+21.0534025	11.28	9.558	8.976	0.582
CB0085	J12521160+2522245	193.0484042	+25.3734937	8.89	7.881	7.609	0.272
CB0086	J12573686+2858448	194.4035971	+28.9791078	10.41	8.897	8.473	0.424
CB0087	J13054399+2003214	196.4333265	+20.0559525	11.18	9.527	8.922	0.605

2.3.4 Ursa Major Stars

The Ursa Major Moving Group is a nearby population of stars consisting of a small nucleus of about 15 stars (located at about 25 parsecs) and a larger number of likely members in a stream, which extends a great distance from the nucleus—the Sun's position, for example, is located inside of this stream. The Sun is not a member, though, as the estimated age of the group is only about 500 Myr (Jones et al. 2015; King et al. 2003). Identifying members using kinematic and spectroscopic criteria, Ammler-von Eiff & Guenther (2009) estimate the metallicity to be about [Fe/H] = −0.03. We select our targets from this same list of likely members, excluding components of close visual pairs. In total, we include 20 stars.

Table 2.5: Ursa Major Target List

Name	2MASS	RA	DEC	V	J	K	J-K
HD11131	J01492335-1042125	027.3473156	-10.7035723	8.78	5.536	5.149	0.387
HD24916A	J03572871-0109338	059.3695895	-01.1594600	8.20	6.063	5.341	0.722
HD26923	J04152879+0611128	063.8700024	+06.1868581	8.52	5.201	4.903	0.298
HD28495	J04335424+6437593	068.4761130	+64.6331895	8.67	6.239	5.750	0.489
HD38393	J05442780-2226538	086.1157956	-22.4483834	3.65	2.804	2.508	0.296
HD41593	J06064047+1532317	091.6686595	+15.5421062	8.62	5.317	4.822	0.495
HD59747	J07330059+3701475	113.2524136	+37.0298417	9.01	6.090	5.589	0.501
HD95650	J11023832+2158017	165.6597642	+21.9671364	9.59	6.522	5.688	0.834
HD238087	J12120522+5855351	183.0217350	+58.9264292	10.02	7.569	6.832	0.737
HD109011	J12311893+5507078	187.8288448	+55.1188437	8.70	6.324	5.662	0.662
HD109647	J12355128+5113172	188.9636827	+51.2214737	8.64	6.728	6.157	0.571
HD110463	J12414450+5543288	190.4355083	+55.7246723	8.38	6.569	6.003	0.566
HD115043	J13133699+5642298	198.4042024	+56.7082703	6.88	5.675	5.334	0.341
HD238224	J13232325+5754222	200.8470398	+57.9061187	9.56	7.172	6.421	0.751
HD152863A	J16550215+2543504	253.7590065	+25.7306839	6.17	4.351	3.868	0.483
HD155674A	J17101050+5429397	257.5437850	+54.4943784	9.22	6.788	6.118	0.670
HD155674B	J17101235+5429245	257.5514809	+54.4901425	9.54	7.017	6.283	0.734
HD167389	J18130721+4128315	273.2801062	+41.4753642	7.45	6.224	5.918	0.306
HD184960	J19341977+5114121	293.5824586	+51.2366198	5.78	4.700	4.494	0.206
HD205435	J21335883+4535307	323.4952209	+45.5918370	4.09	2.485	1.901	0.584

2.4 Potential biases

Looking ahead to the interpretation of results that we hope to obtain from our survey, we note here several potential biases that may arise from our sample selection, most of which can be addressed by examining subsamples, with completeness corrections, or with complementary work.

First, we note that requiring slow projected rotational velocities may introduce an inclination bias in stars that are inherently rapidly rotating. While we expect the G and K stars at ∼600 Myr to be rotating intrinsincally slowly enough to satisfy our $v \sin i_\star$ cuts (see, e.g., Mamajek & Hillenbrand 2008), some F stars (early-to-mid F, in particular) are expected to have rotational velocities greater than $30\,\mathrm{km\,s^{-1}}$. Therefore, only the face-on rotators among these stars will be included in our sample. This would lead to reduced sensitivity to planets if their orbits are well-aligned with the stellar spin (and conversely, would lead to an increased likelihood to detect any misaligned planets around the earlier-type stars). The most massive of such planets, for which we expect the orbital amplitude of an edge-on orbit to be much greater than our measurement errors, would likely still be detected, though it is unavoidable that the minimum detectable mass would be larger for highly inclined orbits. However, we expect any such bias to be minimal because the RV technique is quite sensitive even to highly inclined orbits.

A second potential bias that has been introduced is that we have removed binaries from our sample. While this gives us a sample that is easier to observe and analyze, if we want to interpret hot Jupiter occurrence rates for clusters in comparison to the rate for field stars, we

must be cognizant of the potential differences in binarity between parent samples. While field star planet surveys also typically avoid close binaries (if they are detected), a given angular separation for a distant cluster star corresponds to a much larger physical separation than it does for a nearby field star. Thus, our visual binary cuts may exclude more distant binaries from our survey than a typical field star survey would. This may be important because while close binaries may suppress planet formation (see, e.g., Kraus et al. 2016), more distant binaries may enhance hot Jupiter production through Kozai-Lidov migration. If Kozai-Lidov migration is very important for hot Jupiter migration (a hypothesis that will be tested by some of the research within this dissertation), then the observed hot Jupiter frequency in our sample may not reflect the overall frequency of giant planets in clusters.

Finally, we have instituted a magnitude-limited survey, which comes with well-known biases. Most importantly, stars in more distant clusters like Praesepe will be, on average, of earlier type than stars in more nearby clusters like the Hyades. This can be seen in Figure 2.2, which shows that our Hyades targets extend to $J - K \sim 0.8$ (early M dwarfs) while we only target Praesepe stars as red as $J - K \sim 0.5$ (early K dwarfs). Therefore, when comparing planet occurrence rates between clusters or with the field, we will have to be sure to account for the differing stellar populations that have been surveyed.

CHAPTER 3
SURVEY STRATEGY & OBSERVATIONS

With target lists in hand, we must identify successful, yet efficient, strategies for observing these stars. Such a strategy must include a balance between sensitivity to planets (which is determined by the achieved RV precision, the number of observations, and the observing cadence) and the telescope time required (which dictates the number of targets that can be observed given a fixed telescope time allocation). To balance these quantities there are many levers to pull, not the least of which is the choice of instrument and telescope. For example, while an instrument capable of $1\,\mathrm{m\,s^{-1}}$ precision mounted on a large aperture ($10\,m$–class) telescope might be the first choice for a high-precision RV survey, practical considerations muddy the waters: such telescopes are always over-subscribed, and as a result, one should expect the total observing time awarded—if any—to be small. In contrast, time allocation committees for some medium aperture (1–$3\,m$) telescopes are much more likely to grant a large time request, as they tend to have lower overall subscription rates. Furthermore, the requirements of our particular survey—a giant planet search in nearby $\sim$600 Myr clusters—lessen the need for a super-precise instrument on a large aperture telescope. The previously mentioned Hyades planet survey (Paulson et al. 2004b) determined the typical RV jitter due to activity of 600 Myr Sun-like stars to be about $16\,\mathrm{m\,s^{-1}}$. As such, the utility of an instrument with $1\,\mathrm{m\,s^{-1}}$ RV precision is dramatically lessened for our survey; an instrument with intrinsic precision of $\sim$$10\,\mathrm{m\,s^{-1}}$ would deliver performance nearly on par with a more precise instrument because the final observed RV scatter will be due to the combination (in

quadrature) of astrophysical jitter and instrumental uncertainty, in which the astrophysical jitter is the dominant term. While these moderately high-precision instruments tend to be mounted on medium-aperture telescopes, recall that we have chosen targets to be bright ($V < 12$), so the high signal-to-noise ratio (SNR) observations that are required to approach the instrumental noise floor can still be achieved for all of our stars in reasonable exposure times.

Another consideration related to the instrument is the scheduling of observations. Telescope schedules generally come in two flavors: classical and queue. A classical schedule awards blocks of time (generally consecutive nights or half-nights) to observers based on the ideal time of year for their observations. However, given that our targets are located in small, discrete regions of the sky, it is unlikely that we would be able to observe all of our targets adequately in a single block of contiguous nights (or even several smaller blocks, if the schedule were flexible enough to allow such time allocation). Moreover, because we are interested in detecting planets with periods of a few days to a few weeks, we expect that an observing cadence that samples those timescales well would be more effective than a cadence limited to a few consecutive nights (more on this in the following section). The above requirements are much more well-suited to a queue-scheduled instrument, in which all targets from all observing programs are placed in a single queue, and each is observed when most appropriate (balanced against the needs of other programs). This would allow a customized observing cadence designed to sample the relevant orbital timescales, as well as the flexibility to observe targets throughout the year—when they are placed at an optimal

position in the sky (e.g., near the meridian).

3.1 Observing Cadence

To select an appropriate observing cadence, we first consider the goals of our survey. Our primary goal is to investigate the mechanisms driving hot Jupiter migration, so we should aim to optimize sensitivity to hot Jupiters. This means that we should use our resources to sample short orbital periods ($P < 10$ days). As a secondary goal, sampling on longer timescales (months and years) can provide a clearer picture of the overall giant planet population in clusters, which will allow us to place cluster planets in context with the field.

Previous investigations of the effects of the choice of RV cadence show mixed results. In the context of a large number (dozens) of astrometric observations from space (which, similarly to RVs, must sample an orbit well to ensure detection), Ford (2004) finds that the specific choice of cadence is not particularly important. However, for more modest observing time, an intelligent choice of observing cadence can improve the efficiency of detections, the minimum mass of detected planets, and the uncertainties on the orbital parameters of the discoveries (see, e.g., the adaptive scheduling algorithm described in Ford 2008). We adopt a dual-cadence strategy meant initially to sample short-periods orbits ($P < 10$ days) in search of hot Jupiters, and subsequently to sample longer timescales in search of warm and cold Jupiters or distant binary companions.

More specifically, we plan to observe each star with an initial sequence of three consecutive nights, and then two or three consecutive nights at least one week later. This should provide

sensitivity to orbits with timescales of a few days as well as those with timescales of a few weeks. A significant advantage to this strategy compared to a more random sampling is that short period variables can be identified almost immediately (perhaps after only two or three spectra) and resources can then be allocated preferentially to high priority, planet-hosting stars, rather than equally among all targets. That is, if at any point we identify a star with significant RV variation, we will abandon the initial observing plan and dedicate more intense monitoring to that system. In addition to this short-cadence observing strategy, we will return the next year to observe each star one or two more times in search of variation on longer timescales. We plan similar sparse observations in subsequent seasons to improve sensitivity to these longer-period companions.

To assess the efficacy of such a strategy, we simulate the observation of planetary systems using our proposed cadence to estimate detection limits as a function of planet mass and orbital period. Figure 3.1 shows that among planets with masses $M_{\rm P} > 0.1\,M_{\rm Jup}$ and orbital periods $P < 10\,$days, our cadence is fairly complete.

3.2 Observations

3.2.1 The Instrument

Balancing the factors outlined above—telescope aperture, instrument precision, oversubscription rates, telescope schedule type—we identify the Tillinghast Reflector Echelle Spectrograph (TRES; Fűrész 2008), mounted on the 1.5 m Tillinghast Reflector at Fred L. Whipple Observatory (FLWO) on Mt. Hopkins, AZ as a good match for the needs of our survey.

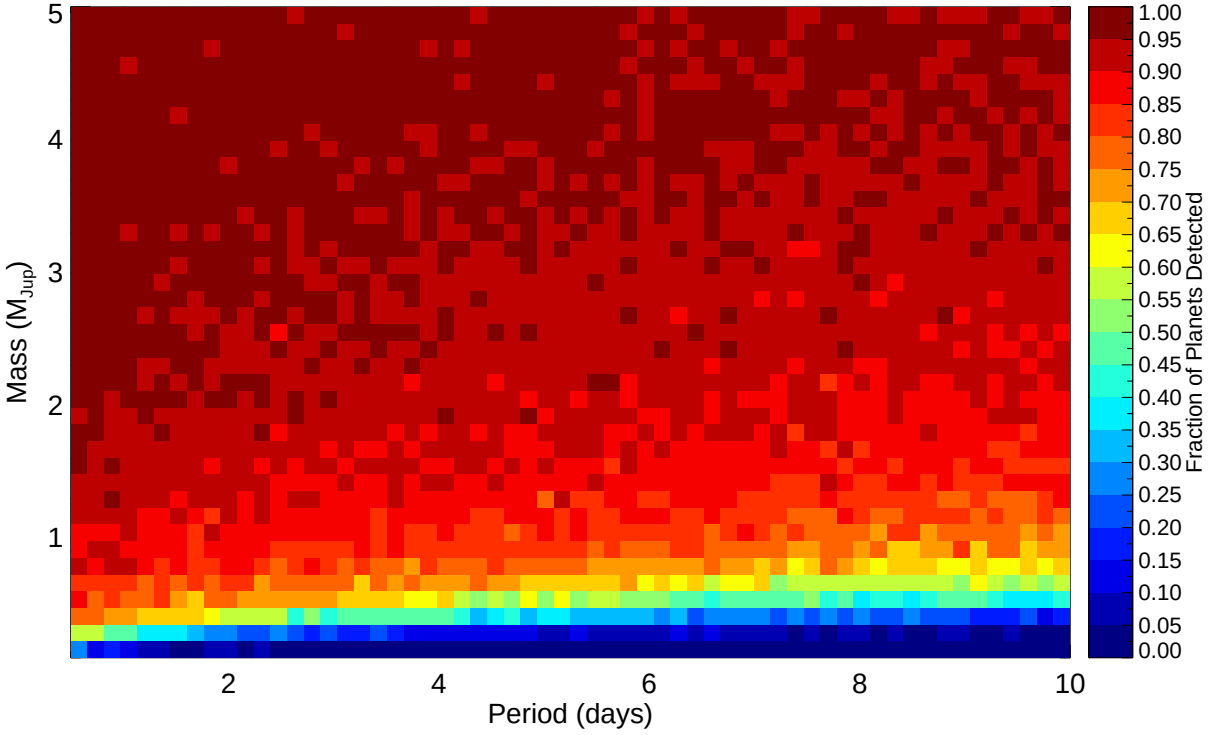

Figure 3.1 A heat map of detection efficiency for our proposed observing cadence (8 total spectra spread over 3 observing seasons), assuming RV uncertainties of $20\,\mathrm{m\,s^{-1}}$. Red regions indicate good sensitivity to planets, while blue regions indicate poor sensitivity. As expected, low-mass, long-period planets are harder to detect, but even with only 8 spectra, we predict that we will be sensitive to most planets with masses $M_\mathrm{P} > 0.5\,M_\mathrm{Jup}$ and periods $P < 10\,\mathrm{days}$, and some planets as small as $\sim 0.3\,M_\mathrm{Jup}$.

TRES is a temperature-controlled, fiber-fed, cross-dispersed echelle spectrograph with a resolving power of $R \sim 44,000$ and a wavelength coverage of 3850–9100 Å that spans 51 echelle orders. While the 1.5 m aperture is quite modest compared to the telescopes on which many extreme-precision RV instruments are mounted, the facility has proven to be quite efficient thanks to several factors: hardware upgrades to improve the stability of the velocity system; established procedures that enable nearly immediate data reduction, PI review of

the data, and daily updates to observing plans; large blocks of queue observing time; and optimization of the camera performance that yields a readout noise of about $2.7\,e^-$. The large spectral grasp of TRES covers information-rich content (for Sun-like stars) in the blue and green—for example, near the Mg I b triplet at 5190 Å—as well as several diagnostic lines for stellar activity, such as the Ca II H&K lines, the Na I D doublet, and Hα and the Balmer series. Along with the development of software tools for stellar classification (Stellar Parameter Classification, or SPC; Buchhave et al. 2012) and data reduction (see the RV pipeline initially described in Buchhave et al. 2010), the camera noise properties and this wealth of spectral information allow TRES spectra to provide precise results, even at relatively low signal-to-noise—as low as 20 per resolution element. These classifications have been used to characterize hundreds of planet-hosting stars (e.g., Buchhave et al. 2014), and the precise RVs (with measurement uncertainties as low as $10\,m\,s^{-1}$, as in Quinn et al. 2014), have allowed the detection or characterization of numerous planetary companions (e.g., Mandushev et al. 2011; Siverd et al. 2012; Bryan et al. 2012; Quinn et al. 2012, 2014, 2015; Bieryla et al. 2015). This RV precision is an excellent match for our survey requirements; we re-emphasize that our target stars are expected to have intrinsic jitter ($\sim$$16\,m\,s^{-1}$) that slightly exceeds the TRES noise floor. In addition to its ideal RV precision, TRES is a queue-scheduled instrument, and therefore provides the desired scheduling flexibility for our survey, as described in Section 3.1. Finally, we note that FLWO is run by the Smithsonian Astrophysical Observatory (SAO), so observing proposals are limited to scientists affiliated with the Harvard-Smithsonian Center for Astrophysics (which includes SAO and the Har-

vard College Observatory); this has kept over-subscription rates relatively low, although this has begun to change in recent proposal periods as the performance of TRES becomes more widely appreciated. We apply for time through our close collaboration with several astronomers at the Harvard-Smithsonian Center for Astrophysics.

3.2.2 Data Acquisition

Following the discussion in Section 3.1, we aim to observe each star in our target list on three consecutive nights, followed by another two or three consecutive nights after a break of at least a week. This short-cadence sequence will provide the sensitivity to short period planets required for a hot Jupiter survey. We then return to those stars in subsequent seasons for sparse observations in search of more distant companions. Deviations from this observing plan may occur for a variety of reasons. Sometimes, the weather or the proximity of the full moon may prevent us from following our desired cadence. Luckily, small deviations from the plan are unlikely to greatly affect the overall sensitivity to planets: our simulations show that completeness should be relatively insensitive to whether observations are made on consecutive nights or if the length of the break between sets of observations varies slightly. We may also deviate from our planned cadence intentially because we no longer think the star is a good target for the survey. If our stellar classifications show the star to be evolved ($\log g < 3.5$), or to have a wildly discrepant composition compared to the cluster mean ($\Delta[\mathrm{m/H}] > 0.25\,\mathrm{dex}$), we stop observing under the assumption that the star is not a member of the cluster. If we detect a constant radial velocity discrepant from the cluster mean by more than $5\,\mathrm{km\,s^{-1}}$, we also stop observing on the basis of non-membership. If we detect

large ($> 1\,\mathrm{km\,s^{-1}}$) RV variations on short timescales, we stop observing under the assumption that close binaries are unlikely to host short-period planets (they may still host circumbinary planets—see, e.g., Doyle et al. 2011; Welsh et al. 2012; Orosz et al. 2012). We *do* continue to monitor stars that show little or no RV variation ($< 1\,\mathrm{km\,s^{-1}}$). These stars may host planets or, if the period is long enough, distant brown dwarfs or stars that are widely separated enough to allow the survival of interior planets; a very distant massive companion may even be a catalyst for inward planetary migration. Finally, we will also deviate from our planned cadence if we detect small but significant RV variation on short timescales. In these cases, we will devote more significant resources to identifying the cause of the variation.

We aim to achieve a SNR per resolution element of about 40 (but at least 20 for faint stars), requiring exposure times ranging from ∼1–25 minutes. We also obtained nightly observations of five IAU RV standard stars (HD 3765, HD 4628, HD 38230, HD 65583, and HD 182488), in order to track the instrument stability and correct for any RV zero point drift that might occur throughout the course of our survey. Precise wavelength calibration is established by obtaining ThAr emission-line spectra before and after each spectrum, through the same fiber as the science exposures.

3.2.3 Spectroscopic Reduction and Cross-Correlation

To analyze the data, we use the data reduction pipeline and RV analysis software developed by Lars Buchhave, which is described in Buchhave et al. (2010). We provide an overview here. Spectra were optimally extracted, rectified to intensity versus wavelength, and for each star the individual spectra were cross-correlated, order by order, using the strongest

exposure of that star as a template. We typically used ∼25 orders (∼4200–6500 Å), rejecting those plagued by telluric absorption, fringing far to the red, and low SNR far to the blue. For each epoch, the cross-correlation functions (CCFs) from all orders were added and fit with a Gaussian to determine the relative RV for that epoch. Using the summed CCF rather than the mean of RVs from each order places more weight on orders with high correlation coefficients. Internal error estimates (which include, but may not be limited to, photon noise) for each observation were calculated as $\sigma_{\rm int} = {\rm RMS}(\vec{v})/\sqrt{N}$, where $\vec{v}$ is a vector containing the RV of each order, N is the number of orders, and RMS denotes the root-mean-squared velocity difference from the mean.

To evaluate the significance of any potential velocity variation, we compared the observed velocity dispersions ($\sigma_{\rm obs}$) to the expected RV measurement uncertainties ($\sigma_{\rm RV}$), which we assume stem from three sources: (1) internal error, $\sigma_{\rm int}$ (described above), (2) night-to-night instrumental error, $\sigma_{\rm TRES}$, and (3) RV jitter induced by stellar activity, $\sigma_\star$. The total expected RV uncertainty is therefore given by $\sigma_{\rm RV} = \sqrt{\sigma_{\rm int}^2 + \sigma_{\rm TRES}^2 + \sigma_\star^2}$, and if all errors are properly estimated and a star has no orbiting companions, the most likely observed dispersion should equal the expected uncertainty ($\sigma_{\rm obs} = \sigma_{\rm RV}$). We know $\sigma_{\rm int}$, and we must therefore try to determine the remaining components of $\sigma_{\rm RV}$ ($\sigma_{\rm TRES}$ and $\sigma_\star$) in order to assess the significance of the observed dispersion.

Before assessing the instrumental error, we used observations of the standard stars to correct for any systematic velocity shifts between runs, calculated in the following way. We construct a fit to the standard star RVs using the Markov Chain Monte Carlo (MCMC)

technique, in which we fit for an RV offset of each standard star and the RV offset of each observing run. Since these are relative RVs, the value of the RV offset for each star doesn't matter; it just matters that we anchor them all to the same scale. We do this first and show the results in the left panel of Figure 3.2, in which all variation can be attributed to instrumental zero-point offsets. We adjust for these offsets using the MCMC results, and show the final, corrected standard star RVs in the right panel of Figure 3.2. The one remaining feature—a single group of high velocities—corresponds to a one-night jump in zero point caused by a known hardware issue. Since the standard stars are assumed to have negligible stellar jitter, we can calculate the uncertainty contributed by instrumental jitter by simply looking at the standard deviations of the corrected RVs in each run. We find that instrument stability changed slightly over the course of our survey, beginning with a stability of $\sim$12-15 $\mathrm{m\,s^{-1}}$, improving to $\sim$6-9 $\mathrm{m\,s^{-1}}$ (sometimes better than 5 $\mathrm{m\,s^{-1}}$) in the period covering summer 2012 through fall 2014, and returning to $\sim$11-14 $\mathrm{m\,s^{-1}}$ since. The improvement can be attributed to the installation of a new camera shutter (the old one generated significant heat throughout the night because it drew power to remain open during exposures; the new shutter is only powered to open or close, and is then latched in place), but we are unable to explain with certainty the cause of the later degradation of performance. Several potential factors include: changes to the telescope optics, as the system was collimated around this time during the telescope shutdown for monsoon season in Arizona; temperature fluctuations, due to the performance of the air conditioner (a new one was installed) or the liquid nitrogen auto-fill; or the mechanical repeatability of the positioning of the periscope arm

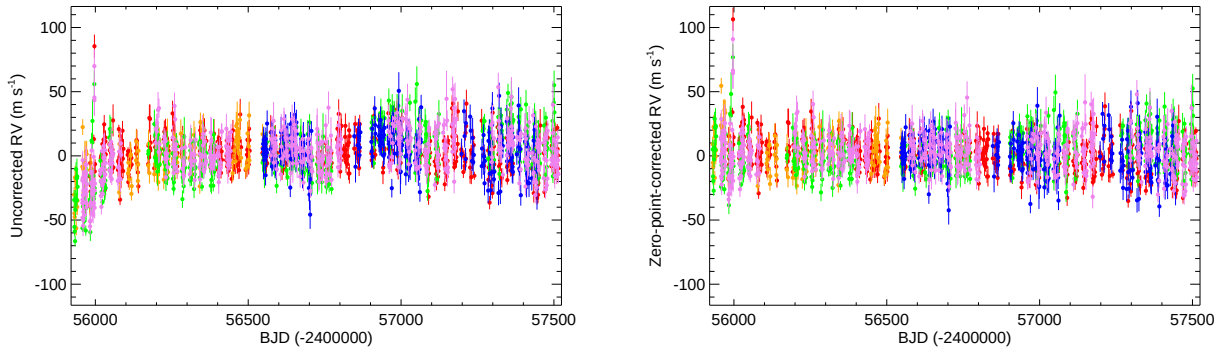

Figure 3.2 *Left*: Relative radial velocities of RV standards HD 182488 (red), HD 3765 (orange), HD 38230 (green), HD 4628 (blue), and HD 65583 (violet) over the course of our survey. *Right*: The same RVs after correcting for the zero point offsets in each observing run. These derived offsets will also be applied to the survey data. Remaining scatter in the standard star RVs is attributed to instrumental jitter, which will be added to the uncertainties of survey RVs.

used for the ThAr lamp exposures. With a nearly two-fold performance improvement at stake, we suggest that all of the above should be examined carefully. Regardless, we add the instrumental jitter from the appropriate run to each observation in our RV survey to account for this noise source. Finally, we note that in general one must also inflate RV errors to account for the uncertainty in the run-to-run offsets that are applied. However, because we have such a rich data set of standard star RVs, the uncertainty in each offset (with the exception of the single-night shift) is smaller than $\sim$1 m s^{-1}, so these errors are negligible given our precisions of 15-20 m s^{-1}.

In order to reduce identification of false signals caused by noisy stars, we set $\sigma_\star = 16\,\mathrm{m\,s^{-1}}$ (the average velocity RMS for all Hyads surveyed by Paulson et al. 2004b) in our initial search for RV variation. We note, however, that the actual stellar jitter for a typical star in each cluster can be estimated from the final observed dispersions and the internal and

instrumental errors. While not a primary goal of our survey, this highlights an ancillary benefit of a planet search around young stars: not all of the stars will host planets, but even null results leave us with a rich data set with which to explore the evolution of stellar astrophysics—in this case the activity of young stars. We explore this jitter calculation in § 3.2.9.

Accounting for the uncertainties described above—internal errors, instrumental jitter, and stellar noise—we constructed a χ^2 fit of each stars RVs assuming a constant velocity, and then calculated $P(\chi^2)$, the probability that a χ^2 value as high as the value observed would arise from a star of constant RV. As described in Latham et al. (2002), $P(\chi^2)$ is a simple and effective metric for identifying variable stars in a radial-velocity survey, and they suggest that nearly all stars below the threshold of $P(\chi^2) = 0.001$ host a companion. While some long-period, low-amplitude variables may lie above this threshold, those stars will often be recognizable by eye. We therefore adopt a threshold for further follow-up of $P(\chi^2) < 0.001$ (i.e., 99.9% confidence of variability). While it is possible that some bona fide planets will not meet this threshold (and will thus be missed by our survey despite having orbital amplitudes large enough for detection), it gives us confidence that our limited telescope resources will be focused on the best planet candidates, and provides a quantitative criterion that can be used to assess completeness and correct for such missed planets.

As we describe below, a number of stars met our variability criterion, and we followed them with additional spectroscopic observations over the course of our survey. We characterize the population of RV variables in more detail in Chapters 4 and 6. Below, we give

details about the observations made in each cluster and we provide an overview of the results for each star in Table 3.1.

3.2.4 Spectroscopic Stellar Classification

To characterize the stars in our survey, we employ the spectral classification routines known as Stellar Parameter Classification (SPC; for a complete description of the routines, see Buchhave et al. 2012, though we briefly describe the code here). SPC compares a library of synthetic spectra to an observed spectrum via cross-correlation in order to assess the goodness of fit for a large number of combinations of stellar atmospheric parameters ($T_{\rm eff}$, $\log g$, [m/H], $v \sin i_\star$). SPC finds the overall best combination of atmospheric parameters via a multi-dimensional surface fit to the correlation coefficients generated from the individual synthetic templates. We use the spectral library maintained at the Harvard-Smithsonian Center for Astrophysics, which was generated from model atmospheres by R. L. Kurucz (see Nordstroem et al. 1994; Latham et al. 2002). The templates were calculated by John Laird, based on a line list compiled by Jon Morse. The spectra cover a wavelength range of $\sim$300 Å centered near 5190 Å, which includes the gravity-sensitive Mg I b triplet, and the templates overlap with three TRES echelle orders. Here we point out that the CfA library uses [m/H] (the scaled-Solar, bulk metallicity abundance relative to the Sun) rather than the iron abundanace [Fe/H]. When comparing these results to measurements of [Fe/H] in the literature, we are therefore implicitly assuming that all metals are enhanced equally, and some small bias in metallicity may be introduced if, for example, a star is enhanced in alpha elements relative to iron. Throughout this work, we treat [m/H] and [Fe/H] interchangeably

(keeping the distinction in mind); when only SPC results are being discussed we use [m/H], and when a combination of literature values and SPC are being discussed we use [Fe/H]. We note that the performance of SPC has been validated against other classification routines such as Spectroscopy Made Easy (SME; Valenti & Piskunov 1996), as well as for systems in which prior constraints on stellar parameters exist—for example, from transiting planets (Torres et al. 2012) or asteroseismology (Buchhave & Latham 2015)—and it has been shown to produce consistent results, even for spectra with signal-to-noise ratios much lower than is typically obtained for precise stellar classification. Given that our data sometimes have relatively low SNRs, SPC is a natural choice for stellar characterization.

One major caveat that must be noted for any spectroscopic stellar classification is that the resulting atmospheric parameters ($T_{\rm eff}$, $\log g$, and [m/H]) are covariant. In general, an unconstrained spectroscopic classification will have difficulty accurately fitting all three quantities because nearly equally good fits can be obtained near the true solution by adjusting all three quantities simultaneously. The result may be biased systematically in one or more of the parameters, and at the very least usually becomes more uncertain than formal errors would indicate. However, if prior knowledge of one or more of the parameters can be used to constrain the fits, these degeneracies can be broken and precise classifications can be obtained. For cluster stars, we have two advantages. We know that all members of the cluster should have roughly the same composition ([Fe/H]), and we have some sense of the age of the stars. In conjunction with stellar models, the age can provide a relationship between $T_{\rm eff}$ and $\log g$, which provides an additional constraint. That being said, with the exception

of the detailed analysis of planet host stars, we do not feel the need to employ such priors; for the purposes of cluster membership, non-members are apparent due to their discrepant RVs, their distance from the $T_{\rm eff}$-$\log g$ main sequence, or their dissimilar compositions. The relatively small possible biases caused by the aforementioned degeneracy will not obscure this information. Because we are using a preliminary SPC analysis for which correlated errors almost certainly exist, we choose not to report errors for individual measurements. Instead, we suggest that typical formal uncertainties of $\sim$150 K in $T_{\rm eff}$, 0.15 dex in $\log g$ and [Fe/H], and $\sim$2 km s^{-1} in $v \sin i_\star$ would be appropriate, and correlated errors may exist with similar magnitudes in the former three parameters ($v \sin i_\star$ is mostly orthogonal to the other three). These typical errors are estimated via the comparisons described above, against other classification routines and systems for which we know (some of) the true quantities (e.g., the Sun, transiting planetary systems, asteroseismic solutions). A more complete description of the uncertainties is presented in Buchhave et al. (2012). The SPC parameters for our stars are included in Table 3.1.

Finally, we find that the coolest stars in our sample—those for which $T_{\rm eff} \lesssim 4750$ K—are affected by a known systematic bias that causes the classification to yield values too low in $T_{\rm eff}$, $\log g$, and [m/H]. This is most likely caused by a limitation of the Kurucz models at cool temperatures, and rather than try to tackle problems of stellar atmosphere modeling, we leave the results as they are but warn the reader that they should only be used with caution, understanding that there are certainly systematic biases for these stars. These results are marked with a warning in Table 3.1.

We also use the cross-correlations from SPC to derive absolute radial velocities for each star in our survey. (These absolute RVs can aid in confirming cluster membership, and have the potential to be used for dynamical studies of the clusters themselves.) Because each synthetic template spectrum has a known absolute RV (with precision set by the fidelity of the line lists used to generate the synthetic spectrum) of $0\,\mathrm{km\,s^{-1}}$ (i.e., spectral lines are at rest wavelengths), the wavelength shift that is required to match the observed spectrum yields the observed star's absolute RV. However, we must also account for the absolute TRES instrumental zero point, and we do this by comparing the absolute RVs of our standard stars to their values on the IAU standard scale, which we take from Nidever et al. (2002). We derive a TRES instrumental zero point offset of $650 \pm 100\,\mathrm{m\,s^{-1}}$, which must be subtracted from our SPC-derived absolute RVs to shift them to the IAU scale. In general, the uncertainty in the instrumental zero point will dominate, since the observed RV scatter is on the order of tens of meters per second for the stars in our sample. The shifted absolute RVs are reported in Table 3.1. Finally, we note that a small, surface gravity-dependent bias will exist in these absolute RVs because the wavelength scales of our template spectra do not account for the gravitational redshift of the star.

Table 3.1: Summary of Spectroscopic Observations

Cluster	Name	$N_{\rm obs}$	ΔT[a] (days)	$T_{\rm eff}$[b] (K)	$\log g$ (dex)	[m/H] (dex)	$v \sin i_\star$ ($\mathrm{km\,s^{-1}}$)	$v_{\rm abs}$[c] ($\mathrm{km\,s^{-1}}$)	$\sigma_{\rm obs}$[d] ($\mathrm{m\,s^{-1}}$)	$\sigma_{\rm RV}$[e] ($\mathrm{m\,s^{-1}}$)	$P(\chi^2)$	Comments[f]
Praesepe	Pr0009	1	···	5849	4.24	−0.50	3.1	36.366	117.0	···	···	NM
Praesepe	Pr0014	4	38.8	6251	4.01	−0.08	10.9	31.230	26.9	43.9	0.829165	NM
Praesepe	Pr0017	7	1501.9	6036	4.58	0.14	6.5	35.899	25.5	22.9	0.558544	
Praesepe	Pr0021	1	···	6023	4.45	−0.15	3.0	33.260	100.0	···	···	NM?
Praesepe	Pr0024	2	1082.9	6150	3.70	−0.48	6.8	19.384	43.9	61.8	0.491270	NM
Praesepe	Pr0035	25	1474.9	6205	4.04	−0.06	14.5	34.709	636.5	41.4	0.000000	V
Praesepe	Pr0036	1	···	5901	4.42	0.11	17.8	2.046	100.0	···	···	NM
Praesepe	Pr0044	9	1569.8	5820	4.57	0.10	4.9	35.168	40.0	19.6	0.008375	
Praesepe	Pr0047	7	1497.0	5578	4.69	0.19	3.1	35.638	41.3	24.2	0.123371	
Praesepe	Pr0051	7	1520.0	6054	4.52	0.14	4.7	35.068	20.9	24.4	0.792934	
Praesepe	Pr0058	16	1368.2	6001	4.51	0.11	8.8	35.496	1693.8	28.5	0.000000	SB

Cluster	Name	$N_{\rm obs}$	ΔT[a] (days)	$T_{\rm eff}$[b] (K)	$\log g$ (dex)	[m/H] (dex)	$v \sin i_\star$ ($\rm km\,s^{-1}$)	$v_{\rm abs}$[c] ($\rm km\,s^{-1}$)	$\sigma_{\rm obs}$[d] ($\rm m\,s^{-1}$)	$\sigma_{\rm RV}$[e] ($\rm m\,s^{-1}$)	$P(\chi^2)$	Comments[f]
Praesepe	Pr0062	7	1517.8	5563	4.72	0.16	2.8	34.507	17.2	23.7	0.899157	
Praesepe	Pr0065	7	1542.8	5609	4.62	0.14	3.6	34.424	23.3	18.0	0.393396	
Praesepe	Pr0076	35	1538.8	5769	4.61	0.15	4.4	35.130	30.7	19.7	0.012962	
Praesepe	Pr0079	8	1542.0	5702	4.64	0.18	3.9	34.717	30.0	17.0	0.122474	
Praesepe	Pr0081	7	1542.7	5755	4.63	0.13	5.6	35.532	30.8	25.4	0.475128	
Praesepe	Pr0084	7	1542.8	5609	4.67	0.17	5.1	35.393	29.2	16.1	0.091767	
Praesepe	Pr0085	7	1502.9	6248	4.53	0.17	10.4	34.945	77.3	35.4	0.046338	V
Praesepe	Pr0086	1	···	6851	4.43	0.10	81.9	38.511	269.0	···	···	FR
Praesepe	Pr0092	7	1511.8	6115	4.54	0.14	9.6	34.851	49.2	37.5	0.226353	
Praesepe	Pr0093	7	1518.8	5279	4.70	0.23	3.9	35.621	19.8	25.0	0.838446	
Praesepe	Pr0095	7	1566.8	5825	4.64	0.12	5.1	34.517	44.5	27.1	0.027628	
Praesepe	Pr0096	7	1517.9	5556	4.69	0.15	3.5	35.344	23.3	19.1	0.532979	
Praesepe	Pr0098	7	1514.8	5569	4.63	0.15	4.5	34.196	21.3	19.8	0.663978	
Praesepe	Pr0100	7	1542.9	5722	4.66	0.15	5.0	36.249	63.7	20.1	0.000000	V
Praesepe	Pr0107	1	···	5827	4.18	−0.65	2.9	76.071	118.0	···	···	NM
Praesepe	Pr0115	1	···	6562	4.10	0.01	108.2	34.754	1073.0	···	···	FR
Praesepe	Pr0119	7	1502.9	6329	4.56	0.26	7.7	35.084	26.2	21.1	0.338741	
Praesepe	Pr0120	7	1503.1	6173	4.55	0.17	10.1	35.149	28.9	32.4	0.673519	
Praesepe	Pr0121	6	1195.9	5480	4.67	0.14	3.8	35.653	610.9	17.7	0.000000	SB
Praesepe	Pr0123	3	2.0	6251	4.66	0.25	13.0	63.339	10166.3	43.8	0.000000	SB
Praesepe	Pr0125	14	737.0	6000	4.50	···	···	35.120	121.0	43.9	0.000000	D
Praesepe	Pr0126	7	1525.9	5030	4.64	0.19	3.8	34.968	11.6	20.6	0.988500	
Praesepe	Pr0128	7	1519.9	6069	4.54	0.13	8.8	34.971	25.2	32.0	0.766904	
Praesepe	Pr0133	7	1510.9	6144	4.58	0.19	9.1	34.114	41.0	28.9	0.156962	
Praesepe	Pr0135	1	···	6952	4.03	−0.01	47.7	34.592	959.0	···	···	FR
Praesepe	Pr0136	7	1520.9	5570	4.69	0.15	4.6	34.624	25.6	21.0	0.467237	
Praesepe	Pr0138	7	1503.1	6390	4.40	0.10	10.0	34.300	25.2	36.4	0.908220	
Praesepe	Pr0143	1	···	0	0.00	0.00	0.0	0.000	···	···	···	FR
Praesepe	Pr0147	1	···	6611	4.30	0.22	77.0	30.970	1125.0	···	···	FR
Praesepe	Pr0149	8	1529.0	5526	4.76	0.17	4.8	34.932	52.8	24.8	0.001777	
Praesepe	Pr0157	47	1574.8	5875	4.60	0.15	6.7	34.169	143.2	20.1	0.000000	V
Praesepe	Pr0160	7	1542.8	5641	4.65	0.17	1.0	34.919	18.7	19.7	0.762116	
Praesepe	Pr0162	7	1524.8	5338	4.69	0.20	4.0	34.619	32.3	28.4	0.185474	
Praesepe	Pr0163	2	1.1	5768	4.49	−0.04	1.1	74.809	37.8	29.6	0.262274	NM
Praesepe	Pr0164	5	75.0	5622	4.63	0.14	1.6	33.299	4668.9	20.8	0.000000	SB
Praesepe	Pr0165	7	1514.0	5602	4.66	0.13	3.7	34.456	20.5	22.2	0.818060	
Praesepe	Pr0168	40	1536.9	5715	4.60	0.07	7.3	34.790	316.8	20.4	0.000000	V
Praesepe	Pr0169	7	1567.7	5752	4.64	0.15	5.2	34.516	24.7	20.9	0.518603	
Praesepe	Pr0172	31	1549.9	5700	4.63	0.12	5.2	35.746	48.6	21.2	0.000000	V
Praesepe	Pr0173	7	1518.9	5908	4.58	0.14	6.8	35.143	19.4	23.6	0.812103	
Praesepe	Pr0174	7	1525.9	5369	4.66	0.13	4.4	35.174	24.0	24.1	0.813975	
Praesepe	Pr0177	7	1516.9	5349	4.68	0.16	2.8	34.781	16.4	22.4	0.866096	
Praesepe	Pr0179	2	51.8	5000	4.50	···	···	···	314.6	46.8	0.000000	D
Praesepe	Pr0185	2	1.0	5494	4.67	−0.13	1.4	36.014	13.1	18.6	0.591972	NM
Praesepe	Pr0194	7	1543.8	5568	4.59	0.13	1.3	34.615	29.1	14.0	0.102091	
Praesepe	Pr0201	59	1564.9	6202	4.53	0.18	8.0	33.966	52.9	19.6	0.000000	V
Praesepe	Pr0202	7	1511.0	6370	4.52	0.19	12.3	34.440	20.0	31.7	0.889251	
Praesepe	Pr0203	3	4.1	6078	4.26	−0.16	5.3	40.225	40.6	26.2	0.226867	NM
Praesepe	Pr0206	7	1525.9	5432	4.72	0.17	3.8	35.544	24.6	21.5	0.537354	
Praesepe	Pr0208	7	1539.9	5936	4.62	0.18	6.1	33.630	14.9	17.0	0.847629	
Praesepe	Pr0210	7	1566.8	5797	4.58	0.12	4.7	33.604	39.7	24.4	0.062173	
Praesepe	Pr0211	62	1483.1	5362	4.72	0.18	4.9	34.959	266.8	19.7	0.000000	V
Praesepe	Pr0218	1	···	6725	4.33	0.11	158.6	37.666	···	···	···	FR
Praesepe	Pr0219	2	48.8	5289	4.61	0.18	3.3	29.319	6.6	30.4	0.846987	NM
Praesepe	Pr0222	26	1510.9	5399	4.68	0.17	3.3	35.281	72.3	27.0	0.000000	V
Praesepe	Pr0223	1	···	6545	4.33	0.01	58.6	34.551	···	···	···	FR
Praesepe	Pr0225	7	1542.8	5621	4.69	0.14	4.7	34.864	35.0	17.7	0.041428	V
Praesepe	Pr0226	2	48.9	5000	4.50	···	···	···	6761.3	130.0	0.000000	D
Praesepe	Pr0227	1	···	6372	4.33	0.02	69.8	40.934	···	···	···	FR
Praesepe	Pr0228	1	···	5000	4.50	···	···	···	···	···	···	D
Praesepe	Pr0232	7	1516.9	5365	4.65	0.13	0.7	33.871	20.0	20.0	0.675943	
Praesepe	Pr0235	7	1491.9	5614	4.71	0.14	4.8	34.084	31.3	19.0	0.084972	

Cluster	Name	$N_{\rm obs}$	ΔT[a] (days)	$T_{\rm eff}$[b] (K)	$\log g$ (dex)	[m/H] (dex)	$v \sin i_\star$ ($\rm km\,s^{-1}$)	$v_{\rm abs}$[c] ($\rm km\,s^{-1}$)	$\sigma_{\rm obs}$[d] ($\rm m\,s^{-1}$)	$\sigma_{\rm RV}$[e] ($\rm m\,s^{-1}$)	$P(\chi^2)$	Comments[f]
Praesepe	Pr0240	1	···	4846	3.11	−0.11	3.0	72.399	···	···	···	NM
Praesepe	Pr0246	1	···	6418	4.32	0.13	26.3	34.624	···	···	···	FR
Praesepe	Pr0253	7	1527.8	5513	4.71	0.17	2.5	34.059	20.7	26.7	0.871854	
Praesepe	Pr0254	1	···	6555	4.16	−0.03	85.4	32.939	···	···	···	FR
Praesepe	Pr0255	7	1511.0	6513	4.23	0.08	6.5	33.838	27.7	30.2	0.500301	
Praesepe	Pr0259	8	1511.8	6192	4.45	0.12	9.0	33.392	34.0	26.4	0.320713	
Praesepe	Pr0260	2	1.0	5421	4.58	0.32	6.6	19.840	11944.0	17.4	0.000000	SB
Praesepe	Pr0264	1	···	6602	3.49	−0.14	87.0	34.634	···	···	···	FR
Praesepe	Pr0266	7	1517.0	6080	4.53	0.14	8.7	33.686	38.1	28.0	0.143736	
Praesepe	Pr0269	7	1185.8	6130	4.55	0.13	10.8	34.420	41.0	23.3	0.061365	
Praesepe	Pr0270	2	48.9	5563	4.47	0.27	0.8	15.741	5.5	29.5	0.869058	NM
Praesepe	Pr0272	7	1542.0	5686	4.58	0.12	4.3	33.819	25.9	18.0	0.330238	
Praesepe	Pr0274	7	1517.0	5539	4.69	0.16	2.4	33.720	20.8	24.2	0.845285	
Praesepe	Pr0276	1	···	6536	3.74	−0.08	108.7	30.970	···	···	···	FR
Praesepe	Pr0277	7	1565.8	5786	4.52	0.07	2.1	33.337	21.1	18.6	0.535589	
Praesepe	Pr0025	1	···	5000	4.50	0.00	4.0	36.480	100.0	···	···	
Praesepe	Pr0029	1	···	4750	4.00	0.00	4.0	36.645	100.0	···	···	
Praesepe	Pr0033	1	···	5000	4.50	0.00	2.0	36.063	100.0	···	···	
Praesepe	Pr0039	1	···	4750	4.00	0.00	4.0	36.566	100.0	···	···	
Praesepe	Pr0057	1	···	5000	4.00	0.00	6.0	36.375	100.0	···	···	
Praesepe	Pr0060	1	···	5000	4.50	0.00	4.0	36.194	100.0	···	···	
Praesepe	Pr0063	1	···	5000	4.50	0.00	4.0	35.352	100.0	···	···	
Praesepe	Pr0069	1	···	5000	4.50	0.00	4.0	36.099	100.0	···	···	
Praesepe	Pr0073	1	···	5000	4.50	0.00	0.0	35.046	100.0	···	···	
Praesepe	Pr0091	1	···	5250	5.00	0.00	2.0	35.657	100.0	···	···	
Praesepe	Pr0108	1	···	5250	4.50	0.00	4.0	36.149	100.0	···	···	
Praesepe	Pr0109	1	···	5250	5.00	0.00	0.0	35.708	100.0	···	···	
Praesepe	Pr0113	1	···	5000	4.50	0.00	4.0	36.595	100.0	···	···	
Praesepe	Pr0122	1	···	5250	5.00	0.00	0.0	35.716	100.0	···	···	
Praesepe	Pr0134	1	···	5000	4.50	0.00	4.0	35.696	100.0	···	···	
Praesepe	Pr0180	1	···	5250	5.00	0.00	2.0	35.355	100.0	···	···	
Praesepe	Pr0190	5	712.1	4941	4.71	0.20	3.9	34.931	71.7	50.3	0.030741	
Praesepe	Pr0230	1	···	5000	4.00	0.00	4.0	42.531	100.0	···	···	NM?, SB?
Praesepe	Pr0239	1	···	5250	5.00	0.00	1.0	35.299	100.0	···	···	
Praesepe	Pr0244	1	···	5000	4.50	0.00	4.0	35.805	100.0	···	···	
Praesepe	Pr0248	1	···	5000	4.00	0.00	4.0	34.967	100.0	···	···	
Praesepe	Pr0249	1	···	4750	4.00	0.00	4.0	35.807	100.0	···	···	
Praesepe	Pr0252	1	···	5000	5.00	0.00	0.0	35.405	100.0	···	···	
Praesepe	Pr0261	1	···	4750	4.00	0.00	2.0	34.805	100.0	···	···	
Praesepe	Pr0285	1	···	5500	4.50	0.00	6.0	36.389	100.0	···	···	
Praesepe	Pr0286	1	···	4750	4.00	0.00	4.0	36.036	100.0	···	···	
Praesepe	Pr0287	1	···	5000	4.50	0.00	4.0	36.330	100.0	···	···	
Hyades	+23755	9	1139.1	4701	4.41	−0.13	1.7	41.551	17.3	9.8	0.510291	
Hyades	AK2-1315	7	1119.0	4184	4.40	−0.32	2.0	42.067	20.0	19.2	0.643857	
Hyades	G7-227	7	1099.0	4527	4.62	−0.12	1.7	40.157	22.4	12.7	0.295584	
Hyades	G7-73C	7	1058.1	4803	3.23	0.21	2.9	37.430	38.4	24.0	0.030854	
Hyades	G8-64	7	1128.1	4837	4.55	0.04	4.3	40.807	23.6	13.2	0.216142	
Hyades	H111	9	1208.8	4546	4.69	−0.16	2.1	39.371	88.6	16.2	0.000000	V
Hyades	H210	7	1190.9	5026	4.71	−0.24	0.6	37.149	12.5	22.8	0.971775	
Hyades	H24098C	7	86.8	4992	4.70	−0.11	0.9	35.410	45.0	20.9	0.035836	
Hyades	H246	7	1077.2	6683	4.39	0.11	22.1	38.962	42.9	64.0	0.557042	
Hyades	H342	10	1150.9	4925	4.67	0.11	1.5	39.598	23.1	13.2	0.331584	
Hyades	H422	7	1120.0	4277	4.48	−0.20	2.5	40.624	25.7	14.5	0.199830	
Hyades	H469	7	1077.2	6506	4.38	0.08	33.4	38.939	44.0	64.3	0.791847	
Hyades	H472	10	1190.7	4728	4.66	0.11	1.9	39.626	13.7	9.6	0.827949	
Hyades	J202A	8	1120.1	4187	4.43	−0.30	2.2	29.728	40.6	22.5	0.128156	
Hyades	L101	8	1139.0	4474	4.12	−0.08	3.9	43.202	16.3	10.1	0.653938	
Hyades	L15	47	1246.8	4503	4.67	0.13	3.2	38.149	92.4	10.3	0.000000	V
Hyades	L18	8	1128.1	5334	4.90	0.19	2.0	36.569	23.1	14.6	0.282060	
Hyades	L26	7	1087.0	4543	4.68	−0.10	2.3	38.284	27.9	11.1	0.119662	
Hyades	L38	7	1152.7	4352	4.44	−0.22	3.0	38.848	22.8	13.7	0.372984	
Hyades	L58	11	1102.0	4264	4.47	−0.30	2.6	39.338	22.4	15.2	0.399249	

Cluster	Name	$N_{\rm obs}$	ΔT[a] (days)	$T_{\rm eff}$[b] (K)	$\log g$ (dex)	[m/H] (dex)	$v \sin i_\star$ ($\rm km\,s^{-1}$)	$v_{\rm abs}$[c] ($\rm km\,s^{-1}$)	$\sigma_{\rm obs}$[d] ($\rm m\,s^{-1}$)	$\sigma_{\rm RV}$[e] ($\rm m\,s^{-1}$)	$P(\chi^2)$	Comments[f]
Hyades	L7	7	1149.8	4306	4.49	−0.24	2.0	35.631	15.3	13.5	0.779622	
Hyades	L96	9	1179.7	4530	4.24	−0.09	3.6	41.683	26.5	9.2	0.054488	
Hyades	VB116	10	1452.0	5511	4.81	0.17	4.0	41.632	22.9	15.2	0.360742	
Hyades	VB128	7	1079.0	6528	4.37	0.07	34.9	42.159	91.3	75.6	0.094462	
Hyades	VB13	7	1077.2	6597	4.25	0.07	28.7	36.896	63.5	48.6	0.044225	
Hyades	VB14	23	54.0	0	0.00	0.00	0.0	0.000	609.1	18.2	0.000000	D
Hyades	VB86	7	1078.1	6396	4.30	−0.01	32.6	40.335	57.6	46.9	0.256333	
ComaBer	CB0001	7	1093.0	5485	4.71	−0.07	3.7	0.573	28.5	15.2	0.130842	
ComaBer	CB0002	22	1082.0	4878	4.77	−0.04	1.3	1.542	391.0	17.2	0.000000	SB
ComaBer	CB0003	1	···	4891	3.07	−0.31	12.7	29.361	···	···	···	NM
ComaBer	CB0004	7	1093.1	5626	4.66	−0.10	4.6	0.101	18.5	17.2	0.677005	
ComaBer	CB0005	1	···	4937	2.23	−0.73	6.5	38.191	···	···	···	NM
ComaBer	CB0006	1	···	4629	2.71	−0.27	2.2	−14.553	···	···	···	NM
ComaBer	CB0007	3	819.8	4984	4.70	−0.11	1.9	−12.084	773.0	15.5	0.000000	SB
ComaBer	CB0008	1	···	4902	3.08	−0.17	4.6	54.546	···	···	···	NM
ComaBer	CB0009	7	1093.1	5914	4.58	−0.06	6.3	0.370	27.1	20.7	0.395907	
ComaBer	CB0010	7	1099.1	5015	4.74	−0.10	3.0	0.762	21.4	13.2	0.448558	
ComaBer	CB0011	8	1085.0	6561	4.21	−0.11	21.0	−0.093	73.6	62.4	0.228906	
ComaBer	CB0012	11	1078.1	4954	4.78	−0.05	1.9	0.546	37.8	17.2	0.016301	
ComaBer	CB0013	3	819.8	6497	4.21	−0.11	49.8	4.160	3661.0	168.5	0.000000	SB, FR
ComaBer	CB0014	1	···	4960	3.01	−0.10	4.4	20.336	···	···	···	NM
ComaBer	CB0015	2	783.9	6551	3.91	−0.04	20.6	−2.930	545.0	109.9	0.000000	NM, D
ComaBer	CB0016	1	···	4747	2.38	−0.56	3.4	−25.569	···	···	···	NM
ComaBer	CB0017	1	···	5225	3.62	−0.36	0.5	17.092	···	···	···	NM
ComaBer	CB0018	1	···	6804	4.18	−0.11	65.7	−0.131	···	···	···	FR
ComaBer	CB0019	1	···	4866	2.78	−0.55	2.3	−66.920	···	···	···	NM
ComaBer	CB0022	33	1114.9	6236	4.43	−0.11	17.2	0.398	663.0	44.7	0.000000	V
ComaBer	CB0023	7	1095.9	6033	4.51	−0.11	9.4	−0.803	27.5	26.7	0.427823	
ComaBer	CB0024	7	1095.9	6122	4.50	−0.05	9.7	−0.979	30.2	19.2	0.160774	
ComaBer	CB0025	8	1078.1	4924	4.80	−0.03	1.9	0.308	44.8	15.4	0.000863	V
ComaBer	CB0026	7	1095.9	6002	4.51	−0.09	6.6	−0.023	29.4	19.9	0.227457	
ComaBer	CB0027	9	1086.0	6398	4.39	−0.08	21.3	−0.198	57.8	43.7	0.101471	
ComaBer	CB0028	8	1086.0	6364	4.32	−0.09	17.1	−0.186	61.1	42.7	0.120004	
ComaBer	CB0029	25	1114.9	6268	4.47	0.01	22.6	−0.542	87.0	55.1	0.000070	V
ComaBer	CB0030	1	···	4584	2.60	−0.35	2.9	12.066	···	···	···	NM
ComaBer	CB0031	1	···	4653	2.04	−1.32	5.0	−15.009	···	···	···	NM
ComaBer	CB0032	1	···	4622	2.22	−0.96	3.4	79.280	···	···	···	NM
ComaBer	CB0033	1	···	4840	2.75	−0.45	2.5	15.459	···	···	···	NM
ComaBer	CB0034	7	1062.2	4552	4.65	−0.23	1.7	0.282	34.2	22.0	0.171846	
ComaBer	CB0035	1	···	4943	2.83	−0.17	3.3	−17.546	···	···	···	NM
ComaBer	CB0036	103	1114.9	6411	4.22	−0.13	28.9	−0.490	109.9	43.3	0.000000	V
ComaBer	CB0037	7	1099.0	4834	4.72	−0.09	2.5	0.638	33.4	15.7	0.052400	
ComaBer	CB0038	7	1095.9	5465	4.69	−0.08	1.3	−0.015	29.1	12.3	0.084645	
ComaBer	CB0039	1	···	4739	2.81	−0.25	2.7	32.347	···	···	···	NM
ComaBer	CB0040	1	···	5264	2.87	−0.71	6.0	62.711	···	···	···	NM
ComaBer	CB0041	1	···	4930	2.67	−0.46	4.3	58.953	···	···	···	NM
ComaBer	CB0042	1	···	4992	3.10	−0.46	1.4	20.655	···	···	···	NM
ComaBer	CB0043	2	785.8	6067	4.18	−0.27	112.5	0.680	4530.0	100.0	0.000044	D
ComaBer	CB0044	1	···	4917	3.31	−0.27	1.3	44.347	···	···	···	NM
ComaBer	CB0045	8	1086.0	6353	4.32	−0.11	16.6	−0.444	65.2	52.4	0.061672	
ComaBer	CB0046	8	1086.0	6405	4.21	−0.07	17.9	−0.113	23.2	37.6	0.911214	
ComaBer	CB0047	1	···	4865	2.92	−0.50	2.3	68.904	···	···	···	NM
ComaBer	CB0048	7	1062.2	4587	4.53	−0.21	2.7	0.438	36.8	20.5	0.029946	
ComaBer	CB0049	1	···	5129	3.55	0.01	2.1	−5.629	···	···	···	NM
ComaBer	CB0050	7	1096.0	5760	4.58	−0.07	3.9	−0.244	18.4	12.8	0.572728	
ComaBer	CB0051	7	1095.1	5470	4.71	−0.07	3.6	0.506	16.3	15.6	0.850589	
ComaBer	CB0052	7	1132.9	5756	4.58	−0.07	4.4	−0.171	10.5	19.2	0.978713	
ComaBer	CB0053	7	1132.9	5440	4.67	−0.09	1.4	0.249	26.0	11.8	0.162063	
ComaBer	CB0054	1	···	5144	3.40	−0.44	1.8	−43.820	···	···	···	NM
ComaBer	CB0055	7	1127.0	5263	4.86	−0.02	3.0	0.568	27.4	14.8	0.174263	
ComaBer	CB0057	1	···	5021	2.55	−0.83	7.2	61.227	···	···	···	NM
ComaBer	CB0058	8	1086.0	6352	4.36	−0.07	19.5	−0.495	77.2	53.7	0.155102	

Cluster	Name	$N_{\rm obs}$	ΔT[a] (days)	$T_{\rm eff}$[b] (K)	$\log g$ (dex)	[m/H] (dex)	$v \sin i_\star$ ($\rm km\,s^{-1}$)	$v_{\rm abs}$[c] ($\rm km\,s^{-1}$)	$\sigma_{\rm obs}$[d] ($\rm m\,s^{-1}$)	$\sigma_{\rm RV}$[e] ($\rm m\,s^{-1}$)	$P(\chi^2)$	Comments[f]
ComaBer	CB0059	1	···	4940	3.32	−0.04	2.1	−4.707	···	···	···	NM
ComaBer	CB0060	1	···	5034	3.48	−0.14	0.7	−39.825	···	···	···	NM
ComaBer	CB0061	7	1133.9	5870	4.63	−0.09	6.0	−1.150	12.6	20.7	0.962518	
ComaBer	CB0062	7	1100.0	4987	4.80	−0.03	0.7	0.073	20.0	14.1	0.430416	
ComaBer	CB0063	8	1162.8	5493	4.67	−0.11	3.5	−2.080	38.9	14.4	0.001619	V
ComaBer	CB0064	1	···	4647	2.69	−0.36	2.3	67.568	···	···	···	NM
ComaBer	CB0065	26	807.0	5392	4.66	−0.10	3.5	−0.017	21.0	13.8	0.000000	SB
ComaBer	CB0067	2	785.9	6101	3.93	0.05	9.0	−19.090	17.9	26.3	0.560116	NM
ComaBer	CB0068	1	···	4782	2.73	0.01	4.9	−3.089	···	···	···	NM
ComaBer	CB0070	7	1150.9	5990	4.51	−0.11	9.0	−1.553	28.0	32.9	0.649854	
ComaBer	CB0071	3	822.8	6341	4.04	0.20	15.4	−2.436	833.0	28.1	0.000000	NM?, SB
ComaBer	CB0072	1	···	5190	3.57	−0.25	1.3	44.325	···	···	···	NM
ComaBer	CB0073	1	···	4808	2.55	−0.28	4.0	−8.225	···	···	···	NM
ComaBer	CB0074	1	···	5142	3.80	0.20	1.5	−9.749	···	···	···	NM
ComaBer	CB0075	1	···	4851	3.11	0.28	3.5	−22.557	···	···	···	NM
ComaBer	CB0076	1	···	5033	2.68	−0.54	4.0	19.012	···	···	···	NM
ComaBer	CB0077	1	···	5450	3.39	−1.08	9.6	163.332	···	···	···	NM
ComaBer	CB0078	1	···	4925	2.95	−0.55	2.1	−47.323	···	···	···	NM
ComaBer	CB0079	2	1.0	4928	2.87	−0.37	2.3	1.243	18.6	10.0	0.324409	NM
ComaBer	CB0080	1	···	4904	3.04	−0.12	4.3	15.474	···	···	···	NM
ComaBer	CB0081	1	···	4817	3.12	−0.28	1.2	31.397	···	···	···	NM
ComaBer	CB0082	3	776.9	4572	4.72	−0.23	2.8	−10.114	3910.0	30.6	0.000000	NM?, D
ComaBer	CB0083	1	···	4657	2.97	−0.34	21.1	−28.390	···	···	···	NM
ComaBer	CB0084	1	···	5270	3.74	−0.12	0.0	−25.283	···	···	···	NM
ComaBer	CB0085	8	1086.0	6204	4.40	−0.08	12.0	−0.664	32.9	32.8	0.482542	
ComaBer	CB0086	69	1161.8	5605	4.69	−0.08	4.6	−1.554	1174.8	15.9	0.000000	SB
ComaBer	CB0087	1	···	4916	2.87	−0.39	2.2	−18.592	···	···	···	NM
UrsaMajor	HD109011	17	360.0	5131	4.76	−0.08	4.4	−11.871	2125.3	51.6	0.000000	SB
UrsaMajor	HD109647	7	243.3	5069	4.76	−0.03	0.9	−8.523	11.2	15.4	0.946712	
UrsaMajor	HD110463	7	243.3	5042	4.77	−0.05	1.0	−9.631	13.8	15.7	0.871477	
UrsaMajor	HD11131	5	17.0	5898	4.57	−0.09	3.0	−3.958	25.3	10.5	0.151196	
UrsaMajor	HD115043	7	243.3	5972	4.60	−0.06	7.9	−8.590	33.5	14.6	0.026894	
UrsaMajor	HD152863	7	24.2	5142	3.02	−0.24	4.3	−0.226	21.6	9.6	0.233809	
UrsaMajor	HD155674	6	24.2	4447	4.05	−0.29	4.1	3.378	30.4	29.3	0.522754	
UrsaMajor	HD155674	6	24.2	4382	4.51	−0.31	2.0	2.554	27.2	23.8	0.548432	
UrsaMajor	HD167389	7	24.2	5932	4.46	−0.05	4.2	−5.537	18.0	16.4	0.655193	
UrsaMajor	HD184960	7	24.0	6198	4.05	−0.15	9.2	0.635	25.9	11.1	0.116775	
UrsaMajor	HD205435	7	19.1	5252	3.35	−0.17	4.3	6.836	11.2	4.7	0.851006	
UrsaMajor	HD238087	7	243.2	4309	4.47	−0.32	1.8	−9.860	25.6	28.1	0.410042	
UrsaMajor	HD238224	17	360.0	4348	4.54	−0.35	3.1	−14.840	1337.0	22.9	0.000000	V
UrsaMajor	HD24916A	5	19.0	4475	4.00	−0.34	2.9	3.737	15.5	15.4	0.704532	
UrsaMajor	HD26923	5	19.0	6036	4.46	−0.06	3.2	−7.267	16.2	10.4	0.562460	
UrsaMajor	HD28495	6	19.0	5545	4.70	−0.08	4.7	7.500	42.0	18.2	0.005277	
UrsaMajor	HD38393	5	31.9	6180	4.14	−0.17	9.2	−9.199	38.5	19.6	0.073224	
UrsaMajor	HD41593	5	34.0	5417	4.68	−0.04	3.7	−9.864	18.1	8.4	0.426610	
UrsaMajor	HD59747	4	20.0	5204	4.63	−0.07	0.6	−15.711	15.2	10.3	0.588531	
UrsaMajor	HD95650	7	246.3	3969	4.40	−0.55	2.2	−13.885	44.6	26.8	0.044667	

Notes —

(a) ΔT is the time span of observations.

(b) We reiterate that classifications of stars with temperatures cooler than about 5250 K are likely affected by systematic biases in $T_{\rm eff}$, $\log g$, and [m/H], and should be treated with caution.

(c) $v_{\rm abs}$ is the mean absolute radial velocity of the system; for stars with companions, we report the center-of-mass velocity only if it is constrained.

(d) $\sigma_{\rm obs}$ is the standard deviation of the RVs, or in the case of stars with companions, of the RV residuals to the best fit orbit or trend.

(e) $\sigma_{\rm RV}$ is the combined uncertainty stemming from internal errors, instrumental errors, and an assumed $16\,\rm m\,s^{-1}$ stellar jitter.

(f) We note systems that are non-members (NM), single-lined spectroscopic binaries (SB), double-lined (D) spectra, fast rotators (FR), or low-amplitude variables (V) according to $P(\chi^2) < 0.001$ or a visual evaluation of a linear trend.

3.2.5 Praesepe Data

Observations of Praesepe stars began UT 2012 Jan 06 and have continued through UT 2016 May 05. As indicated in Table 3.1, a total of 115 Praesepe stars were observed at least once. In total, 775 spectra were obtained for an average of 6.7 spectra per star, though not all stars received the same attention. The typical star has between 7 and 9 observations spread across three observing seasons (with a total time span of about 4 years), but a handful of stars have been observed in excess of 20 times each, and other targets were abandoned after only a few spectra: 24 stars initially had an unknown $v \sin i_\star$ and 12 of these were abandoned upon discovery of rapid rotation; by monitoring RV variations, 5 stars were quickly found to be spectroscopic binaries; observations of 4 other stars reveal composite spectra also indicative of stellar companions (or possibly chance alignments of background or foreground stars that render precise RV measurements hopeless); and 13 proved to be non-members through analysis of the RVs and/or the stellar atmospheric properties. Another 27 faint stars ($V > 12$) were only observed once to assess their suitability for future surveys that may extend to later types. We obtained full data sets for 55 stars. Plots of the number of observations per star and the velocity dispersions are shown in Figure 3.3. We analyze the velocities in search of companions in Chapters 4 and 6.

3.2.6 Hyades Data

Observations of Hyades stars began UT 2012 Sep 23 and have continued through UT 2016 Feb 25. A total of 27 Hyades stars—all previously confirmed members with slow rotation—

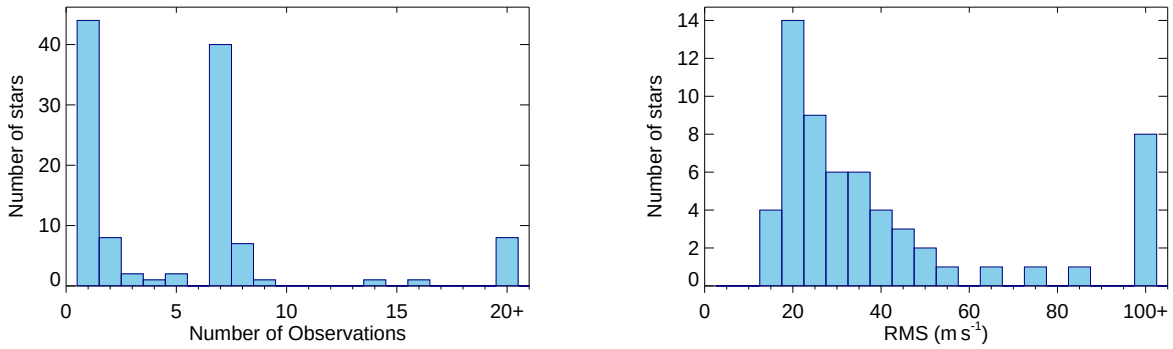

Figure 3.3 Plots showing the number of observations per star (left) and the RMS velocity dispersions (right) for Praesepe stars.

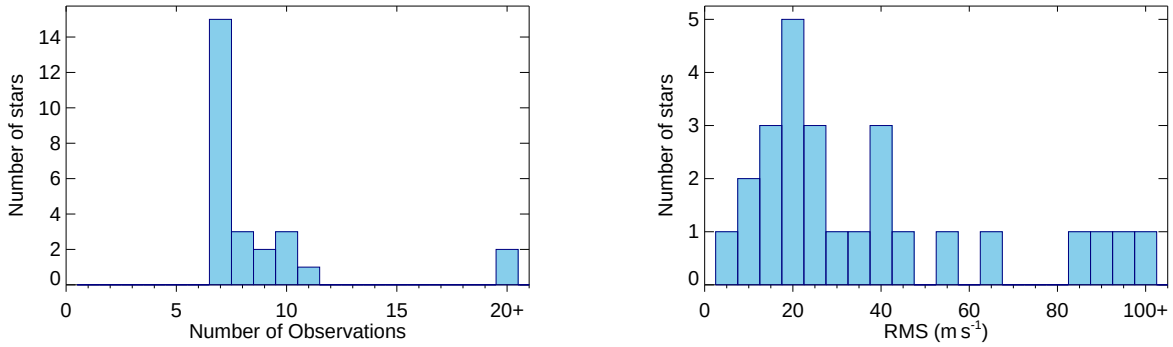

Figure 3.4 Plots showing the number of observations per star (left) and the RMS velocity dispersions (right) for Hyades stars.

were observed. A total of 258 observations were obtained, for an average of 9.9 per star. One star appears to have one or more stellar companions with short orbital period, so 26 stars received full attention in the survey. As with Praesepe, the average number of observations is skewed by outliers, and the typical star was observed 7 times. Plots of the observations per star and the RV dispersions are shown in Figure 3.4.

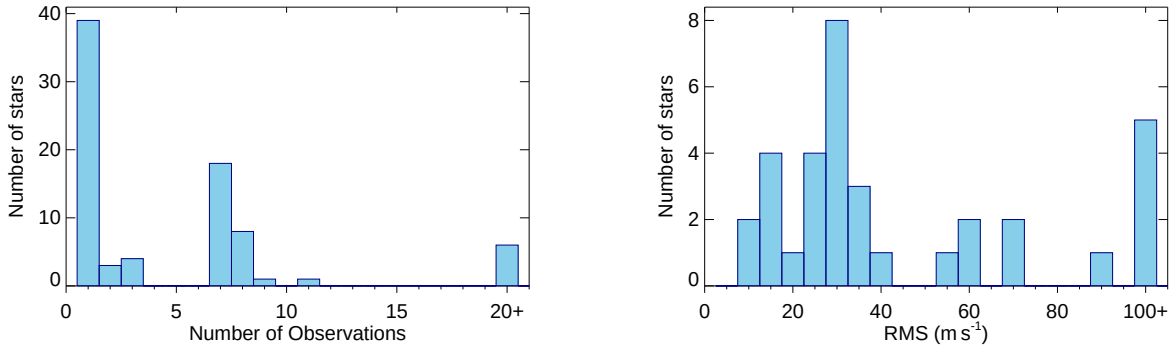

Figure 3.5 Plots showing the number of observations per star (left) and the RMS velocity dispersions (right) for Coma Berenices stars.

3.2.7 Coma Berenices Data

Observations of Coma Berenices stars began UT 2013 Feb 17 and have continued through UT 2016 May 04. A total of 82 stars were observed at least once. 43 were rejected as non-members, 6 more display large RV variations or evidence for composite spectra that are indicative of a stellar companion, and 1 was rotating too rapidly for precise RVs. This leaves 34 likely cluster members that we surveyed fully, 7 of which show variation that may indicate the presence of a stellar, brown dwarf, or planetary companion. 550 total spectra were taken, an average of 6.5 per star, though this is affected by the large number of single observations and a handful of targets that received significantly more observations. Once again, the typical star received 7–9 observations. Plots of the observations per star and the RV dispersions are shown in Figure 3.5. We also show a CMD and a spectroscopic H-R diagram in Figure 3.6, illustrating how our SPC classifications helped us distinguish non-members, even when their RVs were consistent with membership.

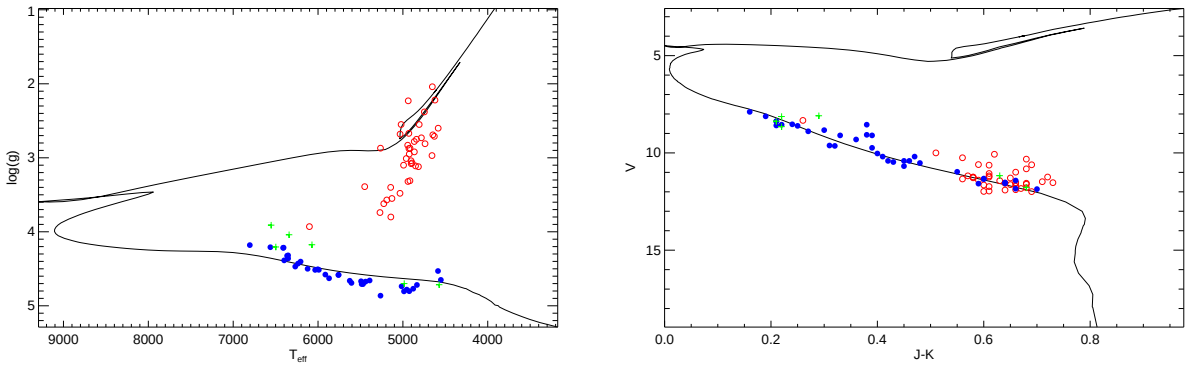

Figure 3.6 Left: A spectroscopic H-R diagram for our Coma Berenices targets, showing $\log g$ versus $T_{\rm eff}$ overplotted on a 600 Myr isochrone. The background giants (red open circles) are immediately apparent above the main sequence, near which the true members (blue filled circles) lie—note that the small, apparently systematic deviations from the main sequence are likely due to degeneracies in the (unconstrained) SPC fits. Also plotted are double-lined systems (green crosses), for which the classifications may not be reliable. Right: The same CMD that was plotted in Figure 2.2, but now with the color scheme from the left panel. It is clear that stars cooler than about 5250 K in the field of the Coma Berenices cluster are very likely to be background giants. As a result, our final target list is made up of mostly earlier types (mid-F to early-G).

3.2.8 Ursa Major Data

Observations of Ursa Major stars began UT 2015 May 01 and have continued through UT 2016 May 04. A total of 20 stars were observed. Some have only received one season of short cadence observations thus far, while others have also been observed a year later. A total of 144 spectra have been taken, with most stars receiving 5–7 observations. Plots of the observations per star and the RV dispersions are shown in Figure 3.7.

3.2.9 Variability Statistics and Stellar Jitter

Finally, we note that using the observed dispersions and the internal errors, we may be able to estimate the stellar jitter for this population of adolescent (500-625) clusters. In principle,

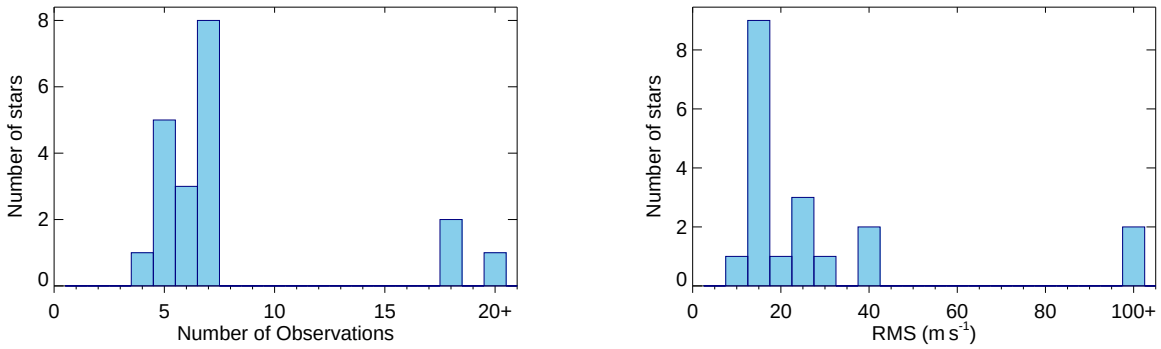

Figure 3.7 Plots showing the number of observations per star (left) and the RMS velocity dispersions (right) Ursa Major stars.

the stellar jitter for each star is simply given by $\sigma_\star = \sqrt{\sigma^2_{\rm obs} - \sigma^2_{\rm int} - \sigma^2_{\rm TRES}}$, but some practical limitations complicate matters. First of all, the observed RV dispersion is sometimes, by chance, smaller than the measurement errors. This issue is further compounded in our survey by the fact that the internal measurement errors and the instrumental errors are of similar magnitude (or greater than) the expected stellar jitter; if stellar jitter were expected to be the dominant term, very few stars would exhibit smaller RV dispersions than their uncertainties and we could have calculated the stellar jitter for all of the stars more readily. Similarly, because stellar jitter contributes only in small part to the total dispersion, any systematic bias in the other quantities will be more likely to significantly affect our calculation of jitter. For example, if our measurement errors or instrumental jitter are overestimated even slightly, we will derive a stellar jitter that is too small. With these cautions in mind, we calculate the jitter for each star, setting those with "negative jitter" to 0. The median of all stars without companions (i.e., those with $P(\chi^2) > 0.001$) is $\sigma_\star = 11\,{\rm m\,s^{-1}}$. We plot the distribution of derived jitter as well as the ratio of external (observed) to internal errors in

Figure 3.8. The latter plot allows us to confirm that the error distributions are approximately normal (excluding the most extreme variables in the last bin), with a peak just greater than 1. This is expected for a population of stars like ours, for which modest stellar jitter should slightly inflate the observed dispersion.

While this value of jitter is roughly in agreement with the value previously derived for the Hyades ($16\,\mathrm{m\,s^{-1}}$ Paulson et al. 2004b), it is slightly lower. This could be a function of the different stellar populations considered. For example, we surveyed a different distribution of stellar masses, with which stellar jitter is expected to vary. This highlights that the properties of the stellar sample can impact a survey in many ways. In particular, it shows that characterization of stellar jitter as a function of spectral type may be important, not only for the general understanding of stellar astrophysics at young ages, but also for optimizing the designs of future surveys of young stars. That said, the ages of our stars are on average slightly younger than the Hyades and we include more rapidly rotating stars in our survey, both of which would lead us to predict a larger jitter, not smaller. Because of this, we cannot discount the possibility that we have very slightly overestimated our errors (internal estimates and/or instrumental jitter).

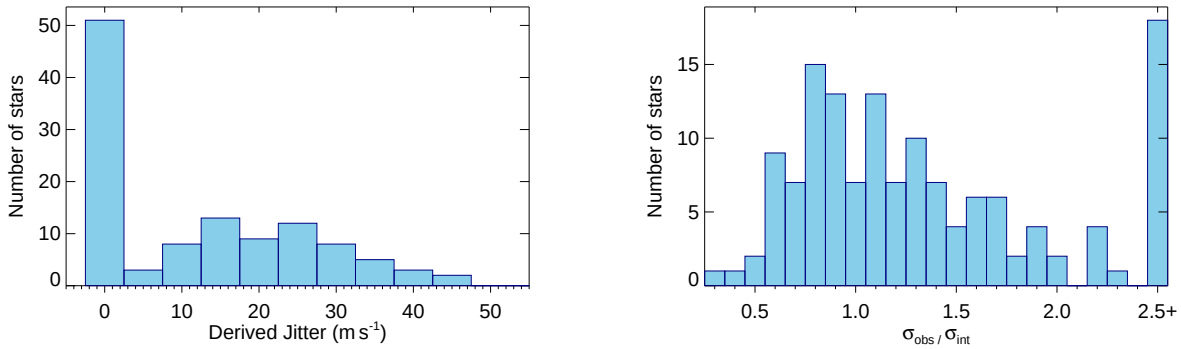

Figure 3.8 *Left*: The distribution of derived stellar jitter for our single stars in Praesepe, the Hyades, Coma Berenices, and Ursa Major. We find a median value of $11\,\mathrm{m\,s^{-1}}$. Note that while the distribution looks bimodal, this is an artifact of the argument of the square root that sometimes becomes negative due to statistical fluctuations. *Right*: The distribution of ratios of external to internal errors of all of our stars, which provides a second, and perhaps better, visual representation of the contribution of stellar jitter. Excluding the most extreme variables in the last bin, the peak of the distribution is very near 1, indicating that stellar jitter is small, and it is clear that the distribution is smooth.

CHAPTER 4
HOT JUPITERS IN OPEN CLUSTERS

4.1 Two 'b's in the Beehive

Exoplanet studies over the last 15 years have demonstrated that at least 10% of FGK stars harbor gas giant planets, with many of them at surprisingly small separations, implying inward migration after formation (Wright et al. 2011). Although the mechanism by which most planets migrate is not fully understood, powerful constraints on proposed theories of migration can be established by determining the orbital properties of planets at young or adolescent ages ($< 1\,\mathrm{Gyr}$). As was introduced in Chapter 1, if migration occurs primarily due to interactions with a circumstellar disk (e.g., Lin et al. 1996), the migration must occur before the disk dissipates ($\sim$10 Myr; Carpenter et al. 2006), and is predicted to circularize orbits. Alternatively, if migration occurs primarily due to planet-planet scattering (e.g., Adams & Laughlin 2003) or the Kozai-Lidov mechanism (e.g., Fabrycky & Tremaine 2007), the process may take hundreds of millions of years to occur and can produce highly eccentric orbits prior to any tidal circularization (see review by Lubow & Ida 2010).

A direct way to find planets that can potentially be used to constrain theories of migration is to search for them in young open clusters. However, at the start of our survey, only 2 open cluster stars were known to harbor planets—ϵ Tau in the Hyades (Sato et al. 2007) and TYC 5409-2156-1 in NGC 2423 (Lovis & Mayor 2007)—both of which are giant stars and thus, by necessity, have planets on wider orbits than those occupied by hot Jupiters. In both cases the host stars are of intermediate mass (2.7 and 2.4 $M_{\odot}$), likely A or B type stars when on the

main sequence. The lack of detected planets orbiting FGK main sequence stars (which are often referred to as Sun-like stars) in open clusters has remained despite radial velocity (RV) suveys of 94 dwarfs in the metal-rich Hyades (Paulson et al. 2004b, mean [Fe/H] = +0.13) and 58 dwarfs in M67 (Pasquini et al. 2012), as well as numerous transit searches in other clusters (e.g., Hartman et al. 2009; Pepper et al. 2008; Mochejska et al. 2006). While the lack of detections might be explained by small sample sizes (see van Saders & Gaudi 2011), millimeter-wave studies of disks around stars in the Orion star forming region, which may evolve into an open cluster, have offered a plausible astrophysical explanation. Eisner et al. (2008) find that most solar-type stars in this region do not possess disks massive enough to form gas giant planets. One may also speculate that for the few stars capable of forming planets, the remaining disk masses may be insufficient to facilitate inward migration (see also Debes & Jackson 2010).

Because hot Jupiters in young and adolescent clusters—if they exist—would offer a valuable glimpse at planets during or soon after the migration process, our initial survey in Praesepe, for which the data acquisition and analysis is described in Chapter 3, serves a dual purpose. The discovery of these planets is the primary goal, but any successes would also pave the way for future study of young planets; knowing that short-period planets do exist in clusters, investigators can carry out these surveys with confidence and, hopefully, with rejuvenated interest. In the following sections we present the seminal result of our initial survey—the discovery of the first 2 hot Jupiters in an open cluster.

4.1.1 Identification of Variability

As described in Chapter 3, we follow the example of Latham et al. (2002) and use the $P(\chi^2)$ statistic—the probability that a χ^2 value equal to or less than the observed χ^2 would be measured for a star of constant velocity—to identify variable stars. Figure 4.1 shows the distribution of these values, of which 13 lie below our threshold for follow-up ($P(\chi^2) < 0.001$, or 99.9% confidence of variability). Among these candidate variables, Lomb-Scargle periodograms revealed two stars, Pr0201 and Pr0211, with significant short period power after the initial short-cadence observations were obtained. We therefore immediately devoted additional telescope time toward their follow-up and found the RVs of both stars to be consistent with the presence of short-period planetary companions. A description of our analysis to confirm and characterize these planets follows.

4.1.2 Orbital Solutions

We used a Markov Chain Monte Carlo (MCMC) analysis to fit Keplerian orbits to the radial velocity data of Pr0201 and Pr0211, fitting for orbital period P, time of inferior conjunction $T_{\rm c}$, the radial velocity semi-amplitude K, the center-of-mass velocity γ, and the orthogonal quantities $\sqrt{e}\cos\omega$ and $\sqrt{e}\sin\omega$, where e is eccentricity and ω is the argument of periastron. Careful consideration of the error analysis is always important, but the choice of methodology for computing the errors is particularly important for a quantity such as the eccentricity, which is truncated at zero and will often result in a skewed posterior distribution. Using a the median and central 68.3% confidence interval as the best fit parameters and 1-σ errors,

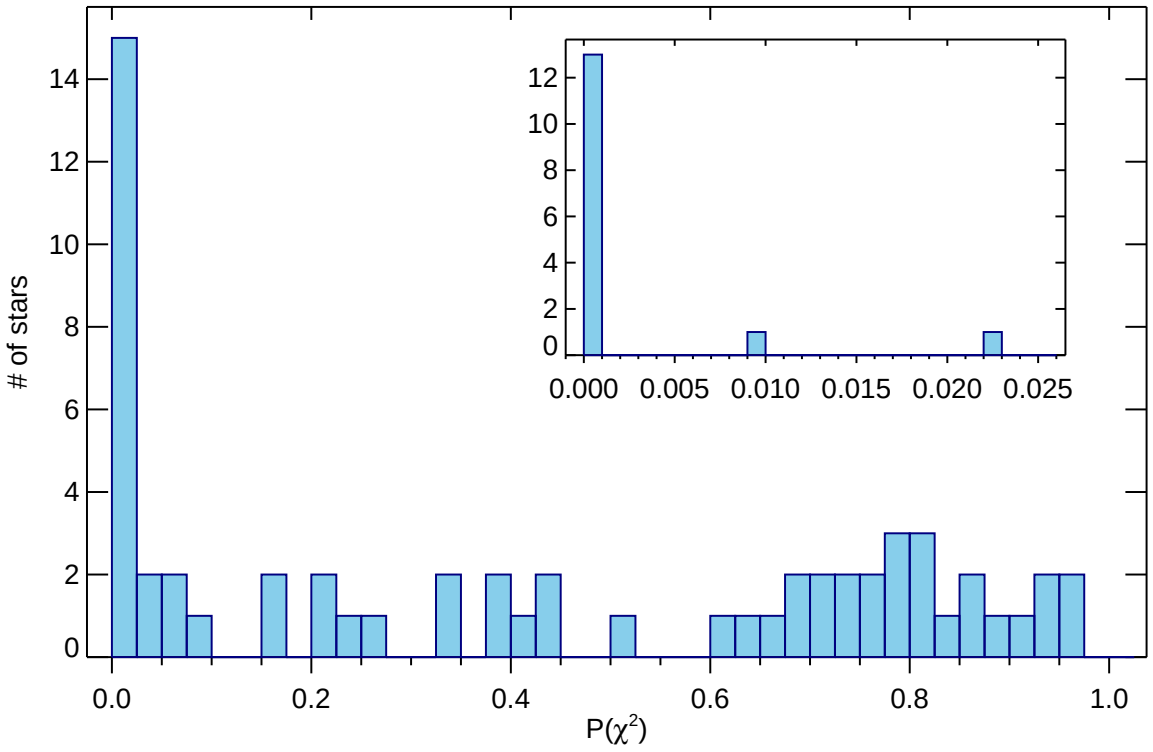

Figure 4.1 We show the $P(\chi^2)$ distribution for Praesepe stars, with the details of the first bin expanded in the inset plot. Stars with candidate companions lie in this first bin, and we dedicate the majority of our follow-up resources to these stars. It can be seen that 13 stars meet our variability criterion of $P(\chi^2) < 0.001$.

as can be done for a Gaussian posterior, would give a biased result, and we are especially interested in an accurate eccentricity because non-zero eccentricities may be evidence in favor of multi-body migration mechanisms. Instead, we adopt best fit parameters from the mode of each distribution, which we identify from the peak of the probability density function (PDF). We generate the PDFs using a Gaussian kernel density estimator with bandwidths for each parameter chosen according to Silverman's rule. We assign errors from the region that encloses 68.3% of the PDF, and for which the bounding values have identical probability

densities. That is, we require the ± 1-σ values to have equal likelihoods. This yields best-fit parameters and errors for the six MCMC parameters above, and the best-fit $\sqrt{e}\cos\omega$ and $\sqrt{e}\sin\omega$ can be converted trivially to e and ω, but we must still consider how to convert the errors in $\sqrt{e}\cos\omega$ and $\sqrt{e}\sin\omega$ to errors in e and ω. We choose to use the extent of the error ellipse in the $\sqrt{e}\cos\omega$-$\sqrt{e}\sin\omega$ plane to identify the extent of this error ellipse in e-ω space. We do this by recognizing that in this plane, e is a radial coordinate and ω an azimuthal coordinate; while the procedure becomes simple to carry out, it is best shown graphically, which we do in Figure 4.2.

The results of this exercise give eccentricities of $e = 0.079 \pm 0.078$ for Pr0201 and $0.156^{+0.041}_{-0.112}$ for Pr0211. However, it can take many precise observations to accurately measure small, non-zero eccentricities (e.g., Zakamska et al. 2011; Pont et al. 2011), and both are consistent with $e = 0$ to within 2-σ, so we advise caution to not over-interpret these results; for short period planets such as these, we expect that in the absence of additional bodies, tidal forces should have already circularized the orbits (e.g., Adams & Laughlin 2006). We report the eccentric solutions for full transparency in Table 4.1 and plot these orbits in Figure 4.3, but we note that the other orbital parameters change insignificantly if we fix $e = 0$—in the absence of additional data, the assumption of circularized orbits is acceptable.

4.1.3 Line Bisectors and Stellar Activity Indices

If the observed velocity variations were caused by a background blend (Mandushev et al. 2005) or star spots (Queloz et al. 2001), we would expect the shape of a star's line bisector to vary in phase with the radial velocities. A standard prescription for characterizing the shape

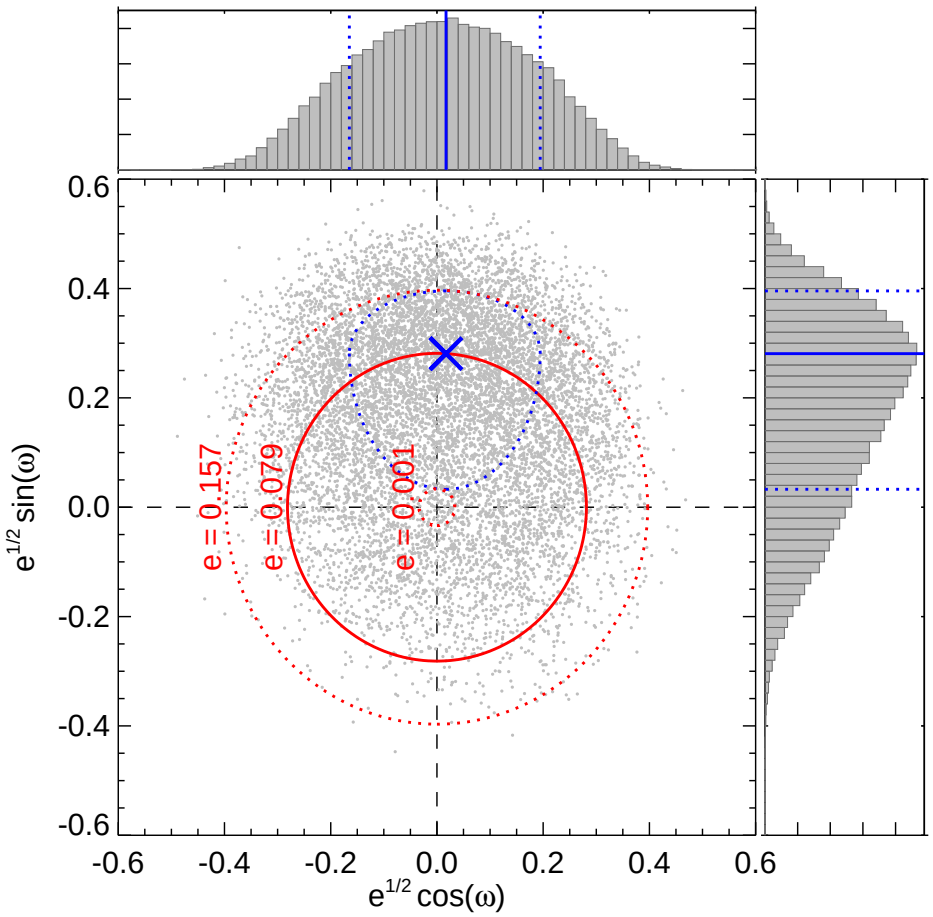

Figure 4.2 Here we show samples from the joint MCMC posterior of $\sqrt{e}\cos\omega$ and $\sqrt{e}\sin\omega$ for the Pr0201 system (gray dots). The top and right panels show the marginalized posteriors for $\sqrt{e}\cos\omega$ (top) and $\sqrt{e}\sin\omega$ (right), with blue lines indicating the mode (solid) and ±1-σ errors (dotted). These dotted lines therefore correspond to the extent of the blue dotted 1-σ error ellipse plotted on the joint posterior, which is centered on the blue "X". Any point in this plane can be trivially converted to e and ω via the equations $e = (\sqrt{e}\cos\omega)^2+(\sqrt{e}\sin\omega)^2$, $\omega = \arctan(\sqrt{e}\sin\omega/\sqrt{e}\cos\omega)$, so we find the values corresponding to the mode and the maximum and minimum values corresponding to points encompassed by the error ellipse. We show these quantities for e, which trace out the solid and dotted red circles, and note that ω for any point in the plane is given by the angle it forms with the positive x-axis (we omit these lines to prevent the plot from becoming too busy).

of a line bisector is to measure the difference in relative velocity of the top and bottom of a line bisector; this difference is referred to as a line bisector span (see, e.g., Torres et al. 2005).

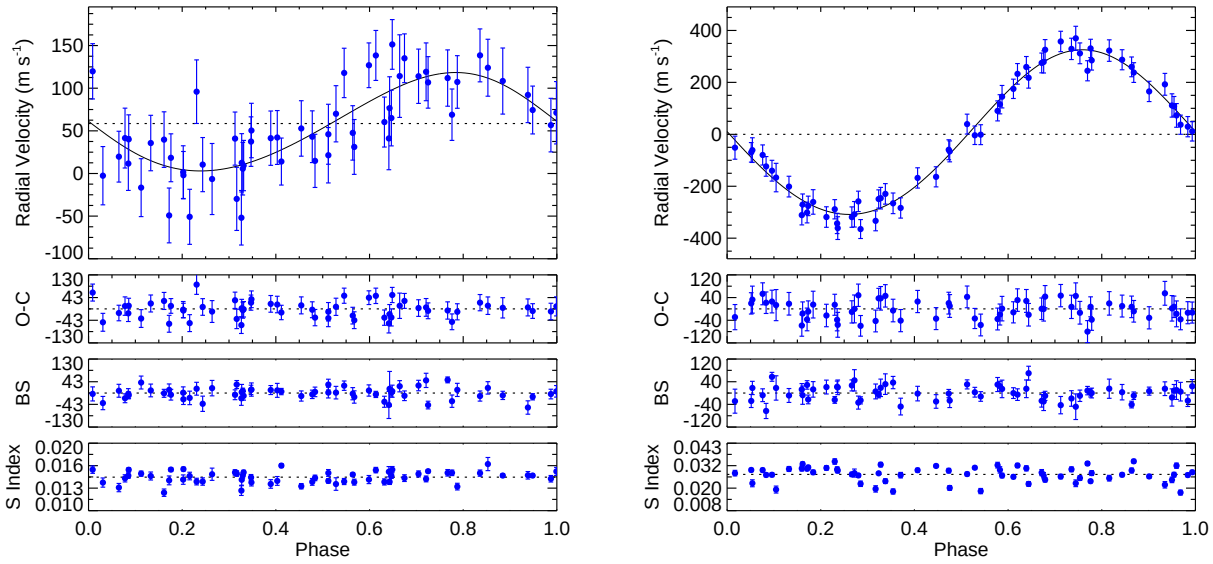

Figure 4.3 We show the orbits of the two hot Jupiters in Praesepe, Pr0201b (left) and Pr0211b (right). In each plot, the top panel shows the RVs plotted against orbital phase, and the three lower panels show, from top to bottom, the residuals to the best-fit orbital solution, the bisector span variations, and the relative S index. For both objects, we see no indication of correlated activity indicators.

We adopt the prescription described in Dumusque (2014), namely, the difference between the mean bisector velocity at 10-40% line depth and 60-90% line depth. To test against background blends or star spots, we computed the line bisector spans for all observations of Pr0201 and Pr0211. As illustrated in Figure 4.3, the bisector span variations are small ($\sigma_{BS} < 20\,\mathrm{m\,s^{-1}}$) and are not correlated with the observed RV variations. As an additional check against activity induced RV variations, for each spectrum of Pr0201 and Pr0211 we also compute the S index – an indicator of chromospheric activity in the CaII H&K lines. We follow the procedure of Vaughan et al. (1978), but we note that our S indices are not calibrated to their scale; these are relative measurements. As shown in Figure 4.3, there is no correlation with orbital phase. These line bisector and S index comparisons strongly

support the conclusion that the observed RV variations are caused by planetary companions.

4.1.4 Stellar and Planetary Properties

As described in Chapter 3, we used the spectroscopic classification technique Stellar Parameter Classification (SPC; Buchhave et al. 2012) to determine effective temperature $T_{\rm eff}$, surface gravity $\log g$, projected rotational velocity $v \sin i_\star$, and metallicity [m/H] for each of our target stars. From these classifications, we calculate a median cluster metallicity of [m/H] $= +0.187 \pm 0.038$ (Quinn et al. 2012), and we note that this value is consistent with, but more precise than, previous estimates (e.g., $+0.27 \pm 0.10$, Pace et al. 2008). Regarding the planet hosts Pr0201 and Pr0211 in particular, we note that our derived temperatures of 6174 K and 5326 K are in agreement with published spectral types (F7.5 and G9.3; Kraus & Hillenbrand 2007), and that their individual SPC-derived metallicities ($+0.18 \pm 0.08$ and $+0.19 \pm 0.08$) are consistent with the median of the cluster. Detailed heavy-element abundance analyses of Pr0201 can be found in Pace et al. (2008) and Maiorca et al. (2011).

We used the stellar parameters from SPC and the known age of Praesepe in conjunction with the Yonsei-Yale stellar models (Yi et al. 2001) to extract the stellar masses and radii. We found that the $\log g$ values indicated by the isochrone fits were slightly more than 1-σ lower than the SPC values, but it is possible that the formal errors for SPC are too small and/or that the stellar models are inaccurate for these somewhat young and active stars. We iterated the SPC analysis, this time fixing both the cluster metallicity and the $\log g$ from the isochrone fit. This resulted in a slightly lower $T_{\rm eff}$, and the subsqequent isochrone fit was consistent with all of the SPC parameters. Using an age of 578 Myr (Delorme et al.

2011), we adopted stellar masses and radii from the isochrone fits ($M_\star = 1.234 \pm 0.034\,M_\odot$, $R_\star = 1.167 \pm 0.121\,R_\odot$ for Pr0201; $M_\star = 0.952 \pm 0.040\,M_\odot$, $R_\star = 0.868 \pm 0.078\,R_\odot$ for Pr0211), but caution that the formal errors on stellar and planetary masses and radii do not encompass any potential systematics. The estimates of the stellar masses provide lower limits on the masses of the planets of $0.540 \pm 0.039\,M_{\rm Jup}$ for Pr0201b and $1.844 \pm 0.064\,M_{\rm Jup}$ for Pr0211b. Table 4.1 lists all of the stellar and planetary properties.

Table 4.1: Stellar and Planetary Properties

	Pr0201	Pr0211
P [days]	$4.43631^{+0.00044}_{-0.00036}$	$2.146117^{+0.000018}_{-0.000019}$
$T_{\rm c}$ [BJD]	2455992.877 ± 0.103	$2456458.217^{+0.013}_{-0.010}$
K [m s^{-1}]	$57.7^{+4.0}_{-4.6}$	$317.0^{+4.3}_{-3.8}$
$\sqrt{e}\cos\omega$	0.02 ± 0.18	$0.152^{+0.045}_{-0.066}$
$\sqrt{e}\sin\omega$	$0.28^{+0.11}_{-0.25}$	$-0.040^{+0.103}_{-0.053}$
e	0.079 ± 0.078	$0.025^{+0.016}_{-0.017}$
ω [deg]	87^{+52}_{-55}	-15^{+39}_{-21}
γ [km s^{-1}]	34.035 ± 0.101	35.184 ± 0.198
$M_\star$ [$M_\odot$]	1.234 ± 0.034	0.952 ± 0.040
$R_\star$ [$R_\odot$]	1.167 ± 0.121	0.868 ± 0.078
$T_{\rm eff,\star}$ [K][a]	6174 ± 50	5326 ± 50
$\log g_\star$ [dex][a]	4.41 ± 0.10	4.55 ± 0.10
$v \sin i_\star$ [km s^{-1}]	9.6 ± 0.5	4.8 ± 0.5
[m/H] [dex][a]	0.187 ± 0.038	0.187 ± 0.038
Age [Myr][b]	578 ± 49	578 ± 49
$M_p \sin i$ [$M_{\rm Jup}$]	$0.534^{+0.038}_{-0.043}$	$1.955^{+0.055}_{-0.067}$
$\sigma_\star$ [m s^{-1}]	21.6	23.1

Notes —

(a) From the final SPC iteration. [m/H] was fixed to the mean cluster metallicity calculated from an SPC analysis of our 53 stars. See Section 4.1.4.

(b) From Delorme et al. (2011).

4.1.5 Discussion

Our discovery of two hot Jupiters in Praesepe confirms that short-period planets do exist in open clusters. Moreover, assuming these gas giants formed beyond the snow-line, the planets have migrated to nearly circular short period orbits in 600 Myr. We can also immediately place some constraints on the hot Jupiter frequency in Praesepe. If we make the assumption

that the observations of the other stars in our sample can completely rule out the presence of short-period, massive planets, then we obtain a lower limit on the hot Jupiter frequency in Praesepe: $(2^{+2.6}_{-1.3})/53$; at least $3.8^{+5.0}_{-2.4}\%$ of all single FGK cluster members host a hot Jupiter (Poisson errors were calculated following the prescription in Gehrels 1986). While this number is slightly higher than the frequency for field stars ($1.20 \pm 0.38\%$; Wright et al. 2012), it is consistent with that expected from the enriched metallicity environment of Praesepe.

Finally, we note that uncertainties in planetary properties are most often limited by determination of properties of their host stars, but planets in clusters – particularly those that transit their host stars – can yield greatly reduced observational uncertainties. The observable transit parameter $a/R_\star$ constrains the stellar $\log g$ (Sozzetti et al. 2007), and the cluster's mean metallicity can be determined more precisely than that of any one star. Accurate $\log g$ and [m/H] values will also improve the spectroscopic $T_{\rm eff}$ estimates by breaking the degeneracy between the three parameters. When combined with the cluster age and distance, the resulting range of allowed masses and radii from stellar models would be greatly reduced. The precision in the stellar properties would propagate to an extremely precise planetary mass, radius, and age, providing a better test for models of planetary structure and evolution. Just as they have played an important role in the calibration of stellar properties, open clusters hold great promise as laboratories to explore properties of exoplanets at various ages and with great precision. *Transiting* giant planets in clusters would be of particular interest, as they would enable measurements of age, mass, and radius (and therefore bulk density); the *evolution* of such quantities may constrain planetary compositions, internal

structures, and formation.

With our discovery that hot Jupiters (tentatively) appear to be as common in clusters as in the field, we enthusiastically continue our survey in Praesepe (in search of longer period companions) and in additional nearby open clusters.

4.2 The Hyades Revisited

As we continue our search for hot Jupiters in open clusters, we remind the reader of the potential importance of such planets. More than 60 years after their proposed existence (Struve 1952) and nearly 20 years after the first detection (Mayor & Queloz 1995), we still lack a complete description of the hot Jupiter formation process. It is believed that they form beyond the snow line (located at $\sim$2.7 AU for the current-day Sun; e.g., Martin & Livio 2013) where there is a greater reservoir of solids with which to build a massive core (e.g., Kennedy & Kenyon 2008) before undergoing an inward migration process, but many questions remain to be answered.

While there are many mechanisms that could cause a gas giant planet to lose orbital angular momentum and migrate inward (see a discussion in Ford & Rasio 2008), two leading ideas are dynamical interactions with a circumstellar disk ("Type II" migration; Goldreich & Tremaine 1980; Lin & Papaloizou 1986) and multi-body gravitational interactions with other planetary companions ("planet-planet scattering"; e.g., Rasio & Ford 1996; Jurić & Tremaine 2008) or stellar companions (Kozai cycles; e.g., Fabrycky & Tremaine 2007). Migration through a disk must occur while the gas disk is present (within $\sim$10 Myr; Haisch et al.

2001) and is expected to preserve near-circular orbits, but if multi-body interactions are the source of most hot Jupiters, inward migration may take significantly longer and many of these planets should initially possess high eccentricity. For simplicity, we adopt the language of Socrates et al. (2012) and refer to these multi-body processes as "high eccentricity migration" (HEM). Given the different timescales predicted, one direct way to distinguish between mechanisms would be to search for hot Jupiters orbiting very young stars ($\lesssim 10\,\mathrm{Myr}$). However, the enhanced activity associated with young stars presents significant challenges for such surveys (e.g., Bailey et al. 2012). Alternatively, the dynamical imprint of HEM on the orbital eccentricity could provide a more accessible means to observationally constrain migration (e.g., Dawson & Murray-Clay 2013; Dong et al. 2014). Subsequent tidal circularization of the orbits erases this evidence of multi-body interaction over time, so identifying "dynamically young" systems, for which the system age (t_{age}) is less than the circularization timescale (τ_{cir}), is necessary for such an investigation. Longer period planets (large τ_{cir}) could satisfy this requirement, but hot Jupiters with periods of only a few days are both more common and easier to detect. Young planets (small t_{age}) offer another solution, but field stars tend to be old and their ages are difficult to estimate accurately (Mamajek & Hillenbrand 2008). The ages of open clusters, on the other hand—e.g., the 625 Myr Hyades (Perryman et al. 1998) or the 125 Myr Pleiades (Stauffer et al. 1998)—are typically precisely known and can be comparable to (or less than) the circularization timescales of many hot Jupiters. Consequently, planets in clusters could provide an avenue to directly measure this observational signature of HEM, allowing us to determine which process is most important

for hot Jupiter migration.

With the discovery of two hot Jupiters (described above and in Quinn et al. 2012) in the Praesepe (∼600 Myr), it is now clear that giant planets can form and migrate in a dense cluster environment. Moreover, two transiting mini-Neptunes discovered by Meibom et al. (2013) in NGC 6811 (∼1 Gyr, Meibom et al. 2011) using the *Kepler* spacecraft further suggest consistency between occurrence rates in open clusters and the field for planets of all sizes. But while open cluster planet surveys have recently enjoyed successes in measuring planet occurrence rates, they have not yet provided a convincing constraint for the hot Jupiter migration process, despite their potential to do so in the future. Unfortunately, the hot Jupiters discovered in Praesepe are too old to address timescale differences between migration mechanisms, and they are not dynamically young, either. That is, they are close enough to their stars to have already undergone tidal circularization ($t_{\rm age} > \tau_{\rm cir}$). To see the dynamical imprint of migration it will thus be necessary to identify younger hot Jupiters or hot Jupiters on wider orbits that would still bear the signature of dynamical scattering in order to help distinguish between migration mechanisms. In hopes of accomplishing the latter, we extend our RV survey to include a sample of Hyades stars, with ages and properties comparable to those in Praesepe.

4.2.1 Comparison to Previous Hyades Survey

As we have noted, Paulson et al. (2004b) report the results of their RV survey for planets in the Hyades, with no detected planets. This appears to be no fault of their own; their survey was comparable in most ways to ours. We typically have fewer observations per

star, but we were able to observe at higher cadence because of the flexible TRES queue schedule. They used a more sensitive instrument on a bigger telescope (Keck-HIRES; Vogt et al. 1994), but we were able to overcome much of the aperture difference because the stars are bright. Moreover, our RV precision is mainly limited by the intrinsic stellar jitter, not the instrumental precision or photon statistics. Our average measured velocity dispersion is $\sim$23 m s^{-1}, which is comparable to that of Paulson et al. (2004b), and is explainable by our slightly lower SNR and a different stellar sample that includes, e.g., stars with more rapid rotation. In summary, while the completeness of each survey will have to be taken into account separately, the two surveys should both be capable of finding planets, and we should be able to combine results for more robust statistics on planet occurrence in the Hyades.

4.2.2 Identification of Variability

As we did for Praesepe, we use a $P(\chi^2)$ threshold to identify candidate companions. In the Hyades, with a smaller target list that has been carefully cleaned of binaries using the results of the 30-year CfA binary survey, we find fewer variables. Only three stars meet the variability threshold, two of which have significant short-period power. The first of these, HD 26462, initially showed a clear RV variation ($\sim$1 km s^{-1}) on the timescale of a week or two that was suggestive of a planetary or brown dwarf companion, but subsequent observations revealed a larger variation and a strong correlation between the line broadening and the radial velocities. We concluded that two sets of spectral lines were present and that the true variation is much larger than a few km s^{-1}, but diluted by the blended set of lines. HD 26462 is most likely a hierarchical triple system composed of a single-lined binary and

a more distant stellar companion. The second star to meet our variability threshold was HD 285507, which also stood out obviously by eye as having significant RV variations after just 3 observations. We continued to observe this star and found significant short-period power in a Lomb-Scargle periodogram, consistent with the presence of a hot Jupiter. We discuss the system in more detail in the following sections.

4.2.3 Orbital Solution

We again used a Markov Chain Monte Carlo (MCMC) analysis to fit Keplerian orbits to the radial velocity data of HD 285507, fitting for orbital period P, time of inferior conjunction $T_{\rm c}$, the radial velocity semi-amplitude K, the center-of-mass velocity $\gamma_{\rm rel}$, and the orthogonal quantities $\sqrt{e}\cos\omega$ and $\sqrt{e}\sin\omega$, where e is eccentricity and ω is the argument of periastron. Because all marginalized MCMC posterior distributions were Gaussian in shape, we adopted errors corresponding to the extent of the central 68.3% interval of the distributions.

The RV errors did not require the addition of stellar jitter in order to obtain a good fit ($\chi^2_{\rm red} = 1$), so we set $\sigma_\star = 0$ in the orbital solution. We report the best fit orbital parameters in Table 4.2 and plot the best fit orbit in Figure 4.4.

Because a modest non-zero eccentricity causes only a small deviation from a circular orbit, we also investigated whether there exists correlated RV noise (e.g., due to surface activity and rotation) on timescales similar to the orbital period using the method of Winn et al. (2010b). Such noise could in principle cause small deviations from a circular orbit that might be interpreted as orbital eccentricity. To rule out this scenario, we fit a circular orbit and performed the test on the residuals to that solution. We found no evidence for

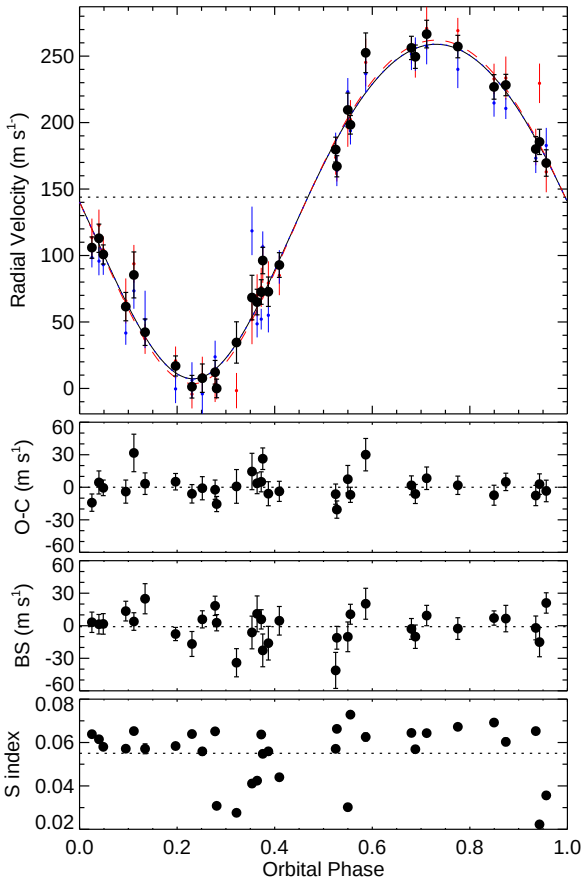

Figure 4.4 Orbital solution for HD 285507b. The panels, from top to bottom, show the relative RVs, best-fit residuals, bisector span variations, and relative S index values. In the top panel the large black points are the final RVs, but also plotted are the RVs derived from the blue and red orders of the spectrum, showing agreement at different wavelengths (see Section 4.2.4). RV error bars represent the internal errors, and do not include astrophysical or instrumental jitter, although 7.2 $\mathrm{m\,s^{-1}}$ instrumental jitter was added to the orbital fit. The solid black curve shows the best-fit orbital solution (and the blue and red dashed curves show the fits to the blue and red RVs). The blue curve is nearly indistinguishable from the black curve. The orbital parameters are listed in Table 4.2.

correlated noise on any timescale.

4.2.4 Tests for a False Positive

HD 285507 is slowly rotating ($P_{\rm rot} = 11.98$ days; Delorme et al. 2011), no X-ray emission was detected by ROSAT (Stern et al. 1995), and no stellar jitter term was required to obtain a good fit to the radial velocities, all of which are suggestive of a chromospherically inactive star. Nevertheless, to rule out false positive scenarios in which the observed RV variations are caused by stellar activity or stellar companions, we used our observations of HD 285507 to search for spectroscopic signatures that correlate with the orbital period.

If the RV variations were caused by a background blend (Mandushev et al. 2005) or star spots (Queloz et al. 2001), we would expect the shape of the star's line bisector to vary in phase with the radial velocities. A standard prescription for characterizing the shape of a line bisector is to measure the relative velocity at its top and bottom; this difference is referred to as a line bisector span (see, e.g., Torres et al. 2005). To test against background blends or star spots, we computed the line bisector spans for all observations of HD 285507. As illustrated in Figure 4.4, the bisector span variations are small ($\sigma_{\rm BS} = 15\,{\rm m\,s^{-1}}$) and they are not correlated with the observed RV variations, having a Pearson r value of only 0.06.

For each spectrum we also computed the S index – an indicator of chromospheric activity in the Ca II H&K lines. We follow the procedure of Vaughan et al. (1978), but we note that our S indices are not calibrated to their scale; these are relative measurements. Correlation between S index and orbital phase might be expected if the apparent RV variations were activity-induced, but as shown in Figure 4.4, there is no such correlation (Pearson $r = 0.17$). Instead, there may be significant periodicity in the S indices at 12 or 13 days (Fig. 4.5),

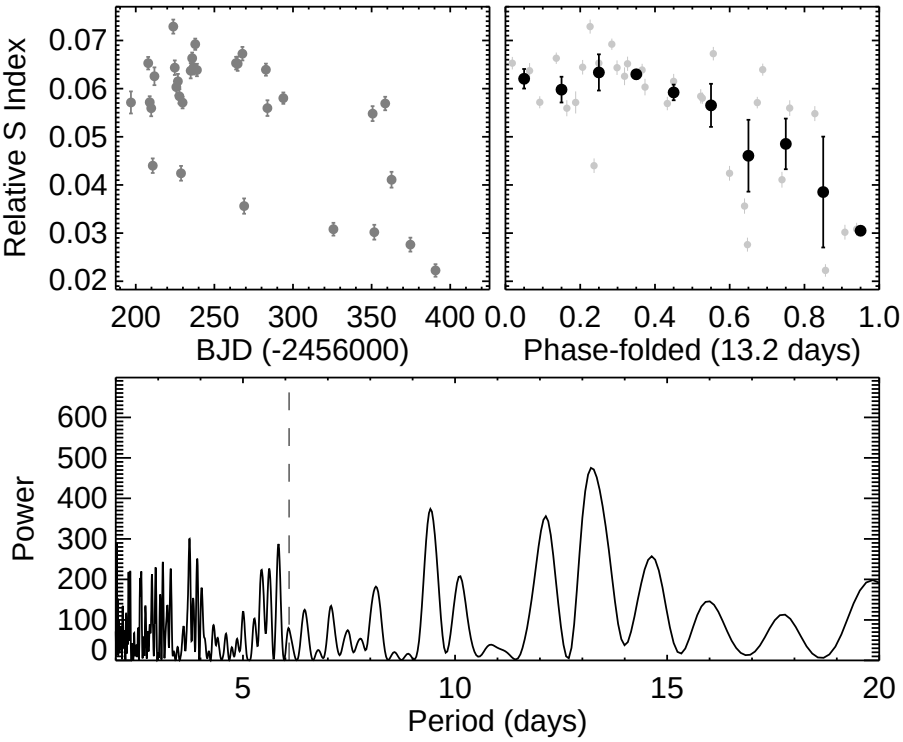

Figure 4.5 *Top left*: the stellar activity, as characterized by the relative S index measured from our spectra of HD 285507. *Bottom*: the Lomb-Scargle periodogram indicates that there may be significant periodicity on timescales similar to the stellar rotation period of 11.98 days (Delorme et al. 2011), but not at the RV period of 6.09 days (dashed line). *Top right*: the data have been folded onto the highest peak, 13.2 days, and binned for illustration.

which is similar to the published rotation period of 11.98 days. Our data set is too sparse to claim a detection of the rotation period from the activity measurement, but we can see there is no power at the observed orbital period of 6.088 days.

Finally, if spots were the source of the variation, we might also expect the RV amplitude to be wavelength dependent because contrast between the spot and the stellar photosphere is wavelength dependent. We derived RVs for the blue and red orders separately (weighted mean wavelengths of $\lambda_{\rm blue} = 4967\,\text{Å}$ and $\lambda_{\rm red} = 5845\,\text{Å}$), and find the amplitudes to be consistent at the level of 0.5σ ($3\,\mathrm{m\,s^{-1}}$, Fig. 4.4). This agreement between the red and

blue amplitudes is encouraging, but is not conclusive by itself. We generally expect large amplitude differences between the optical and infrared for spot-induced RVs because the spot contrast can change drastically over that wavelength range. The expected amplitude difference for our smaller ($\sim$1000 Å) wavelength span, on the other hand, is more uncertain because the local wavelength dependence of the RV amplitudes is itself dependent upon the (unknown) temperature difference between spot and photosphere (e.g., Reiners et al. 2010; Barnes et al. 2011a). The simulations of Reiners et al. (2010) indicate that the amplitude difference might be detectable if the spot contrast is low, but not if it is high. Even this is not certain, though, as other authors (Desort et al. 2007) predict a 10% drop in amplitude between blue and red for high contrast spots on solar-type stars. Regardless, from these results and the work of Saar & Donahue (1997), we estimate that to induce the observed RV amplitude ($125\,\mathrm{m\,s^{-1}}$) given $v \sin i_\star \approx 3.2\,\mathrm{km\,s^{-1}}$, the spot would have to cover $\sim$20% of the visible stellar surface for low contrast spots ($\Delta_{T_{\rm eff}} \approx 200\,\mathrm{K}$) or $\sim$5% for high contrast spots ($\Delta_{T_{\rm eff}} \approx 1500\,\mathrm{K}$). Large and high contrast spots are more likely to appear on very magnetically active stars (e.g., Bouvier et al. 1995), and we have no evidence for strong magnetic activity. Furthermore, for such spot configurations, the RV-bisector correlation should be strong (e.g., Mahmud et al. 2011), and we observe no correlation.

We conclude from the evidence presented above that the observed RV variation is not caused by spots, but is the result of an orbiting planetary companion.

4.2.5 Stellar and Planetary Properties

We once again used SPC to determine $T_{\rm eff}$, $\log g$, $v \sin i_\star$, and [m/H] for HD 285507. As previously noted, the analysis may be limited by degeneracy between the atmospheric parameters, and in this case we can enforce the known cluster metallicity ($+0.13 \pm 0.01$, Paulson et al. 2003) to partially break that degeneracy. We utilized the Dartmouth (Dotter et al. 2008), Yonsei-Yale (Yi et al. 2001), and Padova (Girardi et al. 2000) stellar models to determine the physical stellar parameters. Applying an observational constraint on the size of the star – imposed indirectly by the spectroscopic $T_{\rm eff}$, V magnitude ($V = 10.473 \pm 0.012$, Röser et al. 2011), and distance (41.34 ± 3.61 pc, van Leeuwen 2007) – and enforcing the age (625 Myr, Perryman et al. 1998) and metallicity of the Hyades, we determined the best fit mass and radius for each of the three isochrones. All three results agreed to within 3% in mass and 5% in radius, and although the resulting $\log g$ values indicated by the isochrones were consistent with the spectroscopically determined value, the temperatures were nominally discrepant at the 2σ level. It is possible that, for stars of this mass and age, the stellar models and/or SPC suffer from a systematic bias not reflected in the formal errors. Given that the exact stellar parameters have little bearing on the results presented here, we choose to simply caution the reader and inflate the errors on stellar mass and radius by a factor of two. We adopted the mean mass and radius from the three isochrone fits ($M_\star = 0.734 \pm 0.034\,M_\odot$, $R_\star = 0.656 \pm 0.054\,R_\odot$), where the uncertainties listed here are the inflated statistical errors. Table 4.2 lists all of the stellar and planetary properties. We note that our adopted temperature (4503 K) is consistent with previous estimates of the spectral type (e.g., K5,

Nesterov et al. 1995), and using the spectral type/temperature relations assembled in Kraus & Hillenbrand (2007), we estimate a more precise spectral type of HD 285507 to be K4.5.

Table 4.2: Stellar and Planetary Properties

Orbital Parameters	
P [days]	6.0881 ± 0.0018
T_c [BJD]	2456263.121 ± 0.029
K [m s^{-1}]	125.8 ± 2.3
e[a]	0.086 ± 0.019
ω [deg][a]	182 ± 11
γ_{rel} [m s^{-1}]	143.9 ± 1.6
γ_{abs} [km s^{-1}][b]	38.149 ± 0.023
Stellar Parameters	
$M_\star$ [$M_\odot$][c]	0.734 ± 0.034
$R_\star$ [$R_\odot$][c]	0.656 ± 0.054
$T_{eff,\star}$ [K][c]	4503^{+85}_{-61}
$\log g_\star$ [dex][c]	$4.670^{+0.051}_{-0.058}$
$v \sin i_\star$ [km s^{-1}]	3.2 ± 0.5
[m/H] [dex][c]	+0.13 ± 0.01
Age [Myr][c]	625 ± 50
$M_P \sin i$ [M_{Jup}]	0.917 ± 0.033
$\sigma_\star$ [m s^{-1}]	8.0

Notes —

(a) The MCMC jump parameters included the orthogonal quantities $\sqrt{e}cos\omega$ and $\sqrt{e}sin\omega$, but we report the more familiar orbital elements e and ω.

(b) The absolute center-of-mass velocity has been shifted to the RV scale of Nidever et al. (2002), on which the velocities of HD 3765 and HD 38230 are -63.202 km s^{-1} and -29.177 km s^{-1}, respectively.

(c) From the final SPC analysis and isochrone fits (§ 4.2.5). [m/H] and age were fixed to values determined for the cluster (Paulson et al. 2003; Perryman et al. 1998).

4.2.6 Stellar Inclination and a Search for Transits

Since the rotation period of HD 285507 is 11.98 days and we have estimates for $R_\star$ and $v \sin i_\star$, we can in principle calculate the inclination of the stellar spin axis. In practice, the fractional uncertainty on $v \sin i_\star$ is large (not because the absolute uncertainty is large, but because the value is small), and the inclination can only be constrained to be $i > 72°$. This does not exclude an edge-on stellar equator ($i = 90°$), and because hot Jupiters orbiting cool

stars ($\lesssim 6250\,\mathrm{K}$) tend to be well-aligned with the stellar spin axis (see, e.g., Albrecht et al. 2012b), an inclination of $\sim 90^\circ$ would make a transit more likely *a priori*. However, even an inclined stellar spin axis would not preclude transits of HD 285507, as there is evidence to suggest that young planets tend to be more misaligned than old planets (e.g., Triaud 2011). In addition to providing a radius measurement for HD 285507b, transits of this relatively young planet orbiting a cool star could be valuable to the interpretation of these intriguing correlations.

With this in mind, we conducted photometric monitoring of HD 285507 with KeplerCam on the FLWO 1.2-m telescope at the predicted time of inferior conjunction on UT 07-Nov-2012. KeplerCam is a monolithic, 4k×4k Fairchild 486 chip with a $23' \times 23'$ FOV and a resolution of $0.''336\,\mathrm{pixel}^{-1}$. We used a Sloan i filter with exposure times of 45 seconds and readout time of 12 seconds, obtaining a total of 334 images over 5.5 hours. We reduced the raw images using the IRAF package `mscred`, and performed aperture photometry with SExtractor (Bertin & Arnouts 1996).

The resulting light curve showed no sign of a transit, but to determine our detection sensitivity, we simulated transits – using the routines of Mandel & Agol (2002) and a quadratic limb darkening law from Claret et al. (2012) – and injected them into our observed data. For each injected transit, we compared the mean flux in transit (for all points between mid-ingress and mid-egress) to the mean flux out of transit. If the two differed by more than 1-σ, we classified that transit as detected. From this, we can rule out a central transit of objects larger than 0.35 R_{Jup} (see Figure 4.6). If HD 285507b were to transit, then the de-

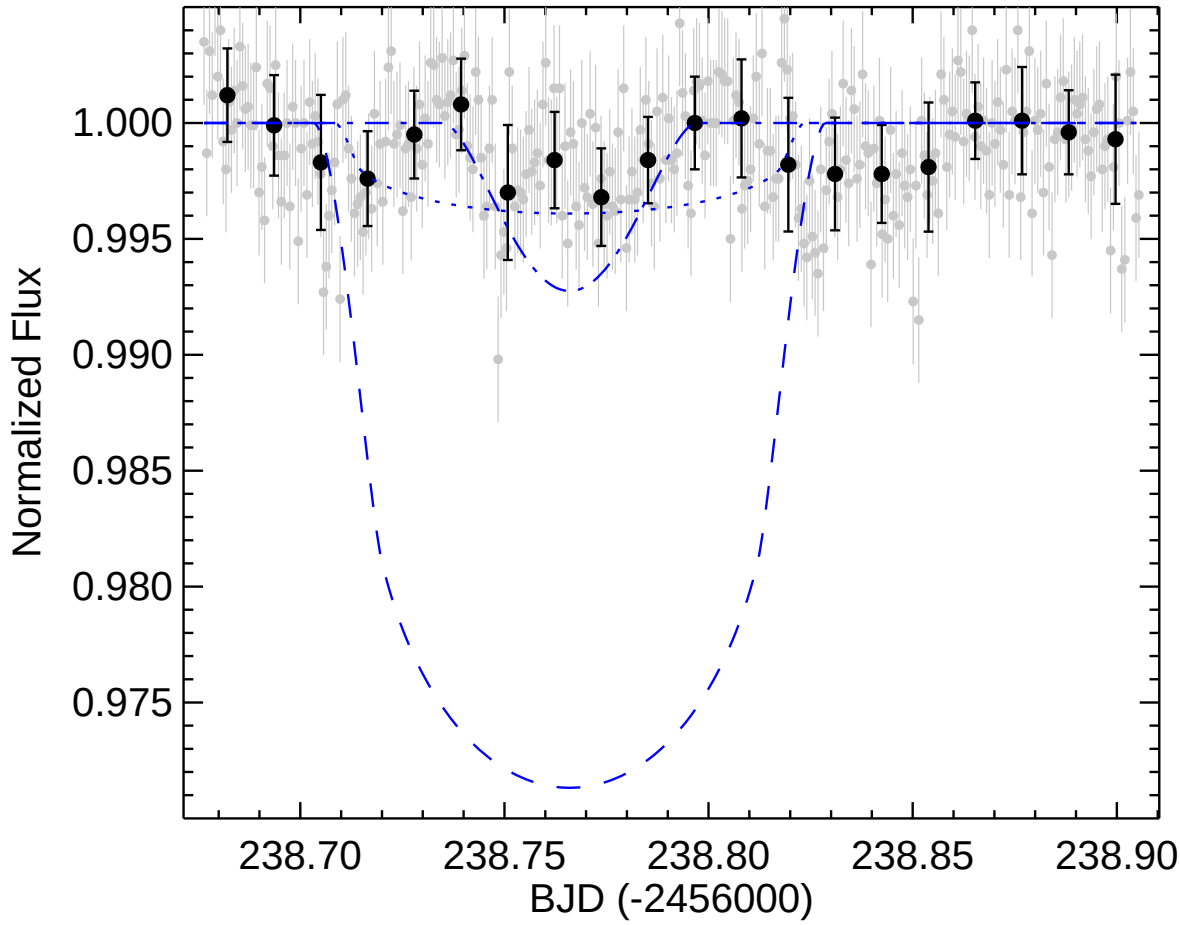

Figure 4.6 The light curve of HD 285507, showing the individual data (small grey circles), the binned data (large black circles), and three simulated transit models at the predicted time of transit (all of which are rejected as bad fits to the data): a central transit of a $0.95\,R_{\rm Jup}$ planet (dashed line), a central transit of a $0.35\,R_{\rm Jup}$ planet (dotted line), and a grazing transit ($b = 1$) of a $0.95\,R_{\rm Jup}$ planet (dash-dotted line). The latter two cases mark simulated detection limits for the observed data quality (see Section 4.2.6). The uncertainty in the time of inferior conjunction at this epoch is only about 1 hour ($\sim$0.04 days).

rived minimum mass would be the true planetary mass. Under this assumption and using the mass-radius-flux relation from Weiss et al. (2013), we would then expect its radius to be $\sim$0.95 $R_{\rm Jup}$, much larger than our sensitivity limit. We can also rule out all transits of

a 0.95 $R_{\rm Jup}$ planet with impact parameters $b < 1$ (i.e., all but the most extreme grazing transits). Using the final ephemeris, the transit center should have occurred 2.22 hours after our observations began ($T_{\rm c}$ = 2456238.7686 BJD), with an uncertainty of $\sim$1 hour, so it is unlikely that a transit occurred outside our observing window.

4.3 Hot Jupiter Occurrence in Clusters

Our discovery of a hot Jupiter in the Hyades bolsters the statistics of short period giant planets in open clusters (of which three are now known). These discoveries, along with a careful treatment of survey completeness and the properties of the stellar sample, can now be used to refine the calculation of the frequency of hot Jupiters in clusters.

4.3.1 Metal-Rich Clusters

Together, members of the Hyades and Praesepe open clusters constitute a large sample of metal-rich stars. Because of the enhanced hot Jupiter fraction for metal-rich field stars, it is possible that the architectures of metal-rich planetary systems are significantly different from those of metal-poor systems, and these differences may significantly influence the efficiency of migration in open clusters, where close stellar encounters are expected to be more frequent. For example, simulations by Shara et al. (2016) suggest that close stellar fly-bys in clusters may result in an increase in perturbations to planetary orbits, which lead to a higher incidence of planet-planet scattering events. In such a scenario, the hot Jupiter frequency may be affected, particularly if planet-planet scattering is an important contributor to hot Jupiter migration. As such, we separately examine the hot Jupiter occurrence rate in metal-rich

clusters before calculating the occurrence rate for our entire open cluster sample.

Including the Paulson et al. (2004b) null result in the Hyades (0 planets among 74 FGK stars), our Hyades sample (1 in 25; Quinn et al. 2014), and our Praesepe sample (2 in 53; Quinn et al. 2012), a total of 3 out of 154 stars host a hot Jupiter. To be able to make a better comparison to field star surveys, we have excluded from these totals stars with RV variations that appear to indicate the presence of a close stellar companion that would be expected to prevent the formation or survival of planets.

While the raw planet counts can provide an estimate of the occurrence rates, survey completeness must be considered in order to make an accurate calculation. To assess the sensitivity of our survey (and that of Paulson et al. 2004b), we simulate planetary orbits and sample them according to the actual observing cadences and measurement errors for each star. Because we cannot know, *a priori*, the planetary mass and orbital period distributions in open clusters, we draw these quantities from a smoothed empirical distribution of hot Jupiters orbiting field stars with periods less than 10 days and masses less than $13\,M_{\rm Jup}$. While we do expect that environmental factors will create some differences between cluster and field star distributions, we do not expect them to be so different that drawing from the incorrect distribution will significantly impact our calculation of completeness. We also note that a characterization of the joint distribution of giant planet masses and periods can be found in the literature (e.g., Cumming et al. 2008), but we do not use this distribution because it does not account for the shape of the distribution in small ranges of period (such as in the local short-period peak corresponding the hot Jupiters). Each orbit is given a random

time of inferior conjunction and an orbital inclination drawn from an isotropic distribution (i.e., $prob(i) \propto \sin i_\star$). We assume circular orbits for periods less than 7 days, and for longer periods, we draw eccentricities following a Rayleigh distribution with Rayleigh parameter $\sigma = 0.3$ (a good match to the eccentricities of giant planets according to Jurić & Tremaine 2008), with randomly oriented longitudes of periastron.

For each synthetic RV data set, we ask whether we would have detected the planet according to our $P(\chi^2)$ threshold. If the simulated planet meets this criterion, we call it a detectable planet, because in our actual survey we would have followed it up and detected it. We happily point out that adopting a clear, quantitative criterion for follow-up, as we have done in our survey, makes completeness calculations straightforward. For the Paulson Hyades survey, we make the assumption that they, too, would have detected planets with $P(\chi^2) < 0.001$, even though they did not adopt this exact criterion in their survey. We argue that this is a valid assumption because they did follow up their low-amplitude variables, and none of the remaining stars in their survey exhibits $P(\chi^2) < 0.001$.

After correcting for completeness and calculating Poisson errors following the prescription in Gehrels (1986), we find a hot Jupiter frequency of $1.97^{+1.92}_{-1.07}\%$ in the metal-rich Praesepe and Hyades open clusters. However, giant planet occurrence scales with metallicity approximately as $10^{2[\mathrm{Fe/H}]}$ (Fischer & Valenti 2005). If we take [Fe/H] $\approx +0.15$ as representative of the combined Praesepe and Hyades sample, the solar-metallicity-adjusted hot Jupiter frequency in clusters is $0.99^{+0.96}_{-0.54}\%$. Although more discoveries are needed to reduce the uncertainty, this is in good agreement with the frequency for field stars ($1.20 \pm 0.38\%$; Wright

et al. 2012), and improves the evidence that planet frequency is the same in clusters and the field.

4.3.2 600 Myr Clusters

While it is important to bear in mind the effect that stellar environment may have on the formation and evolution of planetary systems, it can also be illustrative to examine the characteristics of a larger, more diverse population. Here, we treat our entire sample of adolescent (500-625 Myr) clusters (once again including the null result from Paulson et al. 2004b) as one population and calculate the hot Jupiter occurrence rate. In Coma Berenices and Ursa Major, we detect no hot Jupiters among 31 and 16 non-binary Sun-like members, respectively. This brings our total sample to 201 stars, of which 3 host a hot Jupiter. We again adjust for the metallicity of the stellar samples and for the survey completeness. The final derived solar-metallicity-equivalent hot Jupiter occurrence rate in these adolescent clusters is $0.93^{+0.90}_{-0.50}\%$.

CHAPTER 5
EVIDENCE FOR HIGH ECCENTRICITY MIGRATION

5.1 HD 285507b: a case study in migration

The discovery of a hot Jupiter in the Hyades open cluster brings the total number of short period giant planets in clusters to 3. Of these, however, HD 285507b is unique in that it is the only one that is definitively eccentric; the 2 planets in Praesepe are consistent with having circular orbits. As described in the introduction, the non-zero eccentricity of HD 285507b could be a tracer of its migration history if the planet is dynamically young (i.e., $\tau_{\rm cir} > t_{\rm age} = 625$ Myr). If it is dynamically old, then the orbit should have already circularized, and establishing a credible link between the eccentricity and the migration process becomes more difficult. In planet-planet scattering, for example, if the outer planet gets ejected during the scattering event as is expected, then one must invoke a separate mechanism to excite eccentricity again after circularization. To put it differently, if HD 285507b is dynamically young, then planet-planet scattering is sufficient (but not necessary) to explain the observations; if the planet is dynamically old, planet-planet scattering is neither sufficient nor necessary. To test these scenarios, we estimate $\tau_{\rm cir}$ using the equation given by Adams & Laughlin (2006):

$$\tau_{\rm cir} = 1.6 \text{ Gyr} \times \left(\frac{Q_{\rm P}}{10^6}\right) \times \left(\frac{M_{\rm P}}{M_{\rm Jup}}\right) \times \left(\frac{M_*}{M_\odot}\right)^{-1.5} \times \left(\frac{R_{\rm P}}{R_{\rm Jup}}\right)^{-5} \times \left(\frac{a}{0.05 \text{ AU}}\right)^{6.5}$$

where $Q_{\rm P}$ is the planetary tidal quality factor (a measure of the efficiency of tidal dissipation

within the planet). Note that $\tau_{\rm cir}$ scales linearly with $Q_{\rm P}$, which is unknown to within an order of magnitude. The Jupiter-Io interaction does provide the constraint $6\times10^4 < Q_{\rm Jup} < 2\times10^6$ (Yoder & Peale 1981), but $Q_{\rm P}$ is likely dependent upon temperature, composition, rotation, and internal structure, all of which may be quite different for hot Jupiters. $Q_{\rm P} \approx 10^6$, which we adopt herein, is a fiducial value often assumed for short period giant planets (for a more detailed discussion of tidal dissipation, see, e.g., Ogilvie & Lin 2004).

Since HD 285507b does not transit, we do not know $R_{\rm P}$ and measure only a minimum mass, $M_{\rm P} \sin i$. However, we can calculate the expectation value of $\sin i$ for randomly oriented orbits to determine the most likely mass, and then use the giant planet mass-radius-flux relation derived by Weiss et al. (2013) to estimate the planetary radius:

$$\frac{R_{\rm P}}{R_\oplus} = 2.45 \left(\frac{M_{\rm P}}{M_\oplus}\right)^{-0.039} \left(\frac{F}{\rm erg\ s^{-1}\ cm^{-2}}\right)^{0.094} \tag{5.1}$$

where F is the time-averaged incident flux on the planet. Since $R_{\rm P}$ depends only weakly on $M_{\rm P}$, assuming an inclination is not likely to introduce a large radius error – there is only a 1% difference in derived radius between edge-on and average-inclination orientations.

Under these assumptions, we find $\tau_{\rm cir} \approx 11.8$ Gyr – much larger than the age of the cluster. Note that this holds true even for the full range of $Q_{\rm Jup}$ (corresponding to 700 Myr $< \tau_{\rm cir} <$ 22.6 Gyr). We conclude that HD 285507b is dynamically young. While it is tempting to thus proclaim that migration has occurred via a HEM mechanism, recall that this is not a necessary condition for a dynamically young planet with an eccentric orbit. For any individual planet, non-zero eccentricity could also be the result of continued interaction with

an undetected planetary or stellar companion, a recent close stellar encounter, or even modest eccentricity excitation via Type II migration (e.g., D'Angelo et al. 2006). Only analysis of a population of planets can provide meaningful insight into the migration process in this manner. Therefore, we turn to the literature for ages and circularization timescales of the known sample of hot Jupiters.

5.2 Dynamically Young HJs are Preferentially Eccentric

5.2.1 Description of the Analysis

To search for dynamical imprints of migration among known hot Jupiters ($M_{\rm P} > 0.3\ M_{\rm Jup}$, $P < 10$ days), we follow the prescription described above to calculate $\tau_{\rm cir}$ (and $M_{\rm P}$ and $R_{\rm P}$ for non-transiting planets). We adopt ages, eccentricities, planetary masses and radii, and stellar masses, radii, and temperatures from the literature.[1] In Figure 5.1, we plot $t_{\rm age}$ versus $\tau_{\rm cir}$ for this sample. While the figure is complicated by the uncertainties already discussed as well as poorly constrained ages and potential biases in measuring modest eccentricities (e.g., Shen & Turner 2008; Pont et al. 2011; Zakamska et al. 2011; Wang & Ford 2011), there is a hint that the points to the right of the circularization boundary are preferentially eccentric and the ones to the left are preferentially circular. If HEM were responsible for the final stages of hot Jupiter migration, this would be expected; planets get scattered inward on highly eccentric orbits and circularize over time. If Type II migration were responsible, we should expect very little difference between the eccentricity distributions to the right and left of the

[1] All values were obtained from The Extrasolar Planets Encyclopaedia, www.exoplanet.eu. Only planets with ages listed on exoplanet.eu are included in this analysis.

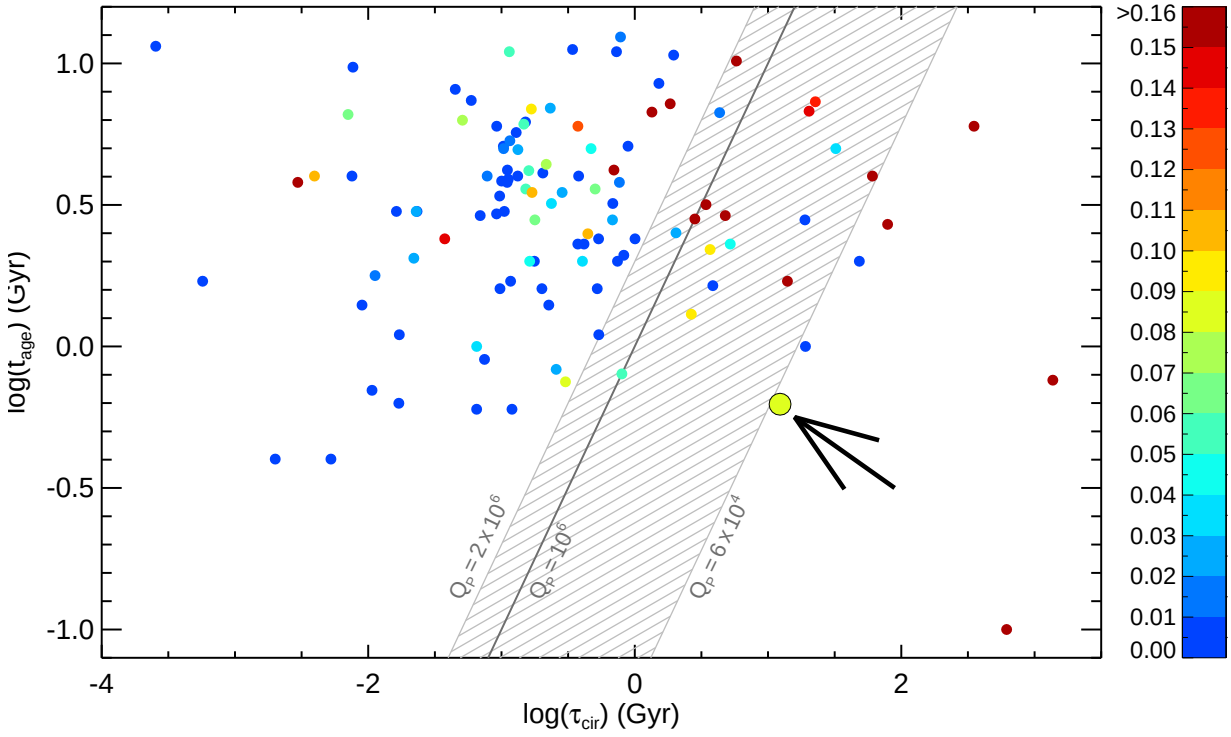

Figure 5.1 Age versus circularization timescale for short period ($P < 10$ days) massive ($M > 0.3\ M_{\rm Jup}$) planets, assuming a tidal quality factor $Q_{\rm P} = 10^6$ for all planets. The solid dark line indicates where $t_{\rm age} = \tau_{\rm cir}$; planets to the left of the line are expected to have undergone tidal circularization. We also plot a shaded region to show the estimated uncertainty in this boundary given the range of $Q_{\rm P}$ values consistent with observations of the Jupiter-Io interaction (see Yoder & Peale 1981). The data points are colored according to their eccentricity, and HD 285507b is the large outlined circle indicated by the arrow. There is a hint that the right side is populated by preferentially eccentric (red) planets and the left side by preferentially circular (blue) planets. This is explored further in Figure 5.2.

boundary; ordered migration through a gas disk should largely preserve circular orbits, so subsequent tidal interactions would not change the population significantly. In Figure 5.2, we plot the eccentricity histograms and cumulative distributions for the two populations, which contain 92 and 22 planets (as shown in Fig. 5.1). To quantify the difference between them, we ran a Kolmogorov-Smirnov (KS) test. The KS p-value is the likelihood that the

two subsamples came from the same parent distribution, and in this case, p = 3.3×10^{-5}. We conclude that the two distributions do not come from the same parent distribution, with ∼99.997% confidence, and infer that high eccentricity migration mechanisms play a significant role in hot Jupiter migration. We also ran an Anderson-Darling (AD) test, which is similar to a KS test, but is more sensitive to differences in the distribution tails. The AD test indicates an even greater significance that the two distributions do not come from the same parent distribution of eccentricities.

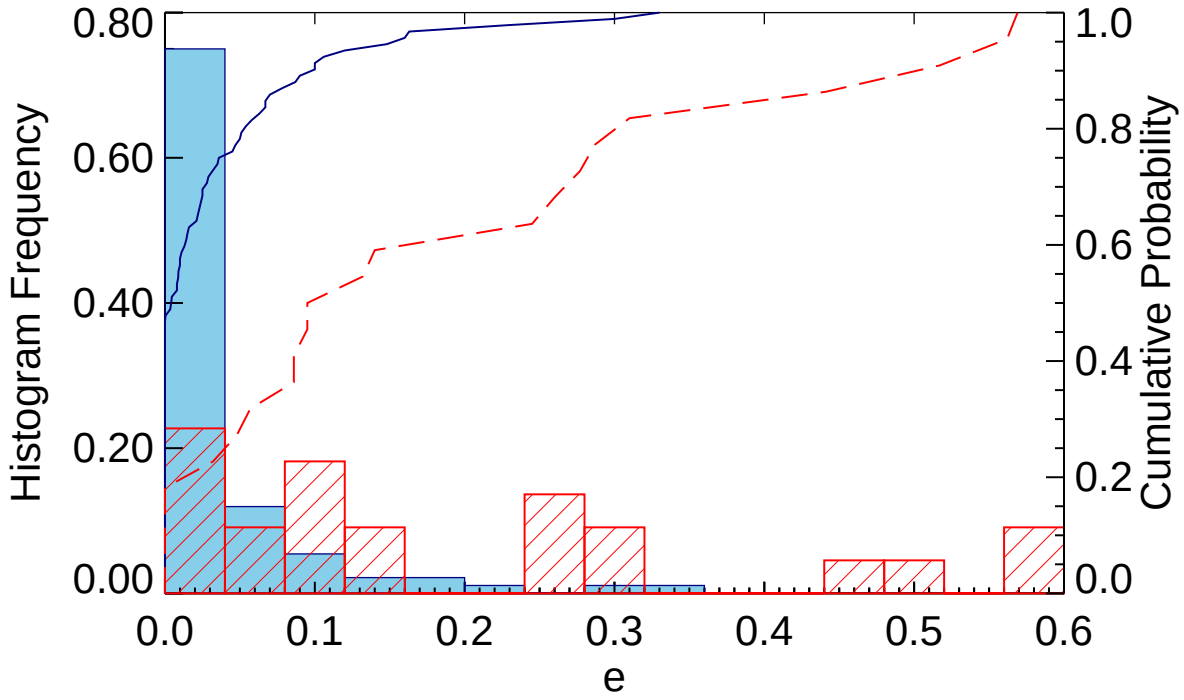

Figure 5.2 Eccentricity histograms and cumulative distributions of hot Jupiters that have (filled and solid blue; left of the thick solid line in Fig. 5.1) and have not (striped and dashed red; right of the line) been tidally circularized. As in Figure 5.1, we have assumed $Q_P = 10^6$ for all planets. A KS test rejects the hypothesis that the two subsamples are drawn from the same distribution with 99.997% confidence.

5.2.2 The Effect of Measurement Errors

As noted previously, ages and eccentricities can be difficult to determine for many of these systems, so it is important to consider what effect uncertainties may have on the significance of our result. Ages of field stars can be estimated by many techniques, including gyrochronology, stellar activity, lithium abundance, and isochrone fitting. However, ages derived from multiple techniques do not always agree, and when they do agree, the allowed range of ages can still be quite large. Likely for this reason, the Extrasolar Planets Encylcopaedia does not report uncertainties on the age (when age is reported at all). Mamajek & Hillenbrand (2008) claim a precision of $\sim$0.2 dex in their activity-age relation, and while not all stars in this sample have ages derived in this manner, we believe this to be an appropriate approximate error for isochrone fitting as well, which is one of the more widespread techniques employed to determine ages. We therefore adopt this as a typical error in our analysis.

Eccentricity errors are similarly heterogeneously reported in the literature, especially for nearly circular orbits. Some authors assume zero eccentricity in such cases for simplicity, which introduces a bias toward smaller values, while others report upper limits or a measured eccentricity. When a small measured value is reported, it may be biased toward larger eccentricities depending on the details of the fitting. Rather than worry about potential conflicting biases in a heterogeneous set of eccentricities and associated errors, we assume a constant eccentricity error of 0.05 for all planets in our sample. We also assume errors of 10% on stellar and planetary masses and radii, 3% on semi-major axis, and 100 K on stellar effective temperature. These values are minor contributors to uncertainty in the analysis,

but they do have a small effect on the derived circularization timescales.

Using the above errors, we redraw our sample 10^4 times. For each of these simulated data sets, we run a KS test to determine the significance of the difference in populations, resulting in a distribution of 10^4 p-values. The median of this distribution is 2.7×10^{-4}, or a 99.973% confidence (nearly 4-σ) that the two samples come from different parent distributions. Furthermore, we find that even for eccentricity errors as large as 0.1 (which is unrealistically large for nearly all planets in the sample), the KS significance remains greater than 3-σ. From this, we conclude that even with conservatively large errors, our result holds: dynamically young planets have larger eccentricities, which suggests HEM mechanisms contribute significantly to hot Jupiter migration.

5.3 A constraint on the tidal quality factor for hot Jupiters, $Q_{\rm P}$

Until now we have been assuming $Q_{\rm P} = 10^6$ to determine which planets are dynamically young (right side of the circularization boundary in Fig. 5.1) and which are dynamically old (left side), allowing us to draw conclusions about the migration process. If we instead *start* with the assumption that planets migrate inward in possession of some intial eccentricity (rather than being gently shepherded on circular orbits through the gas disk), we can invert the problem to place a constraint on the tidal quality factor $Q_{\rm P}$. As we vary $Q_{\rm P}$, the circularization boundary changes location, and the difference between the two populations should be maximized (and the KS p-value minimized) for the correct (average) hot Jupiter $Q_{\rm P}$. Note that it does not matter what fraction of hot Jupiters has undergone HEM – if any

fraction has, then the minimum p-value should occur when the circularization boundary is in the correct place.

Figure 5.3 shows the results of this experiment. A value on the order of 10^6 is preferred, which seems to rule out much of the parameter space consistent with Jupiter's tidal quality factor (and validates our assumption of $Q_{\rm P} = 10^6$). The discrete data points do not produce a smooth distribution, so finding the minimum is not straightforward. As such, we smooth it using a moving average with a boxcar filter of size $[\frac{2}{3}Q_{\rm P}, \frac{3}{2}Q_{\rm P}]$. Quantitative confidence limits on the minimum are difficult to assess (the vertical axis is *not* a probability associated directly with $Q_{\rm P}$), but we take approximate upper and lower limits on $Q_{\rm P}$ to be those for which the smoothed p-value is 10 times its smoothed minimum value, which occurs for $Q_{\rm P} = 1.28 \times 10^6$. For each simulated data set described in Section 8.4, we calculate $Q_{\rm P}$ this way and find the median to be similar (1.12×10^6), but with smaller errors. This is not surprising, as the statistical errors from the simulations are akin to a standard deviation of the mean whereas the errors derived from a single p-value versus $Q_{\rm P}$ experiment are akin to a sample standard deviation. To describe the population, we therefore adopt the latter and suggest an appropriate tidal quality factor for a typical hot Jupiter is $\log Q_{\rm P} = 6.11^{+0.52}_{-0.23}$ (see Fig. 5.3 for a visual representation).

5.3.1 Discussion

A primary motivation for the search for young planets is that their ages are comparable to the timescale of migration. Thus, the orbital properties of such planets may still bear the dynamical signature of this process. Since different migration mechanisms are predicted to

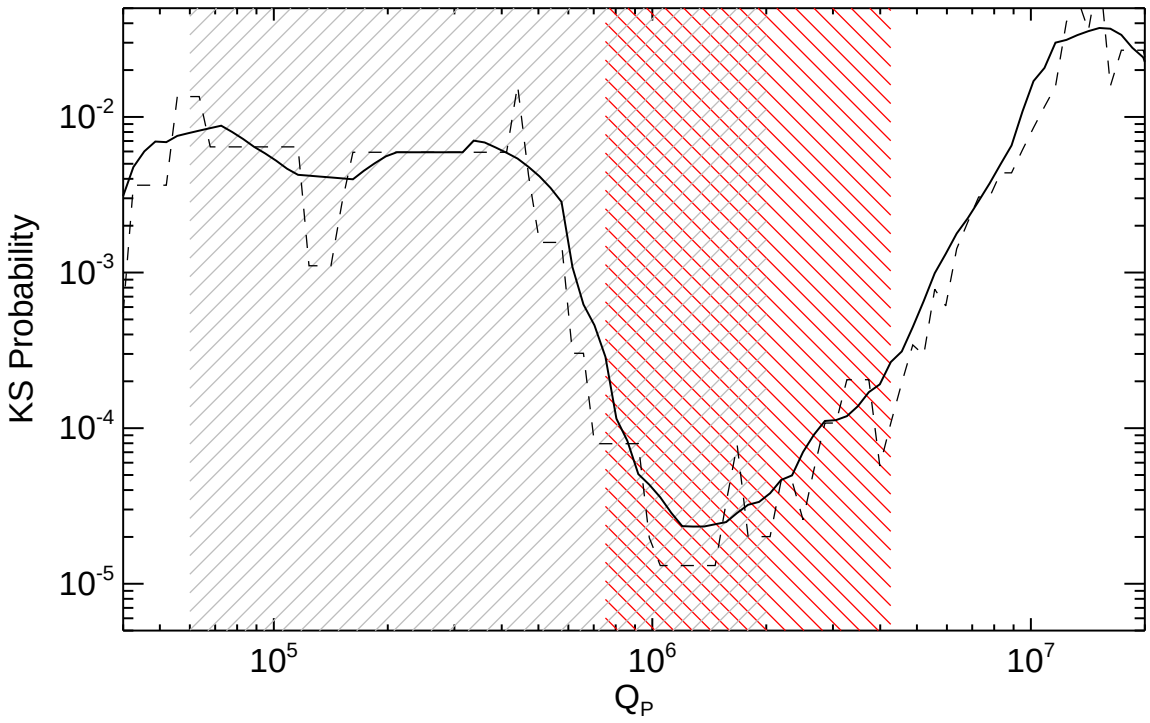

Figure 5.3 KS p-values from comparisons of the eccentricity distributions of hot Jupiter systems with $t_{\rm age} < \tau_{\rm cir}$ to those with $t_{\rm age} > \tau_{\rm cir}$, as a function of the assumed $Q_{\rm P}$ (dashed line); the solid line shows the same result after a boxcar filtering. Since the minimum p-value should occur for the most realistic $Q_{\rm P}$ (see Section 5.3), we can constrain $Q_{\rm P}$ for a typical hot Jupiter to be between about 7.5×10^5 and 4.3×10^6 (red, right hatched region encompassing the broad minimum). The Jupiter-Io constraint (gray, left hatched region) only overlaps partially with the position of the minimum at $Q_{\rm P} = 1.28 \times 10^6$, and given the expectation that Q will be larger for hot Jupiters, we do not apply this constraint to our adopted range for $Q_{\rm P}$.

produce hot Jupiters on different timescales and with different orbital eccentricities, we can use the properties of young hot Jupiters (and their existence at various ages) to determine the process by which they migrate. The ages of the cluster planets discovered thus far do not place a strong direct constraint on the *timescale* of migration (we know only that the process took less than 600 Myr), but the newly discovered planet in the Hyades holds a clue

to its dynamical history. HD 285507b has a long circularization timescale, so its non-zero eccentricity may be a remnant of the migration process, which would suggest planet-planet scattering or Kozai cycles have played a role in its orbital evolution. There is no observational evidence for a third body, but one cannot be excluded either. The RV timespan is not long enough to rule out a second giant planet (which also could have been ejected during scattering), and imaging by Patience et al. (1998) only rules out companions more massive than 0.13 $M_{\odot}$ with projected separations $5 - 50$ AU.

Applying this idea more broadly, we have compared ages and circularization timescales for all known hot Jupiters and find evidence for two families of planets, distinguished by their orbital properties: (1) mostly circular orbits for the "dynamically old" planets, those with $\tau_{\rm cir} < t_{\rm age}$, and (2) a range of eccentricities for "dynamically young" planets, those with $\tau_{\rm cir} > t_{\rm age}$. If Type II migration were the leading driver of hot Jupiter migration, both dynamically young and old planets should have circular orbits. We thus conclude that HEM is important for producing hot Jupiters. However, we can only say that these planets have experienced dynamical stirring *at some point*, and do not suggest that this evidence shows Type II migration to be unimportant. On the contrary, as shown by simulations time and again, Type II migration is almost certainly important to orbital evolution before the gas disk dissipates, but we suggest that for a large fraction of hot Jupiter systems, planet-planet scattering or the Kozai mechanism is responsible for the final stages of inward migration. A larger sample of dynamically young (non-circularized) planets may allow us to determine what that fraction is. Since few hot Jupiters have circularization timescales greater than

1 Gyr, a good way to enhance this sample is to continue finding young planets.

That HEM mechanisms play an important role in hot Jupiter migration has already been suggested, and is supported by a rich data set of stellar obliquity measurements in hot Jupiter systems (see Albrecht et al. 2012b, for a recent discussion). In addition to the excitation of orbital eccentricity, dynamical encounters with a third body are expected to produce a range of orbital inclinations, although tidal interactions with the host star may realign the systems over time. These inclinations can be measured precisely, most notably via the Rossiter-McLaughlin effect (Rossiter 1924; McLaughlin 1924), and the results of such studies parallel those presented in this paper: systems for which the tidal timescale is short tend to be well-aligned, and those for which the timescale is long display high obliquities. Albrecht et al. (2012b) do caution that stars and their disks may be primordially misaligned for reasons unrelated to hot Jupiters, but we see no obvious reason for this to influence the eccentricities. Migration through multi-body dynamical interactions, on the other hand, could explain both the inclined orbits and high eccentricities observed in systems that have not yet experienced significant tidal interactions. Whether that process is primarily planet-planet scattering or the Kozai effect remains to be determined, and it is likely that more data will be needed to properly answer this question.

Finally, the tidal circularization boundary that separates the dynamically young and old populations of hot Jupiters is sensitive to the choice of the planetary tidal quality factor, $Q_{\rm P}$, so we have leveraged this dependence to constrain the typical value for hot Jupiters to be $\log Q_{\rm P} = 6.11^{+0.52}_{-0.23}$. $Q_{\rm P}$ has wide-ranging implications, e.g., for simulating orbital evolution

(Beaugé & Nesvorný 2012) or modeling the inflated radii of hot Jupiters (Bodenheimer et al. 2003), but has thus far proven difficult to constrain observationally. While our result still includes substantial uncertainty and will not be applicable to any one planet, it can be applied to these problems in a statistical sense. Moreover, it offers a path forward: as our sample of longer period and young hot Jupiters grows, the determination of $Q_{\rm P}$ using this method should improve.

CHAPTER 6

A CONTINUING SURVEY FOR WARM JUPITERS AND DISTANT COMPANIONS

Although our survey for planets in open clusters is most sensitive to hot Jupiters—short-period, massive planets induce larger RV amplitudes than their less massive and longer-period counterparts, and sampling the phase curve of a short period planet can be done quickly—we have designed the survey to also search for long period companions by observing stars over the course of several years. Given our measurement errors and a limited observing cadence over the course of multiple seasons, we expect that we will not be as sensitive to the lowest-mass gas giants, but we note that the frequency of long period giant planets is much higher than that of hot Jupiters, at least for field stars (the distribution is well-fit by a power-law with period dependence $dN \propto P^{0.26} d\ln P$, such that the planet fraction increases by a factor of $\sim$5 for periods greater than 300 days; Cumming et al. 2008). Those authors estimate that 17%-20% of stars host a gas giant planet within 20 AU (compared to $\sim$1% of stars that host a hot Jupiter; Wright et al. 2012; Mayor et al. 2011).

As mentioned in Chapter 3, we detect a number of stars that appear to show RV variations with a timescale of months or years. In this chapter we explore the properties of those systems, and where there is good evidence for an orbiting body we characterize the companions, some of which have well-defined orbits, and some of which exhibit only long-term trends. We also note that while our threshold for significant RV variation ($P(\chi^2) < 0.001$) works well for well-sampled orbits, a long-period companion that shows up as a long-term trend may not meet the threshold, yet may still be recognizable by eye as a companion. 4

stars fall into this category, though they require additional RVs to confirm the trends that have appeared to emerge in the most recent observations. Finally, we also include in this chapter brief notes on double-lined spectroscopic binaries whose RVs are consistent with cluster membership (we only have one or two spectra of these stars, having rejected them as good targets for a planet search), and single-lined spectroscopic binaries, for some of which we have derived preliminary orbital solutions.

6.1 Detected Orbits and Trends

Among the 35 stars discussed in this chapter that pass our $P(\chi^2)$ or "chi-by-eye" tests, 17 are single- or double-lined binaries, while 18 are low-amplitude variables that may plausibly be substellar companions ($M_{\rm P} \lesssim 67\,M_{\rm Jup}$). However, for several objects we are unable to place an upper limit on the orbital period, and many of these are likely to be low-mass stellar companions with long periods.

6.1.1 Planetary Companions

For 4 objects in 3 systems, we detect orbits from which we are able to constrain the companions to be of planetary mass. The first of these comes in a familiar system—an outer giant planetary companion to the hot Jupiter Pr0211b (see Chapter 4 and Quinn et al. 2012). Our continued observations of this system revealed a large amplitude ($K_{\rm c}{\sim}140\,{\rm m\,s^{-1}}$), high-eccentricity ($e{\sim}0.7$) companion with an estimated (but uncertain) period of nearly 5000 days (over 13 years). Despite the long period, we are able to obtain a strong constraint on the planetary mass ($M_{\rm c} = 7.79 \pm 0.33\,M_{\rm Jup}$) because our observations span the periastron

passage of the planet, during which the velocity reaches both its maximum and minimum for the orbit (see Figure 6.1). This planet discovery was published (Malavolta et al. 2016) as a collaboration with the GAPS consortium (Global Architectures of Planetary Systems), using our TRES data and data from the HARPS-N spectrograph. The properties of this planet (and of our other long-period planet candidates) can be found in Table 6.1. We note that our orbital solution for Pr0211b in Chapter 4 was actually a 2-planet fit from which we removed the orbit of Pr0211c (and vice versa here).

Pr0211c is particularly exciting because it marks the discovery of the first multi-planet system in a cluster, and its architecture provides tanatalizing circumstantial evidence for a system that has undergone planet-planet scattering. The presence of a hot Jupiter and a giant planet on a very eccentric, distant orbit is suggestive of a past encounter that excited the eccentricities of both planets, with the inner body experiencing a close approach to the star at periapse that circularized the orbit due to tidal friction. We suggest that a benchmark system like Pr0211 is well-suited for a detailed case study of giant planet migration. N-body simulations may help constrain the initial conditions—e.g., is a stellar flyby, like that proposed by Shara et al. (2016), necessary to produce the observed configuration, or can secular interactions between the planets produce an interaction that leads to this architecture, and if so, where were the initial orbits? It would be particularly interesting to know if the planet-planet scattering must occur well inside the snow line (after some initial inward migration), which has been suggested as one channel that can reproduce the known hot Jupiter population (e.g., Dawson et al. 2015). The discovery of additional multi-planet

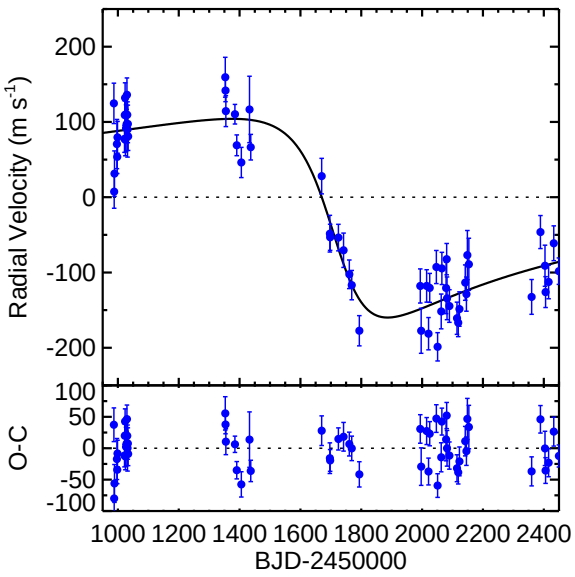

Figure 6.1 The orbit of Pr0211c (after removal of the Pr0211b RVs). We adopt an orbit similar to the one that we published in Malavolta et al. (2016), though we have updated our TRES RVs to account for better zero point corrections and additional data that we obtained this season. We show only the TRES data here.

systems in clusters would provide an even better foundation for such a study.

Fortunately, our survey is now poised to answer this call. We present here the detection of the second (candidate) multi-planet system in an open cluster, CB0036. The inner planet, with a minimum mass of 2.49 $M_{\rm Jup}$, orbits its host star with a period of 43.8 days and an eccentricity of 0.24. The outer planet, the properties of which are still somewhat uncertain, appears to be similar in mass ($M_c \sin i \sim 2.4$) and have an orbital period of 450 days and an eccentricity $\gtrsim 0.6$. The eccentricity is not yet precisely determined because we haven't observed the periastron passage, but there is a fairly strong constraint on the minimum eccentricity because most of the rest of the phase curve has been sampled (over the span of multiple orbits). Figure 6.2 shows the RVs of CB0036 and the best-fit orbital solutions.

While CB0036 is in some ways reminiscent of Pr0211 (e.g., both are systems of two super-Jupiters, with the outer planet on a very eccentric orbit), other features are quite distinct (the orbits of CB0036 are much more closely spaced, and the inner planet is a warm Jupiter, not a hot Jupiter). It therefore seems unlikely that CB0036 can be grouped with Pr0211 to bolster evidence for one particular migration channel; they may even have vastly different migration histories. Irrespective of these differences, though, CB0036 should be an invaluable piece of evidence for giant planet migration as a whole: it can provide insights that one cannot gain directly from studying hot Jupiters—specifically, CB0036 currently serves as *the only* example of a young warm Jupiter, and is one of only 9 systems to date containing a warm Jupiter and a second giant planet beyond 1 AU. The former point is important for one of the same reasons that young hot Jupiters are important: the timescale of migration and system properties at a young age (before, e.g., an outer companion can be distrupted) can provide clues about how a system formed and evolved. The latter point is of interest because it has been shown that warm Jupiters can be produced via a stalled version of the planetary Kozai mechanism (Dawson & Chiang 2014). The authors argue that systems formed in this manner should be likely to be observed with nearly orthogonal periapse angles, and we indeed find that CB0036 satisfies this condition: $\omega_b - \omega_c = 84\,\mathrm{deg}$. It would be convenient to find that all giant planets interior to the snow line migrated to where they are now via the same mechanism, but the true picture is undoubtedly much more complicated. While we expect that one or two migration channels are dominant in the orbital evolution of giant planets, it is not unrealistic to expect that among the numerous migration mechanisms proposed for

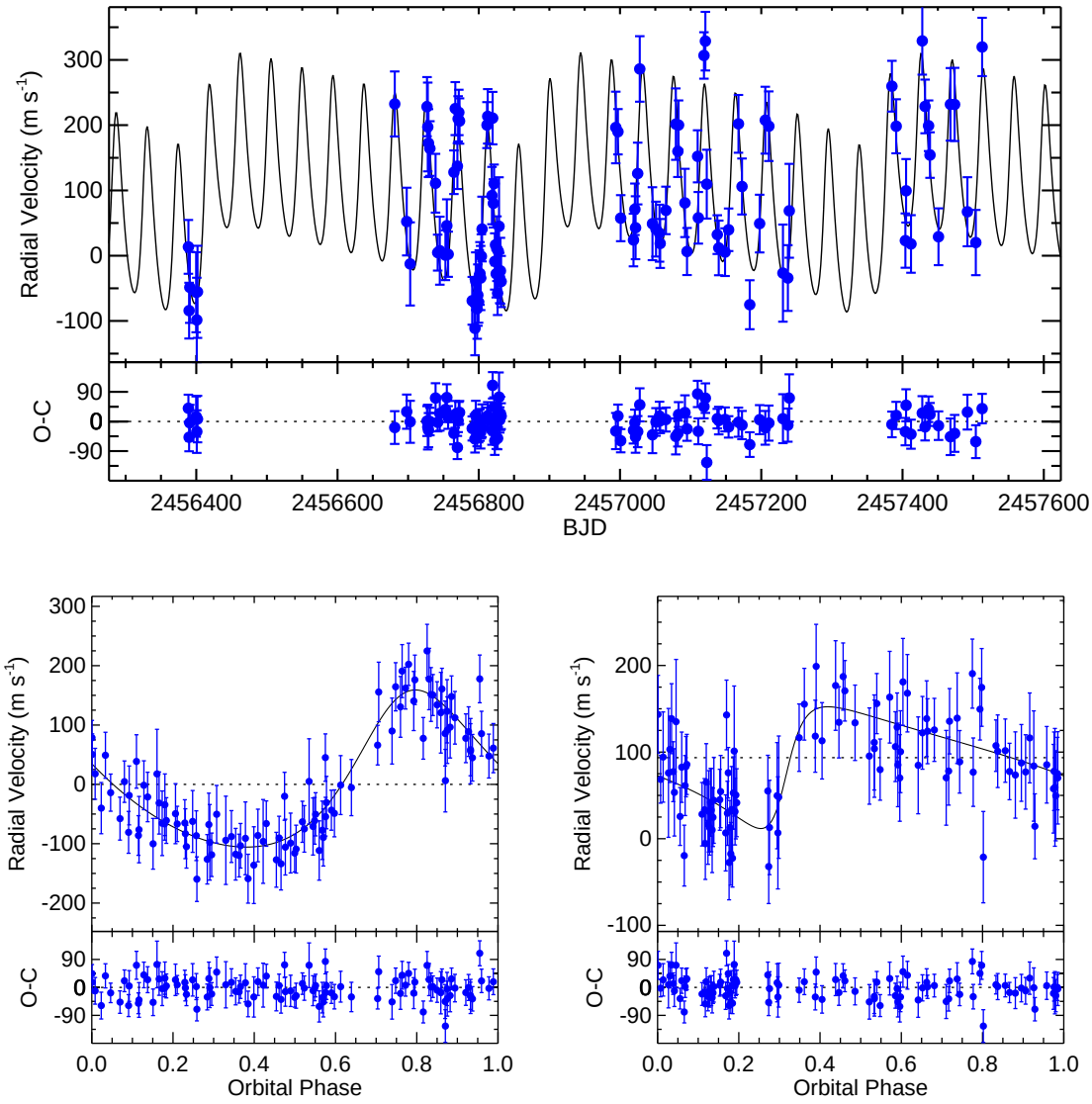

Figure 6.2 *Top*: Full timeseries of the CB0036 system, showing both the 44 day variation of the inner planet and the 450 day variation due to the outer planet. *Bottom:* The orbits of CB0036b (left) and and CB0036c (right).

giant planets, each of them is responsible for at least some fraction of planetary systems. CB0036 may serve as a benchmark system for one of those mechanisms.

The last of our long-period planets is Pr0157b, a massive ($9.58\,M_{\rm Jup}$) giant planet with an orbital period of over three years (1200 days). The orbit is shown in Figure 6.3. It, too,

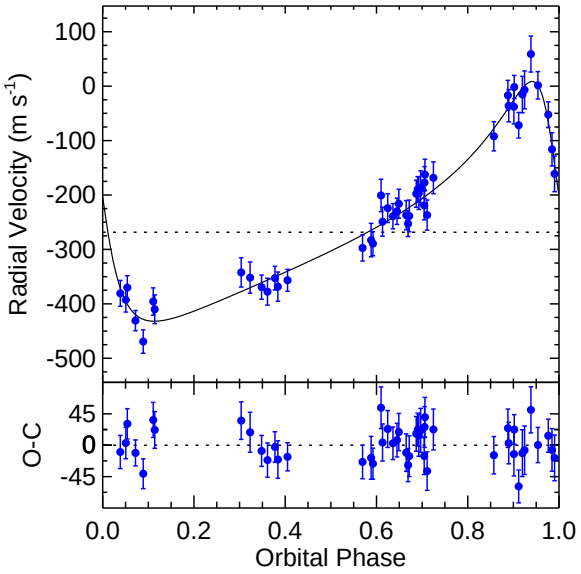

Figure 6.3 The orbital solution of Pr0157, a massive ($M_{\rm P} = 9.49\,M_{\rm Jup}$) planet in a 1200-day orbit. Like CB0036c and Pr0211c, it possesses a very high eccentricity. We suggest that these high eccentricities may be evidence of previous interactions with passing stars.

has a high eccentricity ($e = 0.57$). While a range of eccentricities can be expected for giant planets with long orbital periods, $e > 0.5$ is relatively uncommon. Only 10% of known giant planets with $P > 100$ days have eccentricities as high as 0.57, yet in our survey, all three long-period planets exceed this value. This may be an indication that planetary systems in clusters are more frequently disturbed by interaction with their stellar neighbors. While the chances of these eccentricities being observed are low ($\sim$0.07%) if the distribution is similar to the field, the population is not yet big enough to draw a strong conclusion. We are hopeful that we will be able to improve the statistics of this group, as some of our additional low-amplitude variables may turn out to be planets. We discuss these in the follow section.

Table 6.1: Long-Period System Properties

	Pr0211c	CB0036b	CB0036c	Pr0157b
Orbital Properties				
P [days]	4850^{+4560}_{-1750}	$43.831^{+0.039}_{-0.047}$	449^{+13}_{-12}	1234 ± 11
T_c [BJD]	2456694 ± 22	$2456997.17^{+0.68}_{-0.58}$	2456882^{+37}_{-24}	2455062^{+18}_{-22}
K [m s^{-1}]	138 ± 7	$130.3^{+4.4}_{-3.9}$	92^{+97}_{-44}	$220.4^{+4.1}_{-6.2}$
$\sqrt{e}\cos\omega$	-0.30 ± 0.11	$0.404^{+0.040}_{-0.051}$	$-0.37^{+0.25}_{-0.40}$	0.340 ± 0.029
$\sqrt{e}\sin\omega$	0.78 ± 0.09	$-0.287^{+0.061}_{-0.047}$	$-0.788^{+0.084}_{-0.076}$	$0.682^{+0.019}_{-0.023}$
e	0.71 ± 0.11	$0.239^{+0.027}_{-0.034}$	$0.69^{+0.20}_{-0.04}$	$0.577^{+0.023}_{-0.020}$
ω [deg]	111 ± 9	$-35.9^{+8.6}_{-6.5}$	-117^{+20}_{-28}	$62.8^{+3.2}_{-1.7}$
γ [km s^{-1}]	34.184 ± 0.198	-0.490 ± 0.173	-0.490 ± 0.173	34.169
Stellar and Planetary Properties				
$M_\star$ [$M_\odot$]	0.952 ± 0.040	1.2	1.2	0.9
$R_\star$ [$R_\odot$]	0.868 ± 0.078	1.2	1.2	0.8
$T_{\rm eff,\star}$ [K]	5326 ± 50	6411 ± 50	6411 ± 50	5875 ± 50
$\log g_\star$ [dex]	4.55 ± 0.10	4.22 ± 0.10	4.22 ± 0.10	4.60 ± 0.10
$v \sin i_\star$ [km s^{-1}]	4.8 ± 0.5	28.9 ± 0.5	28.9 ± 0.5	6.7 ± 0.5
[m/H] [dex]	0.187 ± 0.038	-0.13 ± 0.10	-0.13 ± 0.10	0.187 ± 0.038
Age [Myr]	578 ± 49	591 ± 50	591 ± 50	578 ± 49
$M_p \sin i$ [$M_{\rm Jup}$]	7.79 ± 0.33	2.49 ± 0.10	$2.7^{+1.5}_{-0.4}$	9.49 ± 0.66
$\sigma_\star$ [m s^{-1}]	26.7	0	0	12.5

Note — Stellar properties of Pr0211 come from Quinn et al. (2012). Stellar masses and radii of the other stars are approximate.

6.1.2 Possible Substellar Companions

Our possible substellar companions come in two main types. The first category includes long period objects, for which the partial orbit that we have observed is well fit by a linear or quadratic trend, or for which the curvature of the orbit is insufficient to place constraints on the orbital parameters. The second category includes objects for which we have observed nearly a full orbit, but which have masses very close to the hydrogen-burning limit—if the orbit does not complete soon, or if the orbital plane is not very close to edge-on, the companion will have to be a star. Figure 6.4 contains a gallery of the companions that manifest as RV trends with amplitudes small enough that several of these may well be planetary companions. Figure 6.5 includes the objects that may be substellar but will probably turn out to be low-mass stars (as well as the definite binaries). The properties of these objects are summarized in Table 6.2.

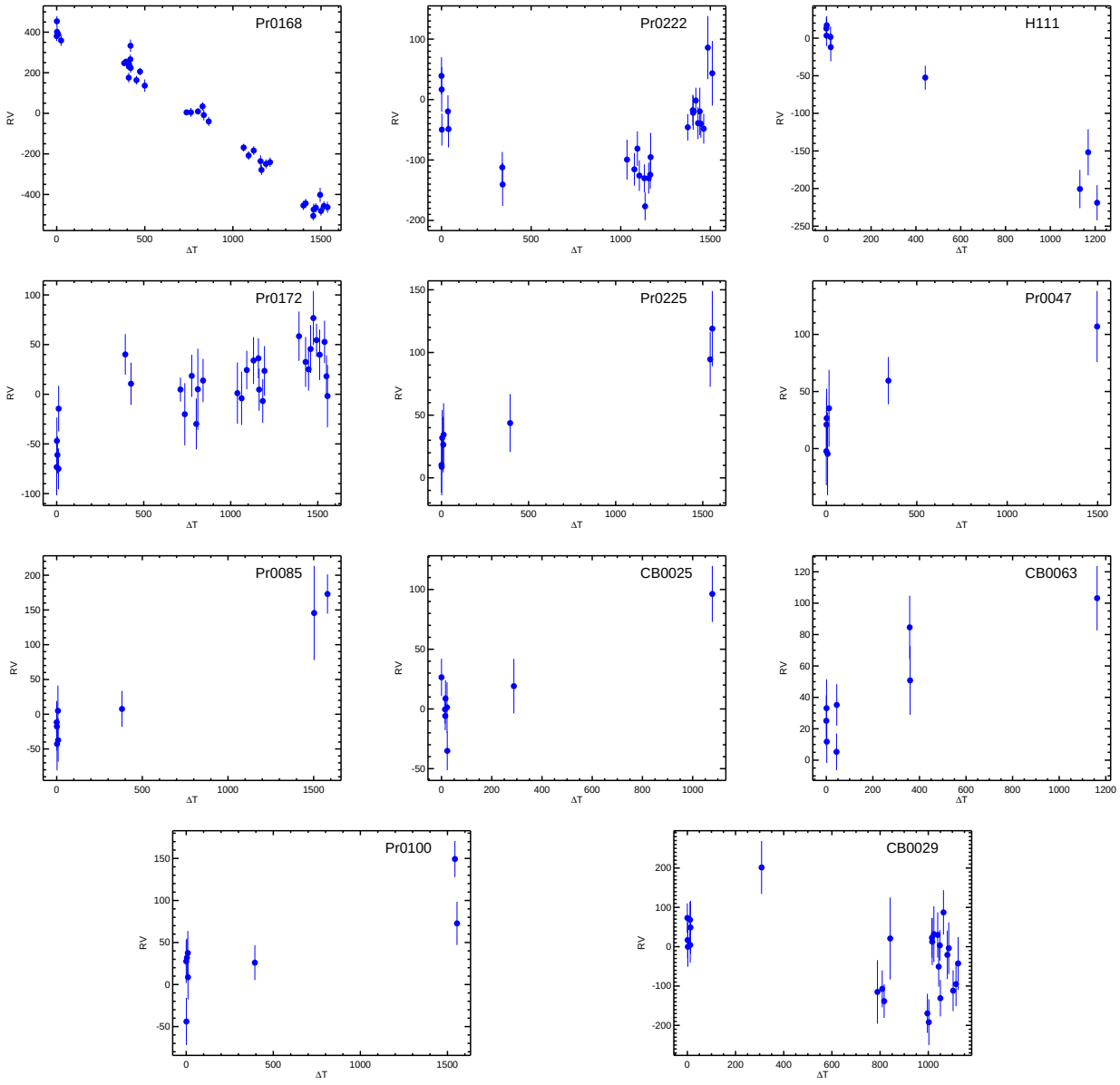

Figure 6.4 A gallery of possible substellar companions. Most exhibit trends, while the last two, Pr0100 and CB0029, may have periodicities on shorter timescales.

6.1.3 Binary Companions

We classify as binary companions those objects for which the orbital amplitude implies a minimum mass above the hydrogen-burning limit, or those that exhibit large (several km s^{-1})

RV variation over the course of only a few days. The long-period binaries have solved or partial orbits because until the RV amplitudes became too large, they were viable planet and brown dwarf candidates that we continued to observe. These objects are shown in Figure 6.5 and summarized in Table 6.2. The short-period stellar companions include Pr0123, Pr0164, and Pr0260, each of which was observed no more than 5 times. We stopped observing these three stars when it became clear that they could not host substellar companions.

Table 6.2: Properties of Binaries and Likely Binaries

Name	M_A ($M_\odot$)	P (days)	$M_B \sin i$ ($M_\odot$)	$M_B \sin i$ ($M_{\rm Jup}$)
CB0002	0.80	2520 ± 330	0.220 ± 0.019	231 ± 20
CB0022	1.17	3200 ± 1600	0.075 ± 0.016	79 ± 17
CB0065	0.97	81.2724 ± 0.0077	0.06961 ± 0.00019	72.92 ± 0.19
CB0086	1.00	2750 ± 100	0.05840 ± 0.00088	61.18 ± 0.92
Pr0035	1.17	$\sim$2480	$\sim$0.10	$\sim$110
Pr0058	1.13	1048.1 ± 2.0	0.1988 ± 0.0025	208.2 ± 2.6
Pr0121	0.98	...	...	...
HD109011	0.80	$\sim$494	$\sim$0.0980	$\sim$102.6
HD238224	0.65	$\sim$600	$\sim$0.0563	$\sim$59

Note — Uncertainties come from a simple Levenberg-Marquardt orbital fit, so they may be underestimated in the presence of correlated errors. Errors on companion mass do not include an error on the stellar mass, which is (crudely) estimated by comparing the $J - K$ color and spectroscopic $T_{\rm eff}$ to the mass relations of Kraus & Hillenbrand (2007). Objects without reported errors do not have reliable orbits (generally because the orbital period is longer than the time span of observations). In these cases, only weak constraints on the orbital period can be derived from the shape of the RV curve. We list one possible orbit for each of these stars, but the derived companion masses are strongly dependent upon the orbital periods, which may be much larger. Object masses are reported in units of $M_\odot$ and $M_{\rm Jup}$ to illustrate that some are consistent with a substellar mass to within the errors (including stellar mass uncertainty), and assuming near edge-on orientation. (However, we reiterate that these, too, are likely to be stars.) Pr0121 has a large gap in coverage, so it is also possible that the period is shorter than the observing time span, but the large variation suggests a likely stellar companion.

In addition we note the cluster members with composite spectra, which are probably indicative of a double-lined spectroscopic binary (but may also arise from hierarchical triple systems or chance alignments of stars on the sky). In Praesepe, we find 4 double-lined likely cluster members: Pr0125, Pr0179, Pr0226, and Pr0228. In Coma Berenices, we find another

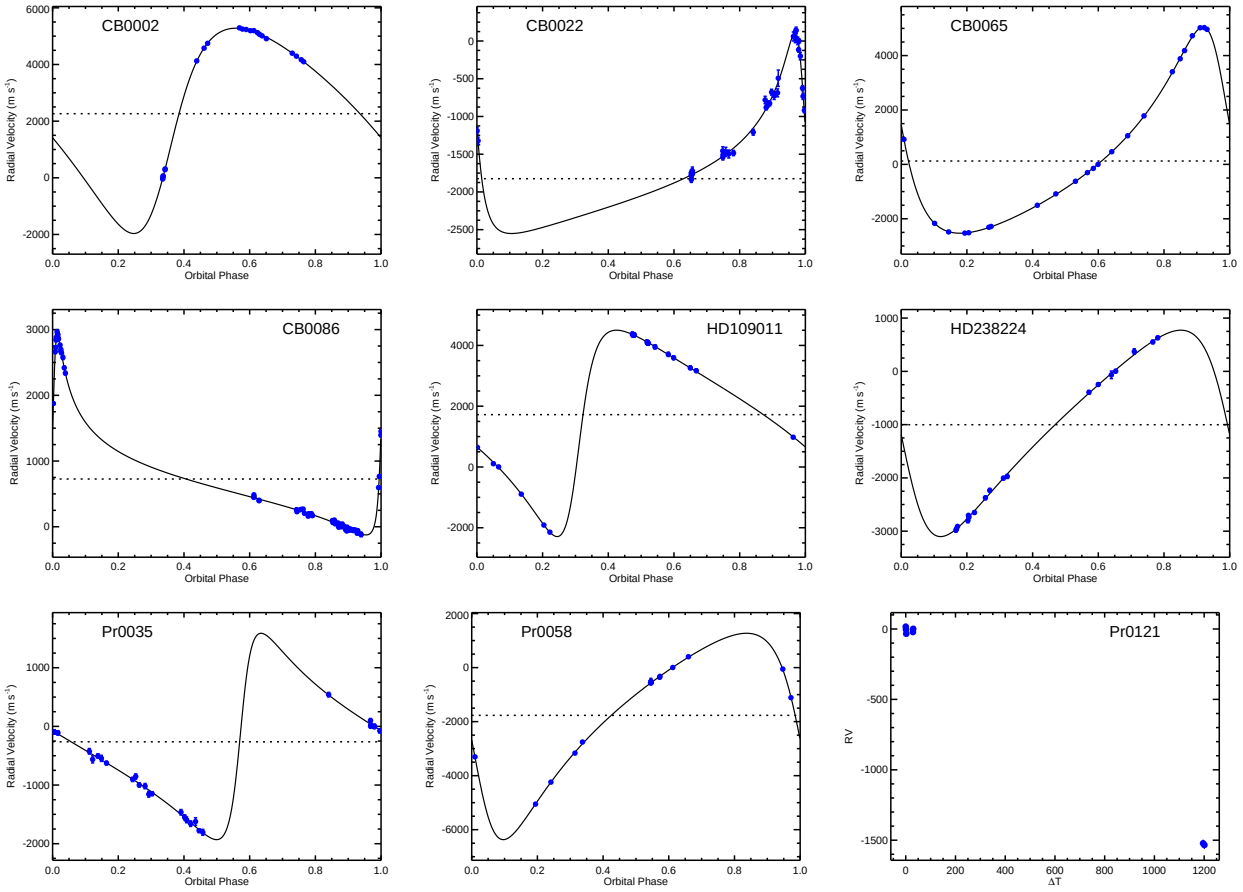

Figure 6.5 A gallery of systems hosting companions that are definitely or likely above the hydrogen-burning limit.

2: CB0043 and CB0082. In the Hyades, we believe VB14 to be a hierarchical triple system based on the apparent reflex motion of one set of lines that is blended with a second set of lines at nearly the same RV.

6.2 The Frequency of Warm and Cold Jupiters in Clusters

Now that we have detected several long-period planets (and have additional candidate detections) we can start to estimate the frequency of giant planets on wide orbits in clusters. As was the case for hot Jupiters, there will be significant uncertainty in this estimate, made

more extreme by the fact that we do not know the nature of most of our companions. If no additional stars end up hosting planets, we can at least estimate a lower limit on the frequency, and we can run a second, optimistic calculation by assuming that some fraction of our candidate planets are bona fide. For this purpose, we only include the candidate planets characterized for which the total velocity variation is less than $300\,\mathrm{m\,s^{-1}}$. This is an arbitrary cutoff and will correspond to a very rough estimate.

The absolute lower limit on the frequency of giant planets with $P > 10$ days is given by the raw counts: 4 planets from 128 non-binary stars subjected to our full survey, or 3.1%. (We do not include stars from the previous Hyades survey because we do not know how thoroughly they searched for long-period planets.) Of course, our survey is certainly not complete out to the periods we have considered. In fact, it is very unlikely that we would have detected Pr0211c ($P{\sim}4850$ days) around any of our stars that do not host interior planets, since it was the follow-up of the hot Jupiter Pr0211b that led to the improved sampling on a long timescale that allowed the detection of Pr0211c. One could make a similar argument for CB0036c. For this reason, we choose to limit our analysis to the frequency of planetary *systems*, and only consider periods less than 2000 days, both of which enable a simpler comparison to the field frequencies reported by Cumming et al. (2008), who consider only the frequency of systems in the period range 2-2000 days. These criteria bring our raw long-period planet total to 2/128, or 1.6% (3.9% when including hot Jupiters).

Next, we must account for incompleteness in the survey, for which we use a similar method as the one described for the hot Jupiters in Chapter 4. Namely, we simulate orbits

and sample them with our actual observing cadences and measurement errors. This time, however, we draw masses and periods from the distribution described by Cumming et al. (2008), $dN = CM^{-0.31}P^{0.26}d\ln Md\ln P$, where C is just a constant that governs the overall occurrence rate. Our simulations give us the fraction of planets detected by our survey, which we can divide into our raw counts to estimate the total number of planets present around our survey stars. Note that this assumes that the shape of the distribution in clusters is similar to the that of the field, and it is not immediately apparent that this should be the case. If, for example, long period planets in clusters are more often ejected (or prevented from forming) by nearby stars, we might expect a different distribution of masses and periods. If they migrate at a higher rate, or via different mechanism, we might again expect a different distribution. However, given that the biggest uncertainty is currently the raw counts, we leave such considerations for future work. These simulations (of which the results for one star are shown in Figure 6.6) lead to a derived survey completeness of $\sim$40% for planets in the mass and period ranges considered. Therefore, if all cluster planets follow field distributions—and if we assume that none of our candidate planets are real—the overal planet occurrence rate should be $\sim$9.8%. If, on the other hand, we assume (as an example) that 3 candidate planets will turn out to be real, the occurrence rate jumps to 15.6%. Given that the field occurrence rate in this mass and period range is 10.5% (Cumming et al. 2008), we need to determine the nature of our unsolved RV variables in order to begin to compare occurrence rates in clusters and the field. This is a worthwhile exercise, as this comparison can yield insight into the processes that shape planetary system architectures in clusters, and in general.

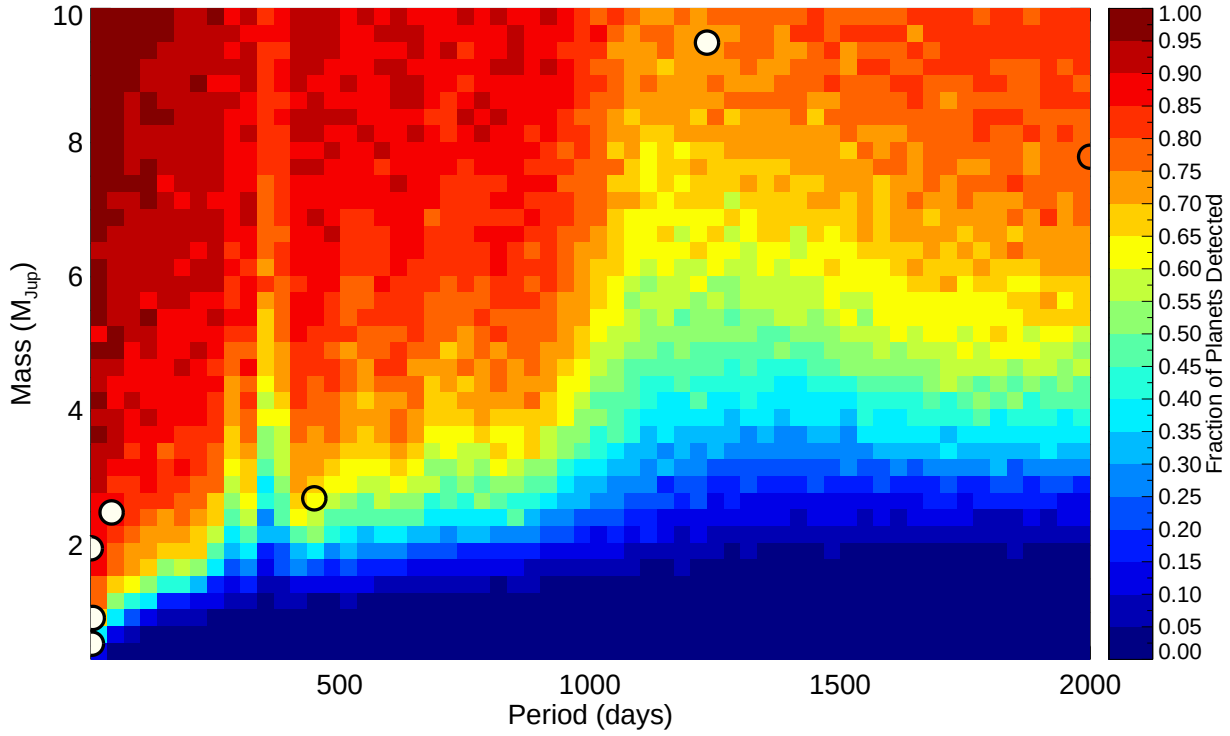

Figure 6.6 A heat map showing the detection efficiency out to long periods for Pr0222. For this star, and for many Praesepe stars, the long time span of observations provides sensitivity to long periods, but a gap in coverage during the middle of the survey leads to reduced sensitivity at periods of a few years. While most of the range shown has a detection efficiency greater than 50%, planets are drawn from a realistic distribution (low-mass and long-period planets being more common), and as a result we estimate that we would detect only ∼48% of any hypothetical giant planets orbiting this star. We overplot our 7 discovered planets as black circles (with Pr0211c at the edge of the plot despite its longer period). We fill with white only the first planet in each system, as the outer planets may not have been detected unless the inner planets were followed-up.

CHAPTER 7

AN ADAPTIVE OPTICS SURVEY FOR STELLAR COMPANIONS TO HOT JUPITER HOSTS

In this chapter, we present the preliminary results of an adaptive optics survey for stellar companions to known hot Jupiter host stars—the largest such survey carried out to date. This survey is an excellent complement to the science goals of our open cluster RV planet search, both in terms of the parameter space we survey for companions, and the constraints on giant planet migration we hope to achieve. While our RV survey is limited (by measurement precision and time span of observations) to detection of planets roughly within the orbit of Jupiter—and, by design, around single stars—our AO survey will be sensitive only to stellar companions (and possibly some massive brown dwarfs) orbiting their hosts at distances of tens to hundreds of AU and beyond, making each detection part of a planetary system that contains at least three bodies. As discussed previously, a major scientific strength of the RV survey is in the youth of the planetary systems; orbital properties of migrating planets can reveal the mechanism by which they migrate—Type II or HEM (such as planet-planet scattering or Kozai cycles). The AO survey, on the other hand, leverages information from the architectures of the planetary systems to distinguish *which* type of HEM may be important, as the frequency and properties of binary companions to hot Jupiter systems have the potential to reveal stellar Kozai cycles as a primary source of migration. For example, if Kozai migration plays a prominent role in the production of hot Jupiters, then short-period giant planets should often have stellar companions—more often than the typical star does. Moreover, those systems should frequently display spin-orbit misalignment and

eccentric orbits before realignment and circularization (see, e.g., Storch et al. 2014). These provide two easily testable predictions that would indicate Kozai migration is important for hot Jupiters.

The statistics of planets in binary systems are also important from the perspective of formation theories. Binary companions are expected to disrupt planet formation, perhaps through truncation of the planet-forming disk, if the binary orbital separation is small enough. Kraus et al. (2016), for example, show evidence that binaries closer than about 50 AU are significantly less likely to host planets in the *Kepler* data set. Hot Jupiters may be a particularly interesting subset of planets in binaries, as the presence of a binary has the potential to enhance inward migration efficiency (e.g., directly through Kozai cycles, or by inducing scattering events in multi-planet systems) while at the same time suppressing formation. Which mechanism wins out may hold further clues to the physical processes at play.

Finally, we note that the presence of an undetected close stellar companion can dramatically affect the derived properties of transiting planets, but the majority of transiting hot Jupiters were not subjected to high-resolution imaging before publication of their properties. As such, there may be a number of significantly biased planetary properties in the literature, and understanding the sizes, masses, and in turn, bulk densities of hot Jupiters is important. We use this information to help deduce, e.g., compositions, core masses, scale heights of the atmospheres, and more, some of which can be used to select targets for time-intensive follow-up studies. Therefore, it is worth getting accurate measurements. One illustrative

example of how an unseen companion can be a pernicious force in a planetary system is Kepler-14 (Buchhave et al. 2011). Kepler-14A has a stellar companion, Kepler-14B, only 0.5 magnitudes fainter that was not detected in seeing-limited imaging because the projected separation between the two stars is only $0''.3$. Buchhave et al. (2011) demonstrate that if no AO images were obtained and the companion had gone undetected, the planetary mass and radius would have been underestimated by 60% and 10%, respectively, due to dilution of the RV amplitude and of the transit depth. While it is unlikely that many hot Jupiters hosts also harbor a nearly equal-brightness companion within an arcsecond or less, even a small number of such companions (or a large number of slightly fainter companions) could introduce a bias into our understanding of giant planet properties, in individual systems as well as in the overall population.

Many other groups have begun searching for close stellar companions to planetary systems using high-resolution imaging techniques that include adaptive optics, speckle interferometry, and lucky imaging (see, e.g., Howell et al. 2011; Adams et al. 2012; Bergfors et al. 2013; Law et al. 2014; Wang et al. 2014; Ngo et al. 2015). While some large samples have been surveyed—especially from the *Kepler* data set—most of these surveys either target small planets (accomplishing a different set of science goals), lack the large sample sizes necessary to draw significant conclusions about the population, or lack the sensitivity to detect the smallest stellar companions, leaving the survey somewhat incomplete. Of the published surveys, Ngo et al. (2015) is most similar to ours in terms of science (studying the system properties of a sample of northern hot Jupiters) and sensitivity (using the 10-m Keck tele-

scope), but their sample was only just over a half the size of ours, so we are hopeful that we will reach more firm conclusions in the areas in which their statistics were limited.

7.1 The Sample and Observations

We select our sample from the known transiting hot Jupiters discovered from the ground that are visible from the Gemini Observatory in Hawaii. We restrict our sample to the ground-based discoveries because these planets have not generally benefitted from the wide array of follow-up resources devoted, for example, to *Kepler* planet candidates, which routinely receive AO imaging for vetting purposes. Moreover, these transiting planets tend to be brighter than the space-based discoveries, yet still far enough away that seeing-limited images do not usually probe very close physical separations (and at about the right distance for 0.″1-resolution images to probe to a few tens of AU, outside of which we can expect to observe binary companions to planetary systems). RV planets, on the other hand, tend to be so close that much of the interesting parameter space can already be ruled out by seeing-limited imaging, and these systems often have up to a decade or more of precise RV monitoring, which could aready indicate the presence of a stellar companion. At the onset of our survey, 93 stars matched these criteria.

Observations were carried out using the Altair AO system and the Near InfraRed Imager (NIRI) on Gemini North in the J and K bands. NIRI is a 1024×1024 ALADDIN InSb array, which, using the f/32 camera provides a pixel scale of $0.''022\,\mathrm{pixel}^{-1}$ for a field of view of $22'' \times 22''$. All of our targets are bright enough to be used as natural guide stars. We

observe each star with a 3×3 dither pattern in $4''$ offsets, leading to an effective FOV roughly $7''$ on a side, though brighter companions can be detected at much larger distances using a subset of the frames.

7.2 Reduction and Analysis

NIRI has a number of known issues that must be accounted for in the observing or reduction process. The first frame in every sequence of exposures (e.g., a set of dithered images of a star) is known to produce an offset bias pattern of variable strength. As a result, the instrument scientists recommend that the first frame of any sequence (including darks and flats) be excluded from analysis. To prevent significant losses, we start every science sequence with a short, "dummy" exposure to absorb this effect before moving on to our planned sequence. We do, however, reject the first frames of the calibration sequences. The detector is also known to produce pattern noise: vertical striping, horizontal banding, and quadrant offsets are all common, and we run the provided python script `cleanir.py` to remove these features. A second script, `nirlin.py`, corrects for non-linear response when the counts approach full-well depth. We reduce the data using the Gemini IRAF package to perform standard image reduction (bias, dark, and flatfield removal), but we note that not all of the data quirks seem to be corrected for using these scripts and packages. We employ some custom routines to subtract off remaining systematics in the background, for example. We run the IDL routine `undistort.pro` provided by Gemini to correct for distortion in Altair/NIRI images, and we finish by shifting, rotating, and coadding images using our own code.

We use multiple methods to identify companions in our images. For the region far from the star (outside the seeing halo at about $\sim 2''$), we simply use SExtractor (Bertin & Arnouts 1996) to identify sources and perform aperture photometry, setting a threshold of 5-σ for detection. We discuss this criterion in more detail below. For regions near the central star, we must cope with the point spread function (PSF) of the central star and the speckle pattern, both of which can produce more signal than some companions, in order to identify faint sources. While we have experimented with several techniques (e.g., PSF-fitting using an analytical model, removal of the median PSF, empirical PSF subtraction using other targets), we ultimately settle on a multi-step process that first removes the star's PSF and then removes the speckles. We note that for this close-in region we use versions of the coadded images that have *not* been rotated before being shifted—we find that the small-angle rotation of the field during a sequence does not impact companion detection much at small separations (where the linear offset is very small), but the speckle pattern is pseudo-stable in x and y (*not* in RA and DEC), so we are able to leverage information about the speckles from all target images if we do not rotate them. To remove the PSF of the central star, we use a semi-analytical approach that fits both a 2D Moffat profile to the central peak to remove the bulk of the signal, and a cubic spline to the mean residual radial profile to account for the Airy disk and (symmetric) deviations from the assumed Moffat profile. Apart from within the central 3-4 pixels, where PSF asymmetries (sometimes due to saturation) cause problems, this does a good job of removing the light from the central star. We mask out this central region with large residuals for the remainder of the analysis.

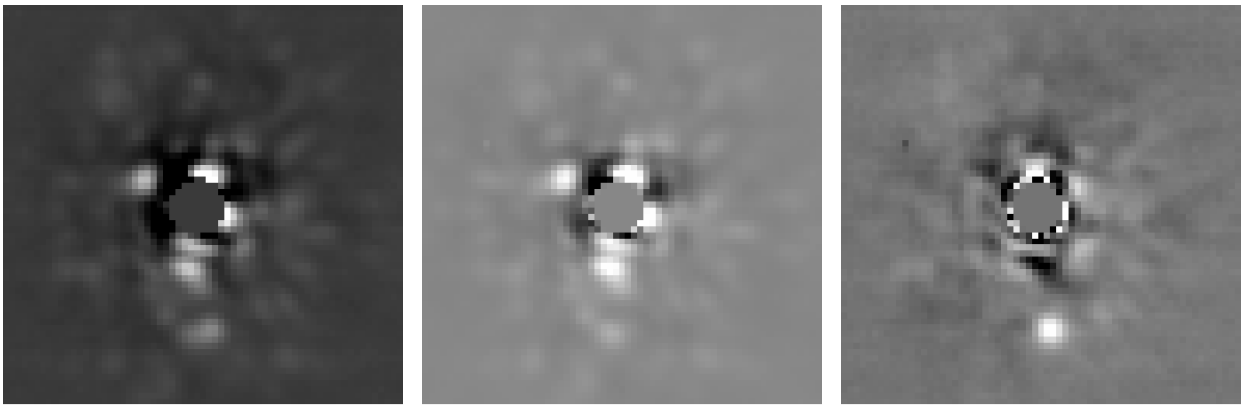

Figure 7.1 These three images are all centered on the hot Jupiter host XO-3 (the PSF of which has been subtracted) and have the same logarithmic brightness scale. In the left image, the speckle pattern is evident. The middle image is generated from the eigenspeckles, which were calculated via PCA from a set of 70 K-band images, in order to best match the observed image on the left. The right image is the difference of the other two images. A companion, barely visible in the original image—and indistinguishable from the speckles around it—is clearly detected in this difference image.

To remove the speckles, we take advantage of the fact that they are pseudo-stable across our three semesters of observing, and employ a principal component analysis (PCA) to identify the primary speckle modes—which we call "eigenspeckles"—and remove the best-fit linear combination of those modes from each image. In our data, PCA successfully suppresses the speckles enough that we are able to identify some companions that lie within the speckle pattern but are actually fainter than many of the speckles. Figure 7.1 illustrates the process for the XO-3 planetary system.

One problem with adopting two modes of companion detection is that assessing the properties of the companions and the completeness of the survey becomes more complicated. While wide companions can be measured via standard aperture photometry, the PCA analysis used to remove speckles and detect close companions can slightly alter the

companion properties. Some fraction of the companion signal will almost always find its way into the modes that are used to reconstruct the speckle pattern and be subtracted off when the speckles get used. We suggest that one way to adjust for this is to inject stars into the images, run PCA, and see how the speckle-subtracted synthetic companion properties have changed in order to reverse the effects that PCA has on a true companion. This is something we have not yet implemented, so in this work we report only positions of companions, not the magnitudes. This will be included as we move toward publication of the survey. Similarly, we assess detection limits by injecting synthetic stars at a range of separations, position angles, and contrasts—generated using the semi-empirical PSF described above—and running SExtractor as we would for a real companion. At each separation (and averaged over PA), we find the contrast ratio at which we no longer detect 95% of companions at the level of 5-σ. (We selected a threshold of 5-σ because this was the value at which we detected no false positives.) These maximum contrast ratios, as a function of separation, form our detection limits. Our two complementary techniques for companion detection (aperture photometry at large separations, and PSF removal plus PCA plus aperture photometry at small separations) will actually have different contrast curves because PCA removes some signal from the companions (with no significant corresponding noise reduction at wide separations), but at some intermediate separation, the PCA method becomes better, so our final contrast curves will come from the maximum of the two methods at each separation.

7.3 Visual Stellar Companions to Hot Jupiter Hosts

From our preliminary analysis of the reduced images of 93 hot Jupiter hosts, we identify 50 companions to 42 stars with separations less than 8″. These companions are listed in Table 7.1. While we do not have finalized detection limits, and thus cannot yet quantitatively estimate the completeness of the survey, we expect that we have detected most companions out to 8″ but that there are some faint stars within the residual speckle pattern that we are unable to detect. Some wide binaries will fall outside the separation range considered ($\rho < 8''$) and some stars, even those on wide orbits, will by chance be too close in projection for us to detect at the current epoch. We also expect that very few (if any) of these companions will turn out to be background stars. The first reason for this is that similar surveys have found a very low occurrence of background stars (see, e.g.,), probably because most of these stars lie away from the galactic plane; the crowded fields toward the galactic plane make for difficult transit surveys, so the parent sample from which these systems originated preferentially came from fields with low probabilities of chance alignments. The second reason comes from our observed distribution of companion separations. The incidence of background stars will scale with the square of the separation—the area of sky between 7″ and 8″ separation, for example, is 5 times as large as the area between 1″ and 2″—but we observe no such rise in the frequency of wide companions. (We find 9 companions between 1″ and 2″ but only 4 between 7″ and 8″, despite wide companions being easier to detect.) We note here that when our photometry is finalized we can use the colors and magnitudes of the companions to help assess whether they are located at the same distances as their primaries. These

considerations—that our survey is likely of high fidelity but not complete—suggest that our observed companion fraction of 45% (42/93) is a lower limit.

Table 7.1: Stars with Detected AO Companions

Star	α ($hh:mm:ss$)	δ ($dd:mm:ss$)	Epoch (BJD)	Sep ($''$)	PA ($^\circ$)
HAT-P-5	18 : 17 : 37.30	+36 : 37 : 16.80	2012.51476407	4.40	268.46
HAT-P-6	23 : 39 : 05.81	+42 : 27 : 57.50	2012.51499048	6.55	48.86
HAT-P-7	19 : 28 : 59.36	+47 : 58 : 10.20	2012.52837203	3.91	90.11
				3.13	267.31
HAT-P-8	22 : 52 : 09.86	+35 : 26 : 49.50	2012.51494782	1.05	133.99
HAT-P-14	17 : 20 : 27.87	+38 : 14 : 31.90	2012.58819767	0.87	265.81
HAT-P-15	04 : 24 : 59.53	+39 : 27 : 38.30	2012.67922368	6.19	238.89
				7.21	193.41
HAT-P-16	00 : 38 : 17.56	+42 : 27 : 47.20	2012.72564606	0.71	146.62
				0.70	147.67
HAT-P-18	17 : 05 : 23.15	+33 : 00 : 44.90	2012.70028801	2.71	186.86
HAT-P-20	07 : 27 : 39.95	+24 : 20 : 11.30	2013.26965310	7.16	318.23
				6.89	318.81
HAT-P-24	07 : 15 : 18.02	+14 : 15 : 45.30	2012.75869986	5.01	170.55
HAT-P-27	14 : 51 : 04.19	+05 : 56 : 50.50	2012.60184536	0.67	28.28
HAT-P-28	00 : 52 : 00.19	+34 : 43 : 42.20	2012.65988292	1.02	219.30
HAT-P-29	02 : 12 : 31.49	+51 : 46 : 43.50	2012.69577757	0.38	55.85
				3.56	151.06
HAT-P-30	08 : 15 : 47.98	+05 : 50 : 12.30	2012.75057242	3.88	3.17
HAT-P-32	02 : 04 : 10.28	+46 : 41 : 16.20	2012.65991648	2.99	105.08
HAT-P-35	08 : 13 : 00.18	+04 : 47 : 13.30	2013.32987969	0.95	137.74
HAT-P-39	07 : 35 : 01.98	+17 : 49 : 48.30	2013.35177992	0.92	95.08
HAT-P-41	19 : 49 : 17.44	+04 : 40 : 20.70	2013.21602127	3.69	183.92
				7.95	231.18
KELT-2A	06 : 10 : 39.35	+30 : 57 : 25.70	2013.26961457	2.43	328.81
TrES-1	19 : 04 : 09.84	+36 : 37 : 57.54	2012.51487158	2.42	172.33
				5.02	142.97
				6.37	53.62
TrES-2	19 : 07 : 14.04	+49 : 18 : 59.00	2012.51484887	1.14	125.11
TrES-4	17 : 53 : 13.06	+37 : 12 : 42.30	2012.64545217	1.58	1.30
WASP-1	00 : 20 : 40.08	+31 : 59 : 23.70	2012.67324640	4.67	2.84
WASP-2	20 : 30 : 54.13	+06 : 25 : 46.30	2012.52049093	0.74	104.12
WASP-3	18 : 34 : 31.62	+35 : 39 : 41.50	2012.51482504	1.21	87.95
WASP-8	23 : 59 : 36.07	−35 : 01 : 52.80	2012.51500676	4.55	169.16
WASP-11	03 : 09 : 28.54	+30 : 40 : 24.70	2012.68757629	0.34	219.01
WASP-12	06 : 30 : 32.79	+29 : 40 : 20.20	2012.69574055	1.08	253.85
				1.08	250.13
WASP-14	14 : 33 : 06.36	+21 : 53 : 40.90	2012.58805488	1.48	101.44
WASP-33	02 : 26 : 51.06	+37 : 33 : 01.81	2012.66019739	1.97	275.14
WASP-36	08 : 46 : 19.30	−08 : 01 : 37.00	2013.36550441	4.97	66.34
WASP-37	14 : 47 : 46.56	+01 : 03 : 53.80	2013.32774848	0.49	26.30
				3.20	6.43
WASP-39	14 : 29 : 18.41	−03 : 26 : 40.10	2012.58803923	7.36	129.98
WASP-45	00 : 20 : 57.00	−35 : 59 : 53.80	2013.53068230	4.44	311.40
WASP-48	19 : 24 : 38.98	+55 : 28 : 23.30	2012.65135367	3.67	223.86
WASP-49			2013.18491390	2.32	177.34
WASP-55	13 : 35 : 01.95	−17 : 30 : 12.70	2013.32770253	4.43	162.63
WASP-66	10 : 32 : 53.99	−34 : 59 : 23.44	2013.34631488	0.28	110.70
WASP-67	19 : 42 : 58.51	−19 : 56 : 58.41	2013.28989692	4.51	52.62
				6.16	70.03
XO-3	04 : 21 : 52.70	+57 : 49 : 01.80	2012.67926405	0.44	291.32

Table 7.2: Stars without AO Companions

Star	α $(hh:mm:ss)$	δ $(dd:mm:ss)$
HAT-P-1	22 : 57 : 46.83	+38 : 40 : 29.80
HAT-P-2	16 : 20 : 36.37	+41 : 02 : 53.36
HAT-P-3	13 : 44 : 22.58	+48 : 01 : 43.20
HAT-P-4	15 : 19 : 57.93	+36 : 13 : 46.79
HAT-P-9	07 : 20 : 40.48	+37 : 08 : 26.10
HAT-P-11	19 : 50 : 50.14	+48 : 04 : 49.06
HAT-P-12	13 : 57 : 33.48	+43 : 29 : 36.70
HAT-P-13	08 : 39 : 31.81	+47 : 21 : 07.30
HAT-P-17	21 : 38 : 08.73	+30 : 29 : 19.40
HAT-P-19	00 : 38 : 04.01	+34 : 42 : 41.50
HAT-P-21	11 : 25 : 05.99	+41 : 01 : 40.60
HAT-P-22	10 : 22 : 43.59	+50 : 07 : 42.00
HAT-P-23	20 : 24 : 29.72	+16 : 45 : 43.70
HAT-P-26	14 : 12 : 37.54	+04 : 03 : 36.10
HAT-P-31	18 : 06 : 09.05	+26 : 25 : 35.90
HAT-P-33	07 : 32 : 44.22	+33 : 50 : 06.10
HAT-P-34	20 : 12 : 46.88	+18 : 06 : 17.40
HAT-P-36	12 : 33 : 03.91	+44 : 54 : 55.10
HAT-P-37	18 : 57 : 11.06	+51 : 16 : 08.80
HAT-P-40	22 : 22 : 03.10	+45 : 27 : 26.40
HATS-1	11 : 42 : 06.08	−23 : 21 : 17.40
Qatar-1	20 : 13 : 31.61	+65 : 09 : 43.48
TrES-3	17 : 52 : 07.02	+37 : 32 : 46.20
TrES-5	20 : 20 : 53.25	+59 : 26 : 55.60
WASP-6	23 : 12 : 37.75	−22 : 40 : 26.10
WASP-10	23 : 15 : 58.30	+31 : 27 : 46.20
WASP-13	09 : 20 : 24.70	+33 : 52 : 56.60
WASP-15	13 : 55 : 42.70	−32 : 09 : 34.60
WASP-16	14 : 18 : 43.92	−20 : 16 : 31.80
WASP-17	15 : 59 : 50.95	−28 : 03 : 42.30
WASP-21	23 : 09 : 58.25	+18 : 23 : 45.80
WASP-22	03 : 31 : 16.32	−23 : 49 : 10.90
WASP-24	15 : 08 : 51.74	+02 : 20 : 35.90
WASP-25	13 : 01 : 26.37	−27 : 31 : 19.90
WASP-26	00 : 18 : 24.70	−15 : 16 : 02.30
WASP-28	23 : 34 : 27.88	−01 : 34 : 48.13
WASP-31	11 : 17 : 45.36	−19 : 03 : 17.20
WASP-32	00 : 15 : 50.85	+01 : 12 : 00.70
WASP-34	11 : 01 : 35.89	−23 : 51 : 38.30
WASP-35	05 : 04 : 19.63	−06 : 13 : 47.30
WASP-38	16 : 15 : 50.36	+10 : 01 : 57.30
WASP-41	12 : 42 : 28.50	−30 : 38 : 23.50
WASP-43	10 : 19 : 38.01	−09 : 48 : 22.50
WASP-44	00 : 15 : 36.77	−11 : 56 : 17.30
WASP-50	02 : 54 : 45.13	−10 : 53 : 53.00
WASP-61	05 : 01 : 11.92	−26 : 03 : 14.90
WASP-78	04 : 15 : 01.50	−22 : 06 : 59.10
WASP-79	04 : 25 : 29.02	−30 : 36 : 01.50
XO-1	16 : 02 : 11.84	+28 : 10 : 10.40
XO-2	07 : 48 : 06.47	+50 : 13 : 32.90
XO-4	07 : 21 : 33.17	+58 : 16 : 05.00
XO-5	07 : 46 : 51.96	+39 : 05 : 40.40

7.4 Evidence for Kozai Migration

When we compare our derived lower limit of the incidence of binary companions ($f_{\rm bin} \gtrsim 45\%$) to that of Solar-type field stars ($\sim$44% reside in multiple systems; Raghavan et al. 2010), we conclude that the typical hot Jupiter host is more likely than the average field star to reside in a binary system. Moreover, from the orbital period distribution presented in Raghavan et al. (2010) (their Figure 13), and a typical distance to our hot Jupiter hosts of a few hundred parsecs, we can see that the separation range probed by our images ($0\farcs15 \lesssim \rho < 8''$) covers roughly the peak of the binary orbital period distribution down to about the half-maximum. Since the distribution is normal, we can estimate that perhaps 15% of companions in our sample lie beyond $8''$, and the total binary frequency for hot Jupiter hosts is probably greater than 50%. Recall that an elevated binary fraction was one of the predictions that follows if Kozai migration is important for producing hot Jupiters. A more rigorous analysis of the false positive rate and survey completeness—which will be included when this survey is published—will improve our confidence in this conclusion.

Finally, we examine the obliquity distribution of our sample. Much work has been done in recent years to measure the spin-orbit angles of hot Jupiter systems, and a compilation of those measurements is maintained by René Heller at his webpage[1]. Among planets with measurements of the sky-projected spin-orbit angle, λ, we find 52 systems in common with our survey. Figure 7.2 shows which of these systems have detected companions (blue circles)

[1] http://www2.mps.mpg.de/homes/heller/

and plots their projected physical separations against λ. The red triangles indicate the rough limits outside of which we can exclude companions. We define a system to be misaligned if its spin-orbit angle is greater than 20 degrees (the green hatched region in the plot) and well-determined ($\lambda/\sigma_\lambda > 2$). If it meets the former condition but not the latter, we consider it aligned. We find several trends of note. First, we see that systems without stellar companions tend to cluster at low spin-orbit angles (the group of red triangles near 0 degrees), while those with companions (blue circles) possess a wide range of obliquities. In fact, 82% of hot Jupiters without AO companions (23/28) are well-aligned to the stellar spin, whereas only 42% (10/24) of hot Jupiters in binaries are well-aligned. Similarly, if we consider only the misaligned systems, we find that 74% of them (14/19) reside in binaries, while only 30% (10/33) of aligned hot Jupiters reside in binaries. Recall that these results—hot Jupiters in binaries are more likely to be misaligned—are another prediction that follows if Kozai migration is important to the production of hot Jupiters.

While these promising results seem poised to place some more quantitative limits on the contribution that Kozai migration makes to the orbital evolution of giant planets, they appear slightly inconsistent with previous work, so we will have to consider the analysis carefully as we move toward publication. Specifically, Ngo et al. (2015) found no correspondence between misalignment and the incidence of imaged companions, though it is possible that their smaller sample size of 50 stars (only some of which have measured λ, with those split further in order to compare populations) was simply too small to significantly detect such a correlation. We must also carefully consider the other properties of the system, as it is possible that the

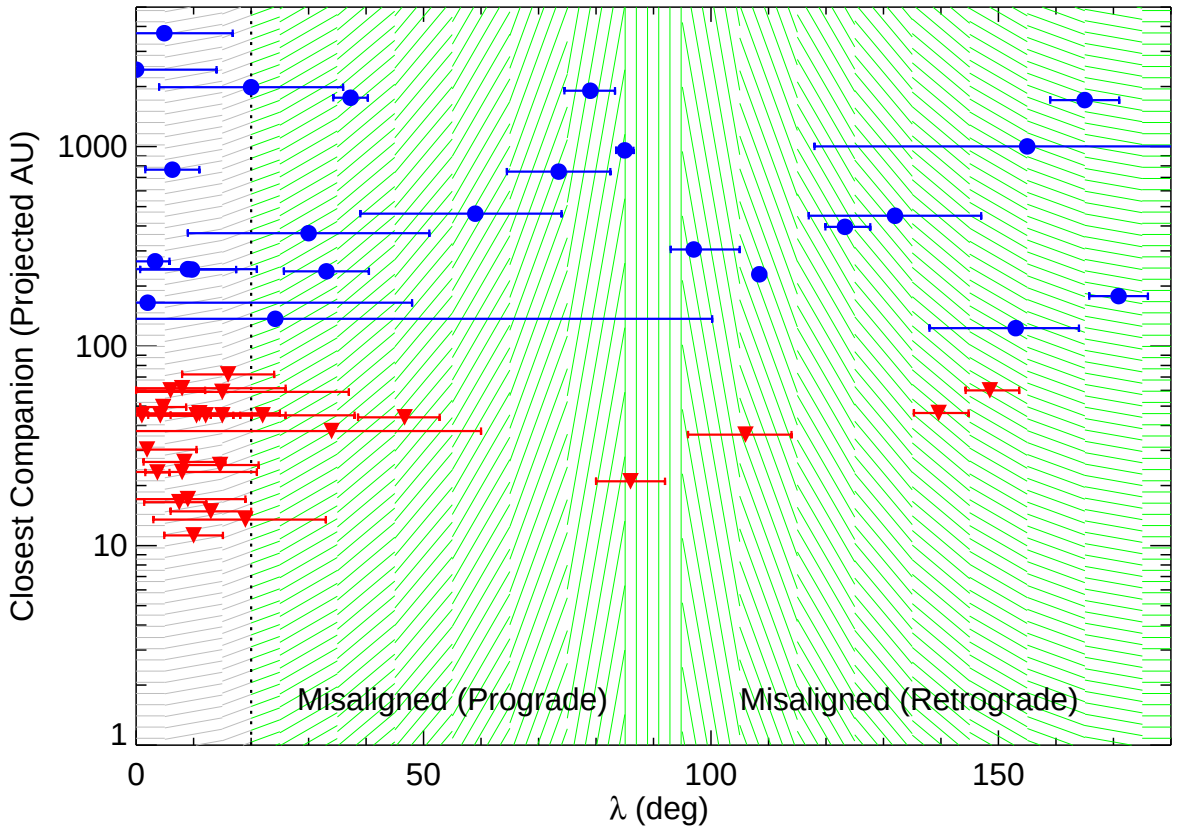

Figure 7.2 The closest stellar companion detected in our AO survey versus sky-projected spin-orbit angle. Blue circles are detected companions, and red triangles represent rough upper limits for null detections. Interestingly, most hot Jupiters in binaries are misaligned ($\lambda > 20$ deg and $\lambda/\sigma_\lambda > 2$), and most misaligned hot Jupiters reside in binaries. This may suggest that stellar Kozai cycles influence hot Jupiter migration.

high observed correlation is not causal; for example, hot (more massive) stars are more likely to have high obliquities, and they are also more likely to have binary companions, but the two need not be related. Misalignment may come from another source like planet-planet scattering, and tidal realignment may occur for the cooler systems. Making sure there are no other trends among the sample can help eliminate such possibilities. Lastly, we acknowledge that the presence of a stellar companion has the potential to tilt the primordial

disk, so spin-orbit misalignments in binaries might not require the invocation of Kozai to be explained. Checking the other properties of the system (e.g., the eccentricity, which should not be influenced by a tilted disk, but would be inflated during Kozai migration) can help confirm this apparent influence of binary companions on hot Jupiters.

CHAPTER 8

OBLIQUITIES OF EXOPLANET HOST STARS FROM PRECISE DISTANCES AND STELLAR ANGULAR DIAMETERS

8.1 Introduction

The stellar obliquity of a planetary system (ψ, the angle between the orbital momentum vector and the stellar rotational momentum vector) is shaped by a combination of several factors, including the degree of primordial misalignment between the stellar spin and the protoplanetary disk out of which the planet forms, dynamical interactions with other planets or stars, and tidal or magnetic interaction with the host star (see review by Winn & Fabrycky 2015). The obliquity can thus potentially provide valuable observational constraints on the planetary environment at formation, the architecture of planetary systems, and the processes that most often drive changes in planetary systems.

While direct measurements of the obliquity are in practice difficult, observational techniques exist that allow for precise measurements of two different projections of the obliquity. The first of these is the projection of obliquity on the plane of the sky, commonly referred to as λ (see Figure 1 from Schlaufman 2010); this measures how azimuthally aligned the vectors are, but does not constrain the inclination along our line of sight. Techniques that enable measurements of λ include the Rossiter-McLaughlin effect (Rossiter 1924; McLaughlin 1924; Queloz et al. 2000; Winn et al. 2007), Doppler tomography (e.g., Collier Cameron et al. 2010), and planets that transit spotted stellar surfaces (e.g., Sanchis-Ojeda et al. 2011; Nutzman et al. 2011; Désert et al. 2011) or gravity-darkened stars (e.g., Barnes et al. 2011b).

In special cases, the Doppler beaming "photometric Rossiter-McLaughlin" effect has been used (Groot 2012; Shporer et al. 2012), but this is not widely applicable.

Recent use of these techniques for hot Jupiter systems provides good examples of the potential for projected obliquity measurements to place constraints on the dynamical evolution of planetary systems. One seminal result is that hot Jupiters are found with a wide range of obliquities, including orbits that are highly-inclined, polar (e.g., WASP-7b; Albrecht et al. 2012a), or even retrograde (e.g., WASP-15b; Triaud et al. 2010), which is interpreted as evidence that inward migration is often driven by multi-body interactions (rather than through the gas disk). Moreover, hot Jupiters orbiting hot stars ($\gtrsim 6250\,\mathrm{K}$) often have high obliquities, whereas cool stars ($\lesssim 6250\,\mathrm{K}$) tend to be well-aligned (e.g., Winn et al. 2010a), which suggests a difference in formation, migration, or dynamical interaction between the two groups. Following a more physical motivation, the sample can as easily be divided into stars with short and long timescales for tidal dissipation (Albrecht et al. 2012b) or stars with strong versus weak magnetic braking (Dawson 2014), perhaps indicating that all hot Jupiters initially have a range of obliquities, but cool stars are able to realign more efficiently. This dichotomy could also be explained by realignment between the star and an initially misaligned planet-forming disk (Spalding & Batygin 2015), as low-mass T-Tauri stars have much stronger magnetic fields than their high-mass counterparts.

While these observations are beginning to place helpful constraints on the dynamical interactions that are important for shaping systems of gas giant planets, relatively little is known about the orbital histories of small planets, despite their relative abundance (e.g.,

Swift et al. 2013; Fressin et al. 2013; Dressing & Charbonneau 2013; Petigura et al. 2013; Ballard & Johnson 2014; Muirhead et al. 2015). This is because the techniques that can successfully measure λ are currently extremely difficult or infeasible for small planets due to the slight flux they occult. Nevertheless, population analyses of the stars that host small planets are providing indirect evidence of typical spin-axis orientations. For example, Mazeh et al. (2015) found that the average amplitude of photometric rotational modulation of cool *Kepler* transiting planet hosts is larger than for stars with no transits. They conclude that this is the result of typically edge-on equators (well-aligned with the orbital plane) for cool hosts ($< 6000\,\mathrm{K}$), and they further show that this result extends to orbital periods of at least 50 days, which would be unexpected if alignment were due solely to tidal realignment, as has been proposed for hot Jupiters.

It is also now well known that systems of small planets tend to be mutually well-aligned (i.e., coplanar; Fabrycky et al. 2014; Fang & Margot 2012), which is suggestive of a calmer dynamical history for small planets compared to hot Jupiters—small planets inside the ice line may have predominantly experienced disk migration, or very little migration at all if many of them form in situ (e.g., Hansen & Murray 2012; Chiang & Laughlin 2013). However, measurement of the inclination of the orbital planes with respect to the star is in most cases unknown. While one would generally expect spin-orbit alignment for systems with mutual orbital alignment, the disk itself could become misaligned as a consequence of the chaotic environment of star formation (e.g., Bate et al. 2010; Thies et al. 2011; Fielding et al. 2015), or through star-disk interactions (Lai et al. 2011; Batygin & Adams 2013). Gravitational

perturbation from outer companions may also tilt orbital planes while the inner planets remain mutually coplanar. This has been proposed as the mechanism responsible for Kepler-56, a system with spin-orbit misalignment, but two coplanar (transiting) planets and an outer massive companion (Huber et al. 2013). Direct measures of the obliquities of small planets could elucidate the formation conditions and processes that drive spin-orbit misalignment for small planets.

A second projection of the obliquity—its projection onto our line of sight—is equivalent to the inclination of the stellar spin axis $i_\star$ since the presence of transits implies that $i_{\rm orb}{\sim}90\,{\rm deg}$; this measures how similar the inclinations are, but doesn't constrain their relative azimuthal orientation. The advantage to using measurements of $i_\star$ over measurements of λ is that it depends only upon the properties of the star; $i_\star$ can be measured equally well for stars that host either small or large planets.

For example, Dumusque (2014) demonstrate that a sophisticated star spot and stellar activity model can constrain $i_\star$, but this is relatively imprecise and requires significant spectroscopic follow-up. The stellar inclination can also be measured via asteroseismic modeling of the rotational splitting of oscillation modes in the stellar interior (e.g., Chaplin et al. 2013; Huber et al. 2013; Quinn et al. 2015). While this does not depend on the size of the planet, it unfortunately requires long time span, precise photometry and strong stellar oscillations; even among the *Kepler* data set, only a small fraction of main sequence stars is amenable to this technique. A classic and perhaps more robust method for estimating $i_\star$ relies on using the rotation period, $P_{\rm rot}$, the stellar radius, $R_\star$, and the projected rotational velocity, $v \sin i_\star$.

$$\sin i_\star = \frac{v \sin i_\star P_{\rm rot}}{2\pi R_\star}. \tag{8.1}$$

Sometimes called the $v \sin i_\star$ method, we refer to this as "inclination from projected rotation", or IPR, and use this initialism throughout for brevity. The main drawback to IPR is that even when precise measurements of $P_{\rm rot}$ are acquired (e.g., from the same photometry used to discover a transiting planet), only very rough constraints on $i_\star$ (several tens of degrees) have generally been possible due to significant uncertainties associated with estimates of $R_\star$ and, for slow rotators, with $v \sin i_\star$. Furthermore, because the sine function flattens near 90 deg, obliquities for well-aligned systems will be imprecise, even for high precision measurements. IPR is therefore most effective for identifying misaligned orbits. Nevertheless, the growing population of these systems is beginning to provide statistical constraints on the obliquities of hosts of both large and small exoplanets.

Schlaufman (2010) employed IPR for hot Jupiters in a statistical sense, adopting predicted values for $P_{\rm rot}$ and model-dependent radii to show agreement with emerging overall obliquity trends, and to identify anomalously slow rotators likely indicative of misalignment. Others (Hirano et al. 2012, 2014; Walkowicz & Basri 2013; Morton & Winn 2014) have applied IPR to *Kepler* systems, to interesting effect. Hirano et al. (2014) report a statistical tendency for alignment among 25 systems, and identify several that may be misaligned. Using a sample of 70 systems and a more sophisticated statistical framework, Morton & Winn (2014) characterize the obliquity distribution according to the Fisher distribution parameter κ, and find a hint that multiple-transiting systems have lower obliquities than systems with

a single transiting planet. They suggest this may be evidence that the singles are actually part of a population of "dynamically hot" multiple planet systems that have large mutual inclinations, distinct from the remarkably flat systems revealed by the presence of multiple transiting planets.

In this paper, we highlight a confluence of new observational surveys and facilities that will enable more precise measurements of $i_\star$ for large samples of nearby transiting exoplanet systems. Paramount to this is the success of proposed photometric survey satellite missions designed to identify small transiting exoplanets orbiting the nearest and brightest main sequence stars. Proposed for launch in 2017 is an ESA S-class mission, the CHaracterizing ExOPlanet Satellite (CHEOPS; Broeg et al. 2013). CHEOPS will observe $\sim$ 500 nearby stars with previously identified transiting planets via radial velocity and/or photometric measurements. It will thereby increase the total number of known nearby transiting planet systems. Also scheduled for launch in 2017 is a NASA Explorer mission, the Transiting Exoplanet Survey Satellite (TESS; Ricker et al. 2014). TESS will monitor at least $\sim$200,000 nearby main sequence stars to identify new transiting exoplanets; most exoplanet discoveries will be short period ($<$ 20 days) because of its observing strategy. Within the next decade (circa 2022-2024) ESA proposes to launch the Planetary Transits and Oscillations of stars mission (PLATO 2.0; Rauer et al. 2014). PLATO 2.0 will survey up to 1 million nearby main sequence stars with an observing strategy that will identify and characterize terrestrial planets at orbital distances that extend to the habitable zone for Sun-like stars. The observational goals and thus observing strategy of PLATO 2.0 may evolve depending upon the

discoveries of CHEOPS and TESS (Rauer et al. 2014).

Likely prior to any of these transit missions being launched, precise distances for all of these stars will be available from ESA's Gaia mission, which is currently measuring trigonometric parallaxes with a predicted precision of $\lesssim 10\,\mu$as (de Bruijne 2012; de Bruijne et al. 2015). Once combined with broad-band photometry now available for the majority of nearby stars (e.g., Stassun et al. 2014), these distances will enable much more accurate determinations of bolometric fluxes and estimated radii. The proximity of the bright stars targeted in these missions will also permit long baseline optical/infrared interferometry to directly measure the sizes of many, from which radii can very accurately be determined (e.g., von Braun et al. 2014), or from which relations that improve radius estimates can be extracted (e.g., Boyajian et al. 2014). The dramatically improved precision of these measurements of nearby stars will lead to a corresponding improvement in the efficacy of IPR and consequently, the resulting constraints on processes that shape orbital architectures.

In Section 8.2, we describe IPR using observed stellar angular diameters and distances, rather than radius estimates as has been employed previously. In Section 8.3 we define the adopted simulated stellar population, including the rotational properties of this population. We discuss appropriate observational uncertainties and simulate the observations in Section 8.4, and we present results—obliquities of individual systems and constraints on underlying obliquity distributions—in Section 8.5. Finally, we consider additional applications and offer further discussion in Sections 8.6 and 8.7.

8.2 The Method

As seen in Equation 8.1, the idea behind IPR is mathematically straightforward: the sine of the stellar inclination can be calculated by dividing the projected rotational velocity ($v \sin i_\star$) by the true rotational velocity. The latter quantity can be expressed as the circumference divided by the rotation period ($v = 2\pi R_\star / P_{\rm rot}$). If the distance ($d$) to the star is known, the radius can be expressed relative to the observable stellar angular diameter (Θ) so that in terms of direct observables, Equation 8.1 becomes

$$\sin i_\star = \frac{v \sin i_\star P_{\rm rot}}{\pi \Theta d}, \tag{8.2}$$

where π refers to the mathematical constant (as opposed to the parallax). The precision with which the sine of the stellar inclination can be determined can thus be expressed in terms of the uncertainties in these four observables:

$$\left(\frac{\sigma_{\sin i_\star}}{\sin i_\star}\right)^2 = \left(\frac{\sigma_{v \sin i_\star}}{v \sin i_\star}\right)^2 + \left(\frac{\sigma_{P_{\rm rot}}}{P_{\rm rot}}\right)^2 + \left(\frac{\sigma_\Theta}{\Theta}\right)^2 + \left(\frac{\sigma_d}{d}\right)^2 \tag{8.3}$$

For now, we leave the results in this form rather than taking the inverse sine to obtain the inclination itself, because measurement errors will, in some cases, result in an unphysical measurement of $\sin i_\star > 1$, which clearly presents problems for estimating $i_\star$. If one must report the inclination—e.g., for an individual system—this can be addressed by working with the posteriors for $\sin i_\star$ and $i_\star$ to arrive at an appropriate confidence interval (see Morton & Winn 2014, particularly the discussion of their Figure 2). For our purposes, the expected distribution of $\sin i_\star$ for various underlying obliquity distributions can be modeled as easily as that of $i_\star$, and comparisons can be made directly to the results obtained using Equation 8.2,

even though some fraction of systems will appear to have $\sin i_\star > 1$.

In this paper, we consider the application of IPR for stars that TESS is likely to survey for transiting planets. We select these stars because TESS is the first of the large surveys proposed, and both candidate input catalogs (Stassun et al. 2014) and simulated stellar and planetary populations (Sullivan et al. 2015, hereafter S15) exist for this mission. A similar analysis could be conducted for PLATO 2.0 stars once its stellar sample is better defined. We also note that because of the excellent astrometric precision of Gaia, this technique will be applicable to the stars around which *Kepler* has already found planets, despite their significantly greater typical distances. Measurement precisions will determine the utility of IPR for individual systems, whereas the power of a population analysis will depend critically on obtaining a large sample of measurements. With this in mind, we simulate results for two observationally distinct samples:

i. Stars with precisely measured angular diameters—the number of which will be set by the number of stars resolvable by current (and near-term) facilities, and is likely to be relatively small ($N \sim 10^3$); and

ii. Stars with angular diameters estimated from photometric energy distributions or color relations—the number of which will be much greater ($N \sim 10^5$) and, despite their lower precision, should be more amenable to a population analysis

The results for Case ii will also depend upon the number of stars TESS surveys. The simulated catalog of S15 contains 200,000 stars monitored with 2-minute cadence, and the authors note that a large number of planets will be found using the full-frame images (FFIs),

which will sample 95% of the sky with a 30-minute cadence (similar to that of *Kepler*). We directly consider only the short cadence sample, but discuss the potential value of the larger sample from the FFIs in § 8.7.

Through Case i, we hope to determine for which stars—and how many stars—this method can provide a well constrained measure of the obliquity, and through Case ii, we hope to understand how well the underlying obliquity distribution of small planets can be constrained via such measurements.

8.3 The Stellar Sample

8.3.1 Simulating TESS Targets

At the time of this publication, specific TESS targets have not yet been selected, but there are working catalogs (e.g., Stassun et al. 2014), from which at least two hundred thousand dwarf stars will ultimately be selected, and a simulated target sample and expected planetary population described by S15. We adopt the careful simulations of S15, which employ the TRILEGAL model of the galaxy (Girardi et al. 2005) to generate the stellar population, with slight modifications (e.g., to improve the agreement of the simulated stellar radii with observations). Using this input stellar catalog, the known frequency of exoplanets, and the expected instrumental and survey characteristics of TESS, and a target selection process based on planet detectability criteria, S15 then simulate the stars around which TESS will detect planets and the types of planets it will detect; they report one such planet catalog in their Table 6. We used 10 realizations of the simulated TESS planet catalog provided to us by P. Sullivan to run the obliquity simulations described below. One realization contains an average of 1860 simulated planet hosts, and almost all are main sequence stars. While the stars span spectral types B6 to M9, there are relatively few early type hosts—86% are later- type than G0 ($T_{\rm eff} < 5920\,{\rm K}$), and 57% are M dwarfs ($T_{\rm eff} < 3850\,{\rm K}$). Figure 8.1 and Figure 8.2 illustrate some relevant properties of the planet hosts, but for a more detailed description of the stellar and planetary samples, please refer to S15.

We also point out that while S15 treated stellar multiplicity with care to ensure realistic TESS planet yields, we do not explicitly include the effects of multiplicity in our calculations

in the following sections. The primary effect is likely to be a small bias in some systems when fitting the photometric energy distribution to estimate radii, but we adopt conservative errors to mitigate this.

8.3.2 Calculating the Observable Quantities

The stellar properties provided by S15 include the distance modulus, $R_\star$, $T_{\rm eff}$, and absolute V magnitude, which we can use to derive the observable quantities from Equation 8.2. We first trivially calculate d from the distance modulus and Θ from $R_\star$ and d.

Next, we use the gyrochronological relation from Mamajek & Hillenbrand (2008) to calculate rotation periods (in days) from photometric colors and stellar ages (in Myr):

$$P_{\rm rot} = 0.407\,[(B-V) - 0.495]^{0.325}\,t^{0.566} \tag{8.4}$$

For this, we need the B magnitudes, which we derive using the $T_{\rm eff}$–color table presented by E. Mamajek[1] and Pecaut & Mamajek (2013). There is significant uncertainty in the four constants in Equation 8.4 (because real stars display a scatter about this relation), so we draw a new set of the four constants for each star, using the errors on these constants reported by the authors. This produces a stellar sample with a realistic scatter of rotation periods about the gyrochronological relation. We further note that the sample includes a handful of early type stars and a large number of M dwarfs, but the above relation is only calibrated for $0.5 \lesssim (B-V) \lesssim 0.9$ (F7-K2). Mamajek & Hillenbrand (2008) note that F3V-F6V spectral types appear to be where gyrochronology fails due to the thinning of convective envelopes

[1] `http://www.pas.rochester.edu/~emamajek/EEM_dwarf_UBVIJHK_colors_Teff.txt`

and the loss of magnetic dynamos, thus preventing the magnetic braking from which spin-down laws emerge. These earlier types should therefore spin faster than their slightly less massive counterparts. As an approximation, we assign rotation periods for earlier types by assuming $(B - V) = 0.5$, which may slightly overestimate the rotation periods for the hottest stars. For late type dwarfs with $(B - V) > 0.9$, we simply apply Equation 8.4 and acknowledge that these less massive, and in some cases fully convective, stars probably obey a somewhat different spin-down law. We argue that this is unlikely to significantly bias our results. Qualitatively, cooler stars will spin more slowly, so the declining rotation period relation should be correct to first order. Moreover, some very late-type stars are expected to have significant rotation—the predictable, monotonic spin-down seen in solar-type stars gives way to a bimodality for later types that includes both fast and slow rotators (e.g., Irwin et al. 2011; McQuillan et al. 2014). In all cases, by erring toward overestimated rotation periods, we will also overestimate uncertainties for $P_{\rm rot}$ and $v \sin i_\star$, thereby obtaining conservative results.

A further complication in simulating $P_{\rm rot}$ is that measured rotation periods (including those used to derive gyrochronology relations) track the rotational velocity at the active spot latitudes rather than at the equator—the rotation periods we assigned are therefore the periods at the active latitudes. We can assign *equatorial* rotation periods by assuming a differential rotation law and spot latitude distribution. Following the approach of Hirano et al. (2014) and Morton & Winn (2014), we adopt the functional form for differential

rotation from Collier Cameron (2007):

$$P_{\rm rot}(\ell) = \frac{P_{\rm rot,eq}}{1 - \alpha \sin^2 \ell}, \tag{8.5}$$

and we draw spot latitudes from a distribution $\ell = 20 \pm 20\,\deg$, and assume the strength of differential rotation is similar to the Sun ($\alpha = 0.23$).

Hirano et al. (2014) showed that differential rotation will similarly result in a measured $v \sin i_\star$ that is too large by a factor $\sim(1 - \alpha/2)^{-1}$. While applying this correction to observations of real systems has the potential to introduce a small error if the true strength of differential rotation is significantly different from the assumed solar value of $\alpha = 0.23$, in our simulations the true and observed values would both receive the same correction, so we ignore this small factor.

With the equatorial $P_{\rm rot}$ and $R_\star$ in hand, we can generate $v \sin i_\star$ by drawing $i_\star$ from an appropriate distribution. We note that an isotropic distribution is most likely not the correct choice for this distribution—our hypothetical planets all transit, so if ψ is preferentially low (well-aligned), then $i_\star$ must be preferentially high (edge-on rotation). We explore the effect of different obliquity distributions in Section 8.5.

8.4 Assigning Uncertainties and Simulating Observations

8.4.1 Distance Uncertainty

The most uniform and complete set of distances currently available for nearby Sun-like stars ($< 100\,\mathrm{pc}$) comes from the Hipparcos mission (ESA 1997). van Leeuwen (2007) quote a mean parallax precision for single stars of 0.33 mas for $H_P < 7\,\mathrm{mag}$, and 0.56 mas for $H_P < 9\,\mathrm{mag}$, which corresponds to distance precisions of $\sim$1% for Sun-like stars at 30 pc, and $\sim$4% for those at 75 pc. For many of the fainter TESS targets, this uncertainty easily becomes the dominant term in the error budget of Equation 8.3. Fortunately, the Gaia mission (Perryman et al. 2001) promises to improve upon this considerably, by providing parallax measurements to roughly 1 billion stars; first estimates of these distances are expected to be available prior to the launch of TESS. de Bruijne (2012) quoted an anticipated precision of better than 10 μas for $G < 12\,\mathrm{mag}$ stars— corresponding to a distance precision better than 0.1% at 100 pc and better than 1% at 1 kpc—although faint stars and some very close visual binaries may carry additional measurement errors. Evaluation of in-orbit commissioning data suggests that despite some minor operational hiccups (e.g., significant stray light levels, larger than expected instability between the basic angle between the lines of sight of the two telescopes) the astrometric performance will remain within the 20% science margin set before launch; the updated performance predictions given by de Bruijne et al. (2015)[2] suggest that the majority of the TESS stars will carry a parallax error smaller than $\sim$15 μas. We approximate distance errors by propagating a constant 15 μas uncertainty in parallax, $\sigma_d = 15 \times 10^{-6} d^2$ pc.

[2]See also a summary on the mission website: `http://www.cosmos.esa.int/web/gaia/science-performance`.

8.4.2 Stellar Angular Diameters: Available Populations and Uncertainties

Stellar angular diameters can either be measured directly from interferometric measurements or estimated from bolometric fluxes and effective temperatures: $\Theta^2 = 4F_{\rm bol}/(\sigma T_{\rm eff}^4)$. Since the directly measured values translate to stellar inclinations with the smallest uncertainties, we consider this population first. For a star to be spatially resolved, it must be both bright enough for precise measurements and larger than the resolution limit. Currently the world's longest baseline interferometer operating at optical and infrared wavelengths, where photospheres are the brightest, is Georgia State University's CHARA Array, located on Mt. Wilson in California (ten Brummelaar et al. 2005). With a long baseline of 331 m, the Array yields an angular resolution ($\lambda/2B$) of 0.51 mas in the H band and 0.24 mas in the R band; an adaptive optics system is currently being installed that is predicted to achieve limiting magnitudes of 9.0 at H and 10.0 at R (ten Brummelaar et al. 2012, 2014); current limiting magnitudes for precision measurements are 7.0 and 7.0, respectively.

To determine the number of stars that the CHARA Array is likely to spatially resolve, we adopt the R band adaptive optics limits of $\theta_{\rm res} = 0.24$ mas and $R_{\rm lim} = 10.0$ mag, and assume a declination limit of $\delta > -30$ deg. These limits are applied to the 10 realizations of the TESS simulated planetary population, and yield a mean of 14.8 TESS transiting planet hosts resolvable by CHARA. This subset of stars is illustrated in Figure 8.1. We note that for all but the very latest types, the primary limitation is their small angular sizes, rather than their faint R magnitudes; relative to the CHARA limits, the typical TESS planet host is small but not necessarily faint. The brightness of these stars will enable high S/N observations

that are important for achieving precise size measurements, and their small sizes are not an insurmountable obstacle; Huber et al. (2012), for example, obtained angular diameters to within 2% for several bright stars close to (and even beyond) the nominal resolution limit using a modest number of observations. It thus seems plausible that the majority of these stars that are large enough and bright enough for CHARA to resolve and could have their sizes measured with similar precisions. We therefore adopt a 2% uncertainty in directly measured angular diameters.

Since the subsample that can be spatially resolved with CHARA represents only a small fraction of the expected TESS planet hosts, we also consider the precision with which radii can be estimated. Boyajian et al. (2014) demonstrate that angular diameters can be predicted with a precision of 5% from single color relations and an absolute magnitude, based on the dispersions about the best fit relation for nearby stars with interferometrically measured radii and Hipparcos distances. However, applying these relations blindly to TESS targets will likely yield biased results since the sample extends to distances of $\sim$500 pc (see Figure 8.1) and many stars likely experience modest extinction. There are two promising methods to account and correct for this. First, the precise distances that Gaia will provide, coupled with spectroscopically determined temperatures, will yield all sky extinction maps (Schultheis et al. 2015) and enable first order corrections. And for planet hosts with a spectroscopically determined temperature, their observed photometric energy distribution can be compared to that expected for their temperature to derive their line-of-sight extinction. Thus, with very accurate Gaia distances and extinction corrections, photometric energy dis-

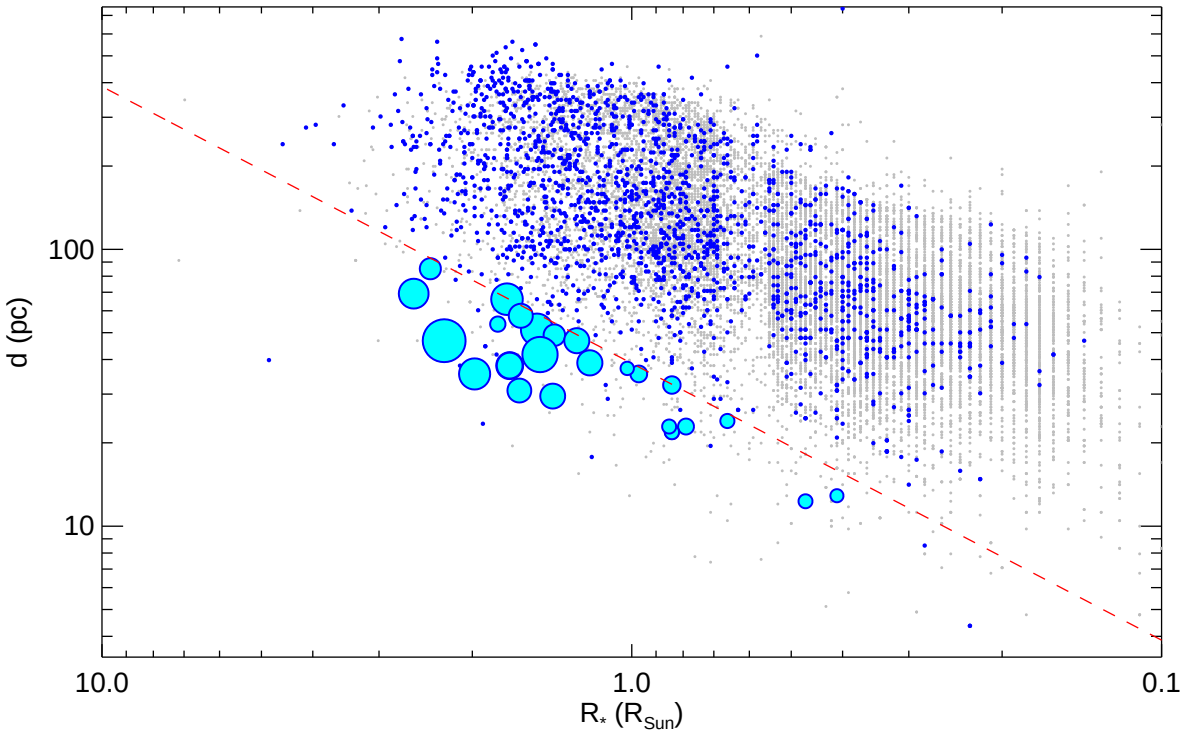

Figure 8.1 Distance as a function of stellar radius for the sample of planet hosts. All 10 realizations are plotted here (gray dots). The CHARA R-band resolution limit (0.24 mas) is indicated with a red dashed line. Stars that are resolvable lie below this line. Blue dots indicate stars with measured $\sin i_\star$—i.e., those that pass our observational cuts in $v \sin i_\star$ and $P_{\rm rot}$ and have detectable photometric rotational modulation, as described in Section 8.5.1. Large cyan circles represent those stars that also pass the resolution, magnitude ($R < 10$), and declination ($\delta > -30\,{\rm deg}$) limits of the CHARA array—i.e., the subset with measured $\sin i_\star$ from directly measured diameters (Case i). The sizes of the circles are scaled logarithmically by their projected rotational velocities, which range from 2 to $\sim$120 $\rm km\,s^{-1}$.

tributions (as opposed to single color relations) can be used to get accurate bolometric fluxes. When combined with spectroscopically determined temperatures, these will yield accurate angular diameters via the Stefan–Boltzmann Law—$\Theta \propto (F_{\rm bol})^{0.5}\,(T_{\rm eff})^{-2}$. We adopt a conservative 5% uncertainty in estimated angular diameters, since that precision has already been demonstrated using single colors, but we expect that it should be possible to do better

using the full photometric energy distribution.

8.4.3 Rotation Period Uncertainty

The photometric precision and high cadence observations ($\sim$2 min) of TESS will enable the detection of a large number of stellar rotation periods. For example, McQuillan et al. (2014) report 34,000 rotation periods among the *Kepler* sample, corresponding to a recovery rate of $\sim$25% for cool ($< 6500\,\mathrm{K}$) dwarfs without eclipsing binary companions.

The TESS and *Kepler* dwarf samples will differ in several ways, and while we discuss these differences below, we ultimately argue that adopting detection rates from the *Kepler* sample is justified in our simulations. One important difference between data sets will be the typical timespan of observations for TESS stars. In general, they will not have the luxury of the long-term monitoring that *Kepler* provided—most TESS stars will be monitored for only 27 days (one spacecraft pointing), though near the ecliptic poles, field overlap will allow $\sim$1 year of continuous monitoring. We therefore expect that precise rotation periods will only be determined for $P_{\mathrm{rot}} < 14$ days, and remove slower rotators from our simulations. This observational constraint is likely to limit TESS detection of rotation periods mainly to stars younger or earlier-type than the Sun (i.e., rotating faster than $P_{\mathrm{rot},\odot}\sim$26 days), and may hinder detections for slowly-rotating late-type stars. However, in the context of *Kepler* rotation periods, the former limitation may not be important, as McQuillan et al. (2014) suggest that very few rotation periods of stars older than the Sun were detected. Similarly, in the context of Case i (interferometrically determined Θ), relatively few late type stars will be resolvable because of their small sizes and faint magnitudes; reduced sensitivity to rotation

periods of late-type stars will have relatively little effect on the overall results. For Case ii (photometrically determined Θ), TESS might only observe a fraction of a rotation period for many cool, slow rotators, which could hinder the application of IPR. However, the typical amplitudes of variation are large enough ($\sim$1 to 22 mmag in the $5^{\rm th}$ to $95^{\rm th}$ percentile) that ground-based follow-up should in most cases be capable of determining the rotation periods. This would not be ideal, but is not an insurmountable obstacle.

Because TESS will observe the brightest stars in the sky, it is worth comparing TESS and *Kepler* photon noise. TESS targets will typically be 30 to 100 times brighter than *Kepler* targets. However, the TESS aperture has an area 100 times smaller than *Kepler* and photon noise will therefore generally be comparable to or greater than for *Kepler*. *Kepler*'s longer duration is also an asset to beat down noise, and the results will ultimately depend on the photometric precision TESS is able to achieve. The brightness of TESS targets will at least better enable ground-based follow-up, e.g., to determine rotation periods of stars for which TESS only observes a fraction of a rotation period.

We assume that the fractional uncertainties in the measured $P_{\rm rot}$ reported by McQuillan et al. (2014) are roughly indicative of the precisions one can expect from TESS, at least for periods short enough to be determined reliably. Among 34,000 main sequence *Kepler* stars for which McQuillan et al. (2014) detect rotation periods, the highest probability density (and 1σ error) of the fractional period uncertainty is $0.29\%^{+1.51\%}_{-0.29\%}$; the period uncertainty is on average dependent upon the rotation period itself. To account for this, we assign uncertainties as a function of rotation period using the McQuillan et al. (2014) catalog.

For each bin in $P_{\rm rot}$, we calculate the probability density function (PDF) of the fractional uncertainty using a kernel density estimator. For each star in that bin, we then draw a fractional uncertainty according to the PDF, which is trivially converted to an absolute uncertainty, $\sigma_{P_{\rm rot}}$. One complication is that the observed rotation period is actually the period at the active spot latitude rather than equatorial rotation. To account for this we first simulate the observed rotation period, $\hat{P}_{\rm rot}(\ell) = P_{\rm rot}(\ell) + x\sigma_{P_{\rm rot}}$, and then assume $\ell = 20\,{\rm deg}$ in order to estimate the correction needed to determine the equatorial rotation period: $\hat{P}_{\rm rot} = \hat{P}_{\rm rot}(\ell)(1 - \alpha \sin^2(20\,{\rm deg})) = 0.973\hat{P}_{\rm rot}(\ell)$. The cumulative effect of having to estimate the active spot latitude correction is typically an additional error in the equatorial rotation period of $\sim$2.5% (stemming from the uncertainty in ℓ) that is not included explicitly in the measurement errors for the observed rotation period.

8.4.4 Projected Rotational Velocity Uncertainty

The projected (equatorial) rotational velocities, $v \sin i_\star$, can be obtained from high resolution spectroscopy. Unlike $T_{\rm eff}$, $\log g$, and [Fe/H], $v \sin i_\star$ is mostly free from degeneracy with the other parameters. For stars rotating sufficiently fast such that rotation is the dominant broadening mechanism ($v \sin i_\star \gtrsim 10$), $v \sin i_\star$ can typically be determined to a few percent with high signal to noise ratio, high dispersion spectra (e.g., Siverd et al. 2012; Bieryla et al. 2015). However, for more slowly rotating stars, complicating effects such as the assumed macroturbulent velocities of convective cells ($v_{\rm mac}$) can directly affect the predicted spectral line profiles. For example, the difference in derived $v \sin i_\star$ if one assumes $v_{\rm mac}$ values of 2 and $3\,{\rm km\,s^{-1}}$ is $\sim$$0.25\,{\rm km\,s^{-1}}$, or 2.5% for a star with $10\,{\rm km\,s^{-1}}$ total line broadening.

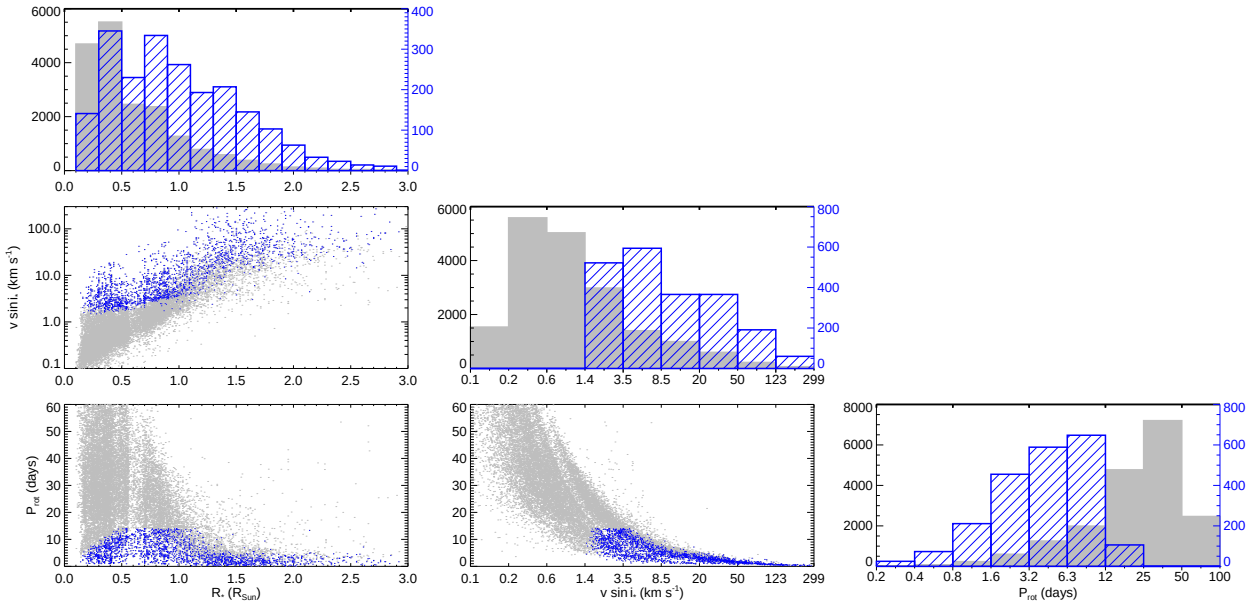

Figure 8.2 Comparison between the full sample of TESS planet hosts (gray) and the sample for which we expect $\sin i_\star$ measurements (blue). We show correlation plots and histograms for $R_\star$, $v \sin i_\star$, and $P_{\rm rot}$. The right (blue) axes in the histograms correspond to the measured $\sin i_\star$ sample, plotted as blue hatched histograms. All 10 realizations of the planet simulations are plotted, and we have assumed $f_{\rm al} = 0.7$ to generate the plotted $v \sin i_\star$ sample. It is clear that the smallest stars (slowest rotators) are most stongly affected by our observational cuts of $v \sin i_\star > 2$ and $P_{\rm rot} < 14$.

There is hope that observationally calibrated relationships between $T_{\rm eff}$, $\log g$, and $v_{\rm mac}$ (e.g., the asteroseismically-calibrated relationship presented by Doyle et al. 2014) can be used to constrain $v_{\rm mac}$ and mitigate such a bias. In practice, however, even with perfect knowledge of $v_{\rm mac}$, current typical $v \sin i_\star$ uncertainties for stars with $v \sin i_\star < 10\,{\rm km\,s^{-1}}$ are $0.2 - 0.3\,{\rm km\,s^{-1}}$, and thus approach a 10% uncertainty for stars with $v \sin i_\star$ values of only a few ${\rm km\,s^{-1}}$ (e.g. Gray 2013; Tsantaki et al. 2014). We note that some more sophisticated analysis techniques may improve the precision several fold (Gray & Baliunas 1997) if measuring $v \sin i_\star$, as opposed to simply accounting for it in a stellar model, were the goal. Finally, measurement of $v \sin i_\star$ values that are less than the instrumental resolution

are possible, but become even more challenging. The HARPS-N spectrograph (Cosentino et al. 2012), for example, has a resolving power of $R{\sim}115{,}000$, corresponding to a resolution element of $2.6\,\mathrm{km\,s^{-1}}$; if $v \sin i_\star$ is much slower than this, then it is only a minor contributor to the total line broadening. Large fractional changes in $v \sin i_\star$ therefore have relatively little effect on the line profiles and cannot be measured precisely. In these cases it is best to assign an upper limit on the $v \sin i_\star$ value, although a proper choice for this limit, relative to the instrumental resolution, is also data quality dependent.

Given the above considerations, we adopt the following uncertainties for $v \sin i_\star$, assuming observations are made with a very high-resolution spectrograph ($R \gtrsim 100,000$) and are subjected to a careful analysis. For stars with $v \sin i_\star \geq 10\,\mathrm{km\,s^{-1}}$, we assume an uncertainty of 2.5%. For stars with $10\,\mathrm{km\,s^{-1}} \geq v \sin i_\star \geq 2\,\mathrm{km\,s^{-1}}$, we assume a constant uncertainty of $0.25\,\mathrm{km\,s^{-1}}$, which corresponds to an uncertainty of 2.5% at $10\,\mathrm{km\,s^{-1}}$ and 12.5% at $2\,\mathrm{km\,s^{-1}}$. For stars with $v \sin i_\star < 2\,\mathrm{km\,s^{-1}}$, we assume that only an upper limit can be inferred, and we remove these stars from our sample.

8.4.5 Simulating Measured Quantities

To determine which, and how many, systems will be amenable to projected obliquity measurements via IPR, we simulate observations of each star in our sample to arrive at simulated observed values of $\sin i_\star$. This simulated observed distribution has two uses. First, it can be populated with transiting planets according to realistic occurrence rates in order to calculate the likely yield of projected obliquities (and their distribution and uncertainties). Second, by running this simulation many times, we can build well-sampled, expected distributions of ob-

served $\sin i_\star$ values under various assumptions (number and characteristics of survey targets, observational uncertainties and limits, etc.). These distributions can be used as comparison samples against which we can compare our observed distributions (e.g., in a Kolmogorov–Smirnov test). This will therefore allow us to test observed distributions against arbitrary underlying obliquity distributions.

We first point out that measurement precision as a function of stellar properties is somewhat nuanced, as the precision of several of the observables is expected to have a dependence on other stellar properties. We therefore must be careful when simulating observed quantities and their measurement uncertainties. Very generally, given the observable quantities $p = \{d, \Theta, P_{\rm rot}, v \sin i_\star\}$ with true values p_i as calculated in Section 8.3, we need to assign for each star in our sample the observed values, $\hat{p}_i$, and uncertainties, σ_{p_i}. Under the assumption of uncorrelated Gaussian errors, these quantities can be related simply by:

$$\hat{p}_i = p_i + x\sigma_{p_i}, \tag{8.6}$$

where x is drawn from a normal distribution, $x \sim \mathcal{N}(0, 1)$.

Using the above relation we can simulate measured quantities for d, Θ, and $P_{\rm rot}$. Simulating measurements of $v \sin i_\star$, however, requires assigning a distribution of $i_\star$ values, which are unlikely to be random for stars that host transiting planets. For example, if most planets are coplanar with the stellar equator, then for a sample of transiting planets, the underlying inclination distribution should be confined to near-90 deg orientations. However, if all systems experience significant evolution of their angular momenta, an isotropic distribution might be more appropriate. The true distribution may contain a mix of systems: well-aligned systems

that have formed in an equatorial disk and experienced calm migration (or no migration at all), plus a more isotropic distribution caused by interaction of the planets or proto-planetary disk with a binary or additional planetary companions. For Case i (interferometric Θ), we do not expect a large number of systems (or a powerful population analysis), and we thus confine our investigation to two simple inclination distributions: isotropic, in which the probability of observing a particular inclination is given by $P(i_\star) \sim \cos i_\star$; and well-aligned, which we characterize as an isotropic distribution truncated to within 10 deg of alignment. For Case ii (photometric Θ), we expect many more systems, and therefore anticipate that we will be able to distinguish much more finely between underlying distributions. We therefore simulate many "mixed" distributions, comprised of varying fractions of the above isotropic and aligned distributions. We refer to these mixed distributions by the fraction of aligned systems—for a mixed distribution with $f_{\rm al} = 0.7$, 70% of systems are drawn from an aligned distribution and 30% of systems are drawn from an isotropic distribution. Regardless of the distribution from which $i_\star$ is drawn, our observed projected rotational velocities are simply given by $\hat{v}\sin i_\star = v \sin i_\star + x\sigma_{v \sin i_\star}$ (with $\sigma_{v \sin i_\star}$ chosen as outlined in Section 8.4.4).

For a given distribution of $i_\star$ values, all 4 measured quantities can be simulated and the uncertainty in $\sin i_\star$ can be determined from formal error propagation.

8.4.6 Resulting Uncertainty on the Stellar Inclination

As described in more detail above, a typical spatially resolvable star might have errors of $\sigma_{P_{\rm rot}} \sim 1\%$, $\sigma_\theta \sim 2\%$, and $\sigma_d \sim 0.1\%$, with an additional $\sim 2.5\%$ uncertainty in $\sigma_{P_{\rm rot}}$ introduced by correcting for differential rotation. The fractional error on $v \sin i_\star$ depends on $v \sin i_\star$

itself; for the example of a star rotating at $5 \pm 0.25\,\mathrm{km\,s^{-1}}$ ($\sigma_{v \sin i_\star} \sim 5\%$), this combination of uncertainties leads to $\sigma_{\sin i_\star} \sim 6\%$. The corresponding constraint on $i_\star$ would depend on the inclination: for nearly edge-on rotation ($\sin i_\star \sim 1$), one would derive an uncertainty in $i_\star$ of $\sim 20\,\mathrm{deg}$, but for lower stellar inclinations, the uncertainty may be only a few degrees. Thus, individual well-aligned systems will still be difficult to identify with confidence—especially around slow rotators for which the $v \sin i_\star$ fractional uncertainty is large—but misaligned systems should result in highly significant detections and precise measurements. Despite this difficulty for some individual systems, the *population* of $\sin i_\star$ measurements should be able to constrain the underlying obliquity distribution, and the smaller uncertainties resulting from IPR using precise distances and angular diameters should reduce the number of measurements required to do so.

8.5 Results

8.5.1 Expected Number of Obliquity Measurements

The above discussion quantifies how well the stellar inclination can be determined in any one case, and the simulated stellar population allows us to estimate the number of transiting systems for which these projected obliquity measurements can be realized. This number can be estimated by multiplying the initial number of targets successively by the fraction that hosts planets, the fraction for which a transit is detected, and the fraction that has detectable rotational modulation and rotational line broadening:

$$N_{\mathrm{ob}} = N_\star \times f_{\mathrm{pl}} \times p_{\mathrm{tr}} \times f_{\mathrm{rot}}. \tag{8.7}$$

By using their simulated TESS planet catalog, we have implicitly adopted the first three terms from S15; briefly, they assume $N_\star = 200{,}000$ and assign planet occurrence rates ($f_{\rm pl} \times p_{\rm tr}$) as a function of stellar properties and orbital period using the *Kepler* planet occurrence statistics reported by Fressin et al. (2013) and Dressing & Charbonneau (2013, 2015). Given the mean number of planets from 10 realizations of the S15 simulations, Equation 8.7 becomes $N_{\rm ob} = 1863 \times f_{\rm rot}$.

Not all stars are active enough to reveal their rotation periods, and activity level varies as a function of spectral type, so we cannot adopt a single value for $f_{\rm rot}$ in our simulations. Additionally, our fiducial simulation makes the assumption that $v \sin i_\star$ cannot be measured below $2\,{\rm km\,s^{-1}}$ and that rotation periods longer than 14 days will not be identified by TESS, so systems that do not satisfy these criteria will be removed, even if the photometric amplitude of rotational modulation is expected to be detectable. To assess detectability of rotational modulation, we first assume that TESS will recover rotation periods at the same rate as *Kepler*. (While the 4-year light curves of *Kepler* should offer an advantage in $P_{\rm rot}$ precision compared to TESS, the *detection* of variability should be generally similar since the amplitudes of variation are in general much larger than the photometric uncertainties.) McQuillan et al. (2014) detected rotation in 83% of cool stars ($< 4000\,{\rm K}$), but in only $\sim$20% of stars hotter than the Sun. To enforce this condition, we divide our sample into bins of 100 K in $T_{\rm eff}$ and then flag stars as detectable with probability according to the PDF of the McQuillan et al. (2014) rotation periods in that $T_{\rm eff}$ bin, normalized to the detection rate for that $T_{\rm eff}$. In this way, our final distributions of rotation periods and detection rates as

a function of $T_{\rm eff}$ broadly match the *Kepler* sample before we apply our observational cuts of $P_{\rm rot} < 14\,{\rm days}$ and $v \sin i_\star > 2\,{\rm km\,s^{-1}}$. Finally, we note that the fraction of transiting planet hosts stars with $v \sin i_\star > 2\,{\rm km\,s^{-1}}$ depends upon the underlying obliquity distribution: well-aligned systems will have larger $v \sin i_\star$ on average. This effect is seen in the results of our simulations. After assessing $P_{\rm rot}$ detectability and applying the observational cuts, we estimate $N_{\rm ob}{\sim}189$ for an isotropic distribution of obliquities and $N_{\rm ob}{\sim}214$ for a well-aligned distribution.

We compare the properties of the full planet host sample to those of the "measured $\sin i_\star$" sample in Figure 8.2. One can clearly see the primary result of the observational limits we have imposed: the excluded slow rotators tend to be the smallest stars, so the "measured $\sin i_\star$" sample is biased toward larger (more massive) stars than the full planet host sample. Furthermore, the M dwarfs for which $\sin i_\star$ *will* be measured belong to the rapidly rotating subset of M dwarfs, which may indicate comparative youth or perhaps more fundamental differences. The properties of planetary systems orbiting these stars may therefore not be representative of all M dwarf planets. This will be important to keep in mind when interpreting results. This also highlights an opportunity – the extension of observational limits to smaller $v \sin i_\star$ and larger $P_{\rm rot}$ through improved techniques and follow-up observations will provide a larger *and more representative* population for this analysis. We discuss this opportunity further in Section 8.6.

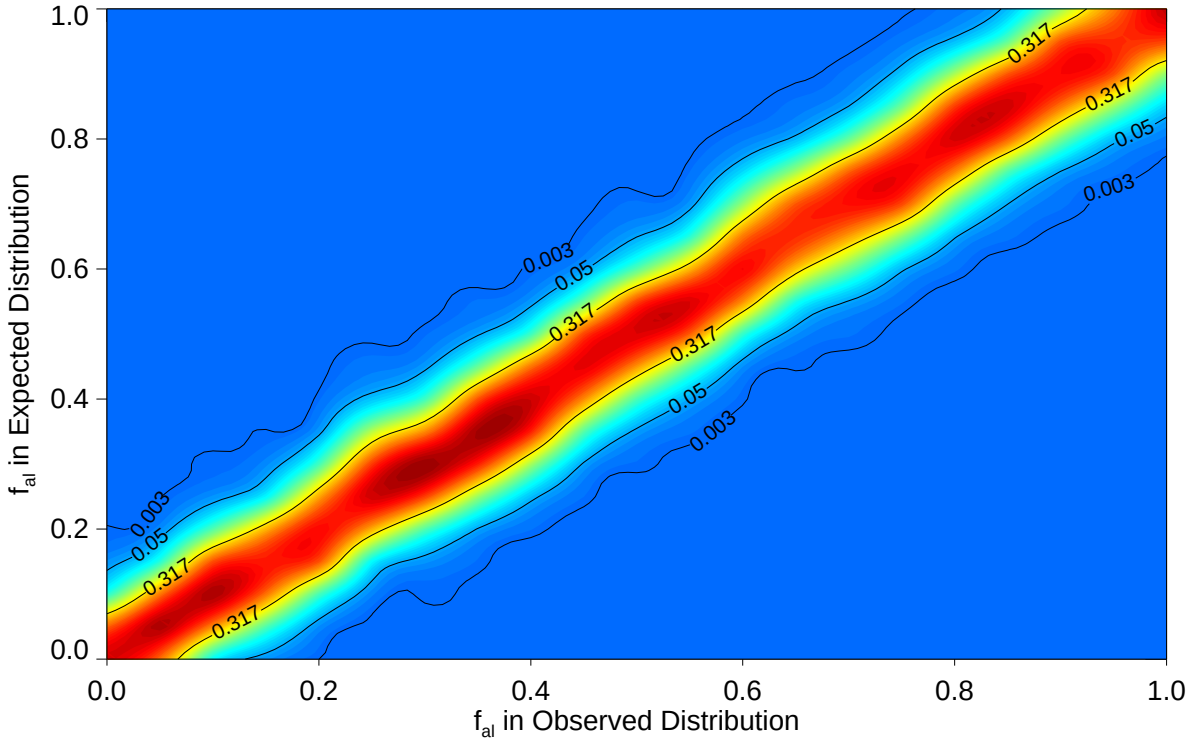

Figure 8.3 KS test p-values (colored contours) for observed and expected $\sin i_\star$ distributions comprised of $f_{\rm al}$ well-aligned systems (and $1 - f_{\rm al}$ randomly oriented systems). Low p-values (blue regions) correspond to pairs of expected and observed distributions that are unlikely to arise from the same parent distribution. The most likely true fraction of aligned systems is that for which the expected distribution produces the largest p-value (red regions), and the distance over which the p-values decline characterizes the precision with which the true aligned fraction can be measured. For each observed distribution, we adopt the region with $p > 0.05$ (red to cyan) as the uncertainty on $f_{\rm al}$ for the true underlying distribution. The results are summarized numerically in Table 8.1.

8.5.2 Constraints on the Underlying Obliquity Distribution from Interferometric Measurements

The discussion in Section 8.5.1 considers the large sample of Case ii (photometrically derived angular diameters), but the (small) number of CHARA-resolvable TESS planet hosts can also be determined directly from the distances and radii provided by the S15 simulations. A mean of 14.8 resolvable planet hosts are expected, but only 2.2 (isotropic distribution) or 2.5

(aligned distribution) are expected to have $v \sin i_\star > 2\,\mathrm{km\,s^{-1}}$ and a detected $P_{\mathrm{rot}} < 14\,\mathrm{days}$.

A handful of projected obliquity measurements is not sufficient for a population analysis, but this group of planetary systems is likely to be well-studied, since uncertainties in stellar properties are most often the strongest limitation on our understanding of the properties of transiting planets, and the precision afforded by directly measured radii allow greater insights into processes governing the structure and evolution of both stars and planets (e.g., Boyajian et al. 2015). It is therefore plausible that through careful follow-up observations, another handful of these $\sim$15 systems will have rotation periods and rotational velocities measured, even beyond the 14 day and $2\,\mathrm{km\,s^{-1}}$ limits assumed above. In any case, for a strong constraint on the underlying obliquity distribution, we must turn to the larger sample of photometrically derived angular diameters.

8.5.3 Constraints on the Underlying Obliquity Distribution from Photometric Measurements

Determining Θ from the photometric energy distribution or color relations will be harder to apply to individual systems because of its less precise measurements, but it holds greater promise as a means to probe the population as a whole because we expect hundreds of systems to be amenable to this technique. We describe here one methodology that can be used to characterize the true obliquity distribution and demonstrate it using our simulated observations of TESS planet hosts.

Given an underlying obliquity distribution, one may simulate a stellar and planetary population and a set of observations of those systems in order to construct the distribution

of $\sin i_\star$ values that one expects to recover through observation. We refer to this as the "expected distribution". It is a distribution corresponding to the true underlying distribution once it has been subjected to our observational constraints (i.e., $v \sin i_\star > 2\,\mathrm{km\,s^{-1}}$, $P_{\rm rot} < 14\,\mathrm{days}$) and measurement errors. This expected distribution can then be used as a comparison against the $\sin i_\star$ distribution that arises from observations of TESS systems—the "observed distribution". (Since TESS has not yet launched, we also simulate the observed distribution here, of course.) To constrain the true underlying distribution, we run a series of Kolmogorov-Smirnov (KS) tests to characterize the similarity between the observed distribution (for a given value of $f_{\rm al}$) and many expected distributions (for many different values of $f_{\rm al}$). For pairs with $p < 0.05$ ($< 5\%$ chance that the same parent distribution would produce both the observed and expected distributions), we consider the distributions inconsistent. For a given observed distribution, we report the best fit as the expected distribution with the largest p-value and assign errors to encompass the expected distributions that produced $p > 0.05$. Figure 8.3 illustrates this comparison for our fiducial simulations and a range of underlying obliquity distributions. The results are summarized in Table 8.1. It can be seen clearly that the best fit distribution does indeed accurately recover the distribution from which our systems were drawn.

One advantage of the technique outlined herein is that by simulating the stellar sample, the observations, and ultimately the expected distribution, the observed distribution can be tested against any model distribution, and the expected distribution captures the observational biases that would not be accounted for in a direct fit to an assumed functional form for

the true distribution. In practice, it makes sense to test physically motivated distributions—such as our examples that have been parametrized to include $f_{\rm al}$ aligned systems and $1 - f_{\rm al}$ isotropic systems, or the Fisher distribution favored by Morton & Winn (2014)—but the model distributions need not be parametric, and the use of the KS test to reject model distributions allows a fully non-parametric analysis. One could, for example, directly use the results of arbitrarily complex dynamical evolution models as the comparison distributions.

Table 8.1: The Underlying Obliquity Distribution

$f_{\rm al}$ drawn	$f_{\rm al}$ derived
0%	0^{+14}_{-0}%
10%	10^{+15}_{-10}%
20%	20^{+15}_{-14}%
30%	30^{+15}_{-14}%
40%	40^{+14}_{-16}%
50%	50^{+15}_{-15}%
60%	60^{+16}_{-14}%
70%	70^{+16}_{-14}%
80%	80^{+16}_{-15}%
90%	90^{+10}_{-15}%
100%	100^{+0}_{-16}%

For each distribution from which we draw an observed sample (given in the first column and specified by the fraction of aligned systems in the distribution), we show the derived underlying distribution (see Section 8.5.3 and Fig. 8.3 for details). The population of $\sin i_\star$ measurements expected from the pre-selected TESS targets accurately recovers the correct distribution.

A potential drawback to this technique is that the reported errors from the grid of KS tests are difficult to interpret in a standard way. To investigate how realistic the errors are, we also fit the observed cumulative distribution function (CDF) directly to a model CDF. For nodes in the observed CDF located at $(\hat{x}, \hat{y})$, the corresponding nodes in the model CDF are located at $(\hat{x}, y)$. The model CDF is taken to be a linear combination of aligned and

isotropic CDFs:

$$\boldsymbol{y}(\hat{\boldsymbol{x}}; f_{\rm al}) = \frac{1}{\beta}\Big(\alpha_1 f_{\rm al}\ \boldsymbol{y}(\hat{\boldsymbol{x}}; 1) + \alpha_0(1 - f_{\rm al})\ \boldsymbol{y}(\hat{\boldsymbol{x}}; 0)\Big);$$
$$\beta = \alpha_1 f_{\rm al} + \alpha_0(1 - f_{\rm al}), \tag{8.8}$$

where the α terms are weight parameters to account for more obliquities being measured in aligned distributions, and β is simply the normalization. We fit to minimize χ^2, with errors for the observed CDF at a given $\sin i_\star$ value assigned to be proportional to the square root of the $\sin i_\star$ PDF (equivalent to counting statistics), and scaled so that $\chi^2_{\rm red} = 1$. The 1-σ errors from this direct fit, corresponding to the central 68.3% highest probability density region, are typically about ± 0.09. These errors roughly correspond to the errors one would get from the KS grid by assuming the 1-σ region is well-described by $p > 0.317$. We therefore conclude that our reported errors are, if anything, conservative. We choose to retain the larger errors, as potential systematics in our method (discussed in Section 8.6) may reduce accuracy for real observations.

Based on these simulations, we conclude that the expected yield of projected obliquity measurements from TESS will enable identification of the likely true obliquity distribution for hosts of planets of all sizes. In our example—motivated by migration processes that might be expected to produce a bimodal distribution of obliquities (i.e., aligned or isotropic, depending on the migration mechanism or lack thereof)—TESS obliquities should determine the fraction of systems drawn from a well-aligned distribution to within $\sim$0.15. The results of such an analysis holds insight into the relative importance of various proposed formation

and migration mechanisms.

8.6 Applications and Improvements

While we have demonstrated the value of the IPR technique using precise Gaia distances and angular diameters (rather than estimated linear radii) for TESS transiting planets, it can easily be applied to other surveys and other types of systems. For example, *Kepler* systems can be examined almost immediately upon release of Gaia distances, as the planets and rotation periods have already been identified (with occurrence and detection rates well-understood), $v \sin i_\star$ measurements have already been made, and broadband photometry exists for most stars in the field. Similarly, as the 2-wheeled *Kepler* mission (K2) continues to survey the ecliptic plane, the requisite data should become available. Furthermore, the all-sky TESS FFIs should enable detection of *more* planets than will observations of the pre-selected target stars (see S15). Observations will be more difficult for these fainter stars, and measurement errors will be larger, but these samples should eventually contribute significantly to constraints on host star obliquities.

One caveat is that to apply IPR in the manner we have presented—to constrain the underlying obliquity distribution—one needs to understand the target sample and detection probabilities well enough to simulate an accurate stellar and planetary population. In addition, a large observing program would need to be undertaken to obtain high signal-to-noise, high resolution spectra of the planet hosts with known rotation periods in order to measure $v \sin i_\star$ (and $T_{\rm eff}$ for calculating Θ via $F_{\rm bol}$). Much of this data already exists for *Kepler*

targets (and now K2 targets), and has been provided by the *Kepler* team and members of the broader exoplanet community as part of the Community Follow-up Observing Program (CFOP[3]), but additional uncertainties may be introduced by the multiple instruments used and widely varying quality of the spectra. Ideally, a large observing program dedicated to the task would be carried out on a single suitable instrument, but relying on community efforts may again be more realistic.

As for applying IPR to individual systems, the sky-plane projected obliquities have been measured for many hot Jupiters via the Rossiter–McLaughlin effect, and combination with the line-of-sight projection via IPR should, in some cases, provide the true obliquity, especially when using precise Gaia distances and angular diameters rather than radius estimates from stellar models.

It should also be noted that the orientation of angular momenta is an interesting diagnostic not only for short-period transiting planets. The same method can be used for eclipsing binaries, or even for non-transiting planets or debris disk systems. Directly imaged planet hosts, for example, tend to be bright, young, large, and nearby, all of which improve the measurements needed for IPR: young stars tend to rotate more rapidly (leading to precise $v \sin i_\star$) and with larger amplitudes (leading to easy $P_{\rm rot}$ detection), and their brightness, size, and proximity make them easily resolvable. While the orientation of the planet or disk is not limited to an edge-on orientation as is the case for transiting systems, if a planet shows an orbital arc, its orbital inclination can be constrained, and one could therefore probe angular momenta in planetary populations at wide separations. Similarly, debris disk orientation in

[3] `https://cfop.ipac.caltech.edu`

relation to the stellar spin axis can constrain the primordial alignment in planetary systems.

Though the potential applications of IPR are exciting, the biggest hurdles will be improving measurement precision (thereby improving individual system obliquity determinations as well as the power of population analyses) and eliminating systematic uncertainties that might bias our results. In most cases, $v \sin i_\star$ is the limiting factor because slow rotation is difficult to measure precisely. Using ultra-high resolution spectrographs could reduce the error contributions from $v \sin i_\star$ (although this would increase observing costs), as could analysis techniques developed specifically for precise $v \sin i_\star$ determination, which hasn't typically been a goal in the exoplanet literature. Such improvements may also justify inclusion of more slowly rotating stars in our sample, perhaps down to 1.5 or 1.0 $\mathrm{km\,s^{-1}}$, leading to a larger sample of obliquities around a wider range of spectral types, and therefore a more powerful, less biased population analysis. Making use of extremely precise distances and color-angular diameter relations, stellar radius measurements can already be delievered to within $\sim$5%, but using the full energy distribution to calculate the bolometric flux should in principle be better—careful development of this technique should also improve IPR. For TESS stars, rotation period measurements will be limited in most pointings to $< 30\,\mathrm{days}$ (and will not be precisely determined unless multiple periods are observed), but long period rotational variables can be identified and followed up from the ground to obtain rotation periods since the stars will be so bright. This can again expand the sample for improved analysis.

As measurement precisions increase, the method presented herein to constrain the true obliquity distribution of exoplanets will likely be limited by systematic uncertainties in the

assumptions made while simulating $\sin i_\star$ distributions (e.g., that gyrochronology can predict rotation periods, or that macroturbulence can be accounted for correctly using $T_{\rm eff}$–$\log g$–$v_{\rm mac}$relations). That is, we have compared simulated observed and expected measurements *under the same assumptions*. If our assumptions contain a systematic bias, this is removed by comparing it against itself, but an analysis that compares against real observations will inherit that bias. In particular, differential rotation, macroturbulence, and stellar rotational evolution remain complicating (potentially systematic) factors. If typical spot latitudes and differential rotation strength can be well-characterized as a function of stellar properties, errors associated with rotation can be mitigated. Similarly, if characterization of macroturbulence as a function of stellar properties continues to improve, we can eliminate additional systematics in $v \sin i_\star$ measurements. The study of gyrochronology (and departures from standard spin-down laws) remains a very active area of study, further enabled by the same space missions with which we search for planets. Continued improvements in these areas of stellar astrophysics will benefit many areas of study, including that of planetary system architectures.

8.7 Summary

Measurements of the obliquities of the hosts of short-period giant planets have proven invaluable to the interpretation of their orbital evolution—the wide range of obliquities that has been observed is suggestive of an active dynamical past for the migrating planets and/or primordial planet-forming system. Initial results for small planets suggest that these systems

are more likely than their larger counterparts to be flat, perhaps suggestive of a different dominant migration mechanism or in situ formation. However, comparatively little is known about the spin-orbit alignment for small planets—a large sample of obliquities for small planet hosts could lend strong evidence to the debate over in situ formation, the prevalence of primordially tilted disks, and the importance of wide companions in producing significant obliquity. We have presented a method to obtain such a sample by measuring the stellar inclinations of TESS planet hosts. To do so, we take advantage of an improvement in radius measurements made possible by precise distances that will be released by Gaia and angular diameters measured directly via interferometry or estimated from broadband photometry. Our simulations indicate that an analysis like the one presented here should be able to differentiate relatively finely between possible underlying obliquity distributions. In the example provided—in which the underlying distribution is modeled as a mixture of a fraction $f_{\rm al}$ aligned systems and $(1 - f_{\rm al})$ randomly oriented systems—we expect an uncertainty in the derived aligned fraction of only $\sigma_{f_{\rm al}} \sim 0.15$.

This technique will also be applicable to *Kepler* planets, results from K2 and ground-based surveys, eclipsing binaries, and directly imaged planets and disks, though it will be most useful as a population analysis for large samples. Finally, we point out that the power of this method can be improved by making precise measurements of $v \sin i_\star$, by furthering our understanding of stellar rotation and macroturbulence, and by carefully calibrating angular diameters derived from photometry.

CHAPTER 9
DISCUSSION

9.1 Summary of Key Ideas and Results

In this dissertation, we have discussed three complementary projects aimed at understanding planetary formation and migration. The main project, our radial-velocity survey for planets in adolescent open clusters, aimed to provide a constraint on whether the dominant mode of hot Jupiter migration is "Type II" disk migration or high eccentricity migration via multi-body interactions. The former must happen within $\sim$10 Myr while there is still a gas disk and is expected to preserve circular orbits during migration. The latter may take hundreds of millions of years and requires the planet to reach very high eccentricities and circularize over time via tidal friction with the host star. The occurrence rates and properties of planets as a function of age can therefore constrain which migration channels are most important. The architectures of these hot Jupiter systems are also important. Disk migration does not require additional companions, but the stellar Kozai mechanism or planet-planet scattering only operate in the presence of multi-body systems. The properties of outer companions therefore hold clues to the migration of giant planets as well. The best time to observe these is early on, before gravitational interactions within the cluster might influence or disrupt the system.

We have surveyed 4 clusters younger than 1 Gyr for RV companions (Praesepe, the Hyades, Coma Berenices, and the Ursa Major moving group), including 244 stars that were observed at least once for a total of 1727 spectra with typical time spans of 2-4 years. While

these ∼600 Myr survey targets are too old to distinguish between mechanisms on the basis of the timescale required (both processes could have produced hot Jupiters in this time), planets at this age that were initially eccentric may not have had time to circularize yet—we call a planet that possesses this property "dynamically young"—and outer companions are likely to still be present. We detected two hot Jupiters in Praesepe and one in the Hyades, representing the first hot Jupiters in open clusters, discoveries that show that such planets do form and migrate in this relatively dense stellar environment. Our derived frequency of hot Jupiters in these two clusters is 2%, in very close agreement with the field after adjusting for the metallicity difference between the populations. We find that one of these planets, Pr0211b in Praesepe, is part of a multi-planet system—the first in a cluster—that also contains a highly eccentric giant planet on a wide orbit ($P > 10$ years), suggestive of migration via planet-planet scattering. Another of these planets, HD 285507b in the Hyades, is dynamically young and possesses a non-zero eccentricity, also suggestive of HEM. More concretely, we find that for field hot Jupiters, dynamically young systems are more likely than dynamically old systems to possess high eccentricities. (This result runs parallel to that of obliquity studies: hot Jupiters with long tidal timescales are more likely to have high obliquities, while other systems may have realigned via tidal interactions.) We interpret this to mean that most hot Jupiters initially possess high eccentricities and circularize over time. Type II migration will not consistently excite high eccentricities, so **we argue that many hot Jupiters migrate via HEM.**

In addition to three hot Jupiters and an outer planet, we detect three additional warm

and cold Jupiters, ranging in period from 44 to 1250 days. Two of these planets orbit the same star (CB0036), and it is likely that the moderately eccentric 44-day planet migrated via interaction with its highly eccentric outer companion. The case for this is bolstered by their orbital orientations, which match predictions for a stalled planetary Kozai migration mechanism thought to be responsible for a class of warm Jupiters. Finally, like the other two long-period planets, Pr0157b is highly eccentric, leading us to speculate that gravitational interactions with other stars in cluster are likely to excite high eccentricities in planetary systems; our observational evidence may be consistent with simulations that suggest planet-planet scattering can be induced at a higher rate in clusters due to stellar flybys. We summarize the currently known cluster planets in Table 9.1.

Table 9.1: Summary of Planets in Clusters

Cluster	Name	$M_p \sin i_\star$ ($M_{\rm Jup}$)	R_p ($R_\oplus$)	P (days)	Reference
Hot Jupiters					
Praesepe	Pr0201 b	$0.534^{+0.038}_{-0.043}$	···	$4.43631^{+0.00044}_{-0.00036}$	Quinn et al. (2012)
Praesepe	Pr0211 b	$1.955^{+0.055}_{-0.067}$	···	$2.146117^{+0.000018}_{-0.000019}$	Quinn et al. (2012)
Hyades	HD185507 b	0.917 ± 0.033	···	6.0881 ± 0.0018	Quinn et al. (2014)
M67	YBP1194 b	0.34 ± 0.05	···	6.958 ± 0.001	Brucalassi et al. (2014)
M67	YBP1514 b	0.40 ± 0.11	···	5.118 ± 0.001	Brucalassi et al. (2014)
Warm and Cool Jupiters					
Hyades	ϵ Tau b†	7.6 ± 0.2	···	594.9 ± 5.3	Sato et al. (2007)
NGC 2423	NGC 2423-3 b†	10.6 ± 1.0	···	714.3 ± 5.3	Lovis & Mayor (2007)
M67	SAND364 b†	1.54 ± 0.24	···	121.71 ± 0.31	Brucalassi et al. (2014)
Praesepe	Pr0211 c	7.79 ± 0.33	···	4850^{+4560}_{-1750}	Malavolta et al. (2016)
Praesepe	Pr0157 b	9.49 ± 0.66	···	1234 ± 11	This work
Coma Berenices	CB0036 b	2.49 ± 0.10	···	$43.831^{+0.039}_{-0.047}$	This work
Coma Berenices	CB0036 c	$2.7^{+1.5}_{-0.4}$	···	449^{+13}_{-12}	This work
Transiting Planets					
NGC 6811	Kepler-66 b	···	2.80 ± 0.16	17.815815 ± 0.000075	Meibom et al. (2013)
NGC 6811	Kepler-67 b	···	2.94 ± 0.16	15.72590 ± 0.00011	Meibom et al. (2013)
Hyades	K2-25 b	···	$3.43^{+0.95}_{-0.31}$	$3.484552^{+0.000031}_{-0.000037}$	Mann et al. (2016)

Note — † signifies that the host star is evolved.

The second project in this dissertation, an adaptive optics imaging search for stellar companions to known hot Jupiter hosts, is an excellent follow-up to the RV survey. While

our study of young planets and their eccentricities seems to indicate that HEM is important to the production of hot Jupiters, it is unclear whether interactions with planetary or stellar companions are the primary mode of migration among HEM mechanisms. Because stellar Kozai migration requires a stellar companion and induces large variations in a planet's orbital inclination, we predict that *if* Kozai is a significant driver of the evolution of the orbits of giant planets, then: (1) hot Jupiter hosts should be more likely than the average star to reside in a binary system, and (2) hot Jupiters in binaries should frequently display large misalignments between their orbital axis and the stellar spin axis. Our survey of 93 host stars detected at least one stellar companion in 45% of systems (42/93), and because the survey is not complete, we consider this a lower limit. Since only 44% of Sun-like field stars reside in multiple-star systems, we tentatively conclude that **hot Jupiter hosts have an elevated binary occurrence rate.** Second, we find evidence that the misalignment of hot Jupiters is correlated with the presence of a companion: 74% of misaligned hot Jupiters reside in binaries (only 30% of well-aligned planets reside in binaries), and only 42% of hot Jupiters in binaries are well-aligned (a whopping 82% of planets orbiting single stars are well-aligned). In other words, **most misaligned hot Jupiters are in binaries and most hot Jupiters in binaries are misaligned**. While alternate hypotheses could help explain these (preliminary) results, **we argue that the stellar Kozai mechanism plays an important role in giant planet migration**.

The final project discussed in this disseration is a simulation of measurements of the expected TESS planet discoveries, demonstrating a method to determine the line-of-sight

projected spin-orbit angle for small planets. We propose to use estimates of stellar angular diameters calibrated with measurements originating from the CHARA Array, precise distances from the Gaia mission, rotation periods from TESS light curves, and the projected rotation velocities of the host stars to measure the inclination of the stellar spin axis (compared to the edge-on planetary orbits). Through this work **we demonstrate in our simulations that by carrying out these suggested measurements and calculations, we will be able to discern the true obliquity distribution of small planets**, gaining insight into their formation and migration histories.

9.2 Future Work

While the above results mark progress toward a more complete understanding of planet formation, there are some obvious next steps for these projects as well as some logical extensions to additional science.

In open clusters, we have demonstrated that cluster planets are a valuable (and viable) field of study. Clusters have the potential to contribute to our understanding of planetary evolution in much the same way that they have been invaluable to advances in the field of stellar evolution, largely due to their known (young) ages. We can build upon the results presented here in a few simple ways. First, we should continue to monitor unsolved variables, as these are the most promising way to improve our planet yield. We can also continue to observe the constant stars with a sparse cadence for several more seasons to improve sensitivity to long periods (though not indefinitely, as we expect diminishing returns before

long, limited by instrument precision and stellar jitter). These two observing programs, both of which we intend to pursue, would help characterize the cluster giant planet population at long periods. This would provide an additional comparison point for the field population, which would shed light upon the impact of the dynamical environment on planetary systems, and we also note that this population is the reservoir from which hot Jupiters originate, so characterizing long period giant planets would help place the hot Jupiter results in the proper context. It is appropriate to mention here that since our discoveries, three more cluster planets (two hot Jupiters orbiting Sun-like stars and a 121-day planet around an evolved star) have been announced in the near-Solar-age open cluster M67 (Brucalassi et al. 2014). These planets bolster the evidence that occurrence rates are similar in clusters and the field, but because they are much older, do not contribute directly to migration constraints. Older clusters can help, however, with studying the effect of environment on planetary systems (which can indirectly affect migration, e.g., through the transient gravitational perturbations of passing stars). In this same vein, we are mindful that the entire envionment in which the planet resides can impact its behavior; while we have already detected outer planetary companions to two of our cluster planets, understanding the full system architectures can help distinguish more finely between migration mechanisms (as we have seen from our AO survey). To that end, it would be worthwhile to carry out a deep high-resolution imaging survey of our cluster stars, though particularly those already known to host planets. This is work for which we have already submitted observing proposals.

Thus far, our RV survey has been limited to adolescent clusters, but even younger planets

would place stronger constraints on migration timescales, and would be more likely to be dynamically young. Given that the sample of dynamically young hot Jupiters is still small, each new discovery in the population is still important. We have already expanded our RV survey to include ∼100 single members of the 125 Myr Pleiades cluster, and even younger clusters such as α Persei may provide more opportunity to continue this work. A complication is that younger stars are more rapidly rotating, more active, and more heavily spotted, which degrades precision and increases the incidence of (high-amplitude) spot-induced RV signals that can mimic planets. One solution would be to carry out a survey in the infrared, where the contrast between spot and photosphere is minimized and spot amplitudes are lower. Such a survey could be run as a complement to visible wavelengths (e.g., to follow up candidates), or it could replace the optical survey. Cluster planets need not be studied only with radial velocities, of course. Transiting giant planets in clusters would immediately become benchmark objects for studying planetary physical evolution—e.g., atmosphere, temperature, and interior structure—given their precisely known ages, radii, masses, host star compositions, and dynamical environments. Space-based transit surveys are best poised to answer this call, with NASA's Kepler and K2 missions already revealing three smaller planets in clusters, including two mini-Neptunes in NGC 6811 (Meibom et al. 2013) and one in the Hyades (Mann et al. 2016), and it is likely that there are more to come. NASA's TESS mission will further the cause by surveying nearly the full sky for transits. Finally, we note that in the longer term, next generation extremely large telescopes will provide observational access to more distant clusters in order to expand sample sizes.

To extend the work presented here on the adaptive optics imaging survey of hot Jupiter hosts, the first step will be to finish the analysis described in Chapter 7—first and foremost to derive quantitative contrast curves and calculate the J and K magnitudes of the companions. We will also carefully consider alternative explanations for the correlations we observe, for example by testing the subsamples for biases in quantities that are known to correlate with binarity and spin-orbit misalignment, such as stellar mass. Additional AO imaging could also prove useful: observation of our detected binaries at later epochs can confirm via common proper motion that these are bound companions. More interestingly, measurement of orbital motion in the companions could constrain the relative directions of the angular momentum vectors of the planets and the binary companions, particularly in conjunction with precise RVs (see, e.g., Dupuy et al. 2016). Also of use would be the observation of control samples of stars without giant planets—or with giant planets that have not migrated inward—using the same instrumental setup to enable more direct comparisons of binary occurrence rates between hot Jupiter hosts and field stars. Finally, we recommend adaptive optics observations of all newly discovered hot Jupiter systems and the continued pursuit of measurements of their spin-orbit angles to improve population statistics.

The future path of our work on small planet obliquities is readily apparent, as we have demonstrated a method to measure the distribution—now someone must carry out those measurements. As we noted in Chapter 8, this will most likely be a community effort, though we intend to push that effort forward by obtaining high resolution spectra of TESS hosts, implementing state-of-the-art techniques for measuring $v \sin i_\star$ from those spectra, refining the

estimate of angular diameters via colors by carefully considering reddening corrections, and identifying systems for which ground-based photometric follow-up can significantly improve uncertainties on measured rotation periods.

REFERENCES

Adams, E. R., Ciardi, D. R., Dupree, A. K., Gautier, III, T. N., Kulesa, C., & McCarthy, D. 2012, AJ, 144, 42

Adams, F. C., & Laughlin, G. 2003, Icarus, 163, 290

——. 2006, ApJ, 649, 1004

Albrecht, S., Winn, J. N., Butler, R. P., Crane, J. D., Shectman, S. A., Thompson, I. B., Hirano, T., & Wittenmyer, R. A. 2012a, ApJ, 744, 189

Albrecht, S. et al. 2012b, ApJ, 757, 18

Ammler-von Eiff, M., & Guenther, E. W. 2009, A&A, 508, 677

An, D., Terndrup, D. M., & Pinsonneault, M. H. 2007, ApJ, 671, 1640

Bailey, III, J. I., White, R. J., Blake, C. H., Charbonneau, D., Barman, T. S., Tanner, A. M., & Torres, G. 2012, ApJ, 749, 16

Ballard, S., & Johnson, J. A. 2014, ArXiv e-prints

Barnes, J. R., Jeffers, S. V., & Jones, H. R. A. 2011a, MNRAS, 412, 1599

Barnes, J. W., Linscott, E., & Shporer, A. 2011b, ApJS, 197, 10

Barnes, J. W., van Eyken, J. C., Jackson, B. K., Ciardi, D. R., & Fortney, J. J. 2013, ApJ, 774, 53

Batalha, N. M. et al. 2013, ApJS, 204, 24

Bate, M. R., Lodato, G., & Pringle, J. E. 2010, MNRAS, 401, 1505

Batygin, K., & Adams, F. C. 2013, ApJ, 778, 169

Beatty, T. G., & Gaudi, B. S. 2015, PASP, 127, 1240

Beaugé, C., & Nesvorný, D. 2012, ApJ, 751, 119

Bergfors, C. et al. 2013, MNRAS, 428, 182

Bertin, E., & Arnouts, S. 1996, A&AS, 117, 393

Bieryla, A. et al. 2015, AJ, 150, 12

Bodenheimer, P., Laughlin, G., & Lin, D. N. C. 2003, ApJ, 592, 555

Boesgaard, A. M., Armengaud, E., & King, J. R. 2003, ApJ, 583, 955

Boss, A. P. 1998, Annual Review of Earth and Planetary Sciences, 26, 53

Bouvier, J., Covino, E., Kovo, O., Martin, E. L., Matthews, J. M., Terranegra, L., & Beck, S. C. 1995, A&A, 299, 89

Bouvier, J., Duchêne, G., Mermilliod, J.-C., & Simon, T. 2001, A&A, 375, 989

Boyajian, T. et al. 2015, MNRAS, 447, 846

Boyajian, T. S., van Belle, G., & von Braun, K. 2014, AJ, 147, 47

Broeg, C. et al. 2013, in European Physical Journal Web of Conferences, Vol. 47, European Physical Journal Web of Conferences, 03005

Brucalassi, A. et al. 2014, A&A, 561, L9

Bryan, M. L. et al. 2012, ApJ, 750, 84

Buchhave, L. A. et al. 2010, ApJ, 720, 1118

——. 2014, Nature, 509, 593

Buchhave, L. A., & Latham, D. W. 2015, ApJ, 808, 187

Buchhave, L. A. et al. 2011, ApJS, 197, 3

——. 2012, Nature, 486, 375

Carpenter, J. M., Mamajek, E. E., Hillenbrand, L. A., & Meyer, M. R. 2006, ApJ, 651, L49

Carter, J. A. et al. 2012, Science, 337, 556

Casewell, S. L., Jameson, R. F., & Dobbie, P. D. 2006, MNRAS, 365, 447

Chaplin, W. J. et al. 2013, ApJ, 766, 101

Chiang, E., & Laughlin, G. 2013, MNRAS, 431, 3444

Claret, A., Hauschildt, P. H., & Witte, S. 2012, A&A, 546, A14

Cochran, W. D., Hatzes, A. P., & Paulson, D. B. 2002, AJ, 124, 565

Collier Cameron, A. 2007, Astronomische Nachrichten, 328, 1030

Collier Cameron, A., Bruce, V. A., Miller, G. R. M., Triaud, A. H. M. J., & Queloz, D. 2010, MNRAS, 403, 151

Collier Cameron, A. et al. 2009, MNRAS, 400, 451

Cosentino, R. et al. 2012, in Proc. SPIE, Vol. 8446, Ground-based and Airborne Instrumentation for Astronomy IV, 84461V

Crockett, C. J., Mahmud, N. I., Prato, L., Johns-Krull, C. M., Jaffe, D. T., Hartigan, P. M., & Beichman, C. A. 2012, ApJ, 761, 164

Cumming, A., Butler, R. P., Marcy, G. W., Vogt, S. S., Wright, J. T., & Fischer, D. A. 2008, PASP, 120, 531

D'Angelo, G., Lubow, S. H., & Bate, M. R. 2006, ApJ, 652, 1698

Dawson, R. I. 2014, ApJ, 790, L31

Dawson, R. I., & Chiang, E. 2014, Science, 346, 212

Dawson, R. I., & Murray-Clay, R. A. 2013, ApJ, 767, L24

Dawson, R. I., Murray-Clay, R. A., & Johnson, J. A. 2015, ApJ, 798, 66

de Bruijne, J. H. J. 2012, Ap&SS, 341, 31

de Bruijne, J. H. J., Allen, M., Azaz, S., Krone-Martins, A., Prod'homme, T., & Hestroffer, D. 2015, A&A, 576, A74

Debes, J. H., & Jackson, B. 2010, ApJ, 723, 1703

Delorme, P., Collier Cameron, A., Hebb, L., Rostron, J., Lister, T. A., Norton, A. J., Pollacco, D., & West, R. G. 2011, MNRAS, 413, 2218

Désert, J.-M. et al. 2011, ApJS, 197, 14

Desort, M., Lagrange, A.-M., Galland, F., Udry, S., & Mayor, M. 2007, A&A, 473, 983

Dong, S., Katz, B., & Socrates, A. 2014, ApJ, 781, L5

Dotter, A., Chaboyer, B., Jevremović, D., Kostov, V., Baron, E., & Ferguson, J. W. 2008, ApJS, 178, 89

Doyle, A. P., Davies, G. R., Smalley, B., Chaplin, W. J., & Elsworth, Y. 2014, MNRAS, 444, 3592

Doyle, L. R. et al. 2011, Science, 333, 1602

Dressing, C. D., & Charbonneau, D. 2013, ApJ, 767, 95

——. 2015, ApJ, 807, 45

Dumusque, X. 2014, ApJ, 796, 133

Dupuy, T. J., Kratter, K. M., Kraus, A. L., Isaacson, H., Mann, A. W., Ireland, M. J., Howard, A. W., & Huber, D. 2016, ApJ, 817, 80

Eisner, J. A., Plambeck, R. L., Carpenter, J. M., Corder, S. A., Qi, C., & Wilner, D. 2008, ApJ, 683, 304

ESA, ed. 1997, ESA Special Publication, Vol. 1200, The HIPPARCOS and TYCHO catalogues. Astrometric and photometric star catalogues derived from the ESA HIPPARCOS Space Astrometry Mission

Fabrycky, D., & Tremaine, S. 2007, ApJ, 669, 1298

Fabrycky, D. C. et al. 2014, ApJ, 790, 146

Fang, J., & Margot, J.-L. 2012, ApJ, 761, 92

Fűrész, G. 2008, PhD thesis, University of Szeged, Hungary

Fielding, D. B., McKee, C. F., Socrates, A., Cunningham, A. J., & Klein, R. I. 2015, MNRAS, 450, 3306

Fischer, D. A., & Valenti, J. 2005, ApJ, 622, 1102

Ford, E. B. 2004, PASP, 116, 1083

——. 2008, AJ, 135, 1008

Ford, E. B., & Rasio, F. A. 2008, ApJ, 686, 621

Fressin, F. et al. 2013, ApJ, 766, 81

Gáspár, A., Rieke, G. H., Su, K. Y. L., Balog, Z., Trilling, D., Muzzerole, J., Apai, D., & Kelly, B. C. 2009, ApJ, 697, 1578

Gehrels, N. 1986, ApJ, 303, 336

Girardi, L., Bressan, A., Bertelli, G., & Chiosi, C. 2000, A&AS, 141, 371

Girardi, L., Groenewegen, M. A. T., Hatziminaoglou, E., & da Costa, L. 2005, A&A, 436,

895

Goldreich, P., & Tremaine, S. 1980, ApJ, 241, 425

Gray, D. F. 2013, AJ, 146, 29

Gray, D. F., & Baliunas, S. L. 1997, ApJ, 475, 303

Groot, P. J. 2012, ApJ, 745, 55

Haisch, Jr., K. E., Lada, E. A., & Lada, C. J. 2001, ApJ, 553, L153

Hambly, N. C., Steele, I. A., Hawkins, M. R. S., & Jameson, R. F. 1995, MNRAS, 273, 505

Hansen, B. M. S., & Murray, N. 2012, ApJ, 751, 158

Hartman, J. D. et al. 2009, ApJ, 695, 336

Hirano, T., Sanchis-Ojeda, R., Takeda, Y., Narita, N., Winn, J. N., Taruya, A., & Suto, Y. 2012, ApJ, 756, 66

Hirano, T., Sanchis-Ojeda, R., Takeda, Y., Winn, J. N., Narita, N., & Takahashi, Y. H. 2014, ApJ, 783, 9

Howell, S. B., Everett, M. E., Sherry, W., Horch, E., & Ciardi, D. R. 2011, AJ, 142, 19

Huber, D. et al. 2013, ApJ, 767, 127

——. 2012, MNRAS, 423, L16

Irwin, J. M. et al. 2011, ApJ, 742, 123

Jones, J. et al. 2015, ApJ, 813, 58

Jones, M. I., Jenkins, J. S., Bluhm, P., Rojo, P., & Melo, C. H. F. 2014, A&A, 566, A113

Jurić, M., & Tremaine, S. 2008, ApJ, 686, 603

Kennedy, G. M., & Kenyon, S. J. 2008, ApJ, 673, 502

King, J. R., Villarreal, A. R., Soderblom, D. R., Gulliver, A. F., & Adelman, S. J. 2003, AJ, 125, 1980

Knutson, H. A. et al. 2014, ApJ, 785, 126

Kozai, Y. 1962, AJ, 67, 591

Kraus, A. L., & Hillenbrand, L. A. 2007, AJ, 134, 2340

Kraus, A. L., Ireland, M. J., Huber, D., Mann, A. W., & Dupuy, T. J. 2016, ArXiv e-prints

Kuzuhara, M. et al. 2013, ApJ, 774, 11

Lai, D., Foucart, F., & Lin, D. N. C. 2011, MNRAS, 412, 2790

Latham, D. W. et al. 2011, ApJ, 732, L24

Latham, D. W., Stefanik, R. P., Mazeh, T., Mayor, M., & Burki, G. 1989, Nature, 339, 38

Latham, D. W., Stefanik, R. P., Torres, G., Davis, R. J., Mazeh, T., Carney, B. W., Laird, J. B., & Morse, J. A. 2002, AJ, 124, 1144

Law, N. M. et al. 2014, ApJ, 791, 35

Lidov, M. L. 1962, Planet. Space Sci., 9, 719

Lin, D. N. C., Bodenheimer, P., & Richardson, D. C. 1996, Nature, 380, 606

Lin, D. N. C., & Papaloizou, J. 1986, ApJ, 309, 846

Liu, F., Yong, D., Asplund, M., Ramírez, I., & Meléndez, J. 2016, MNRAS, 457, 3934

Lovis, C., & Mayor, M. 2007, A&A, 472, 657

Lubow, S. H., & Ida, S. 2010, Planet Migration, ed. S. Seager, 347–371

Luhman, K. L. 2014, ApJ, 786, L18

Mahmud, N. I., Crockett, C. J., Johns-Krull, C. M., Prato, L., Hartigan, P. M., Jaffe, D. T.,

& Beichman, C. A. 2011, ApJ, 736, 123

Maiorca, E., Randich, S., Busso, M., Magrini, L., & Palmerini, S. 2011, ApJ, 736, 120

Malavolta, L. et al. 2016, A&A, 588, A118

Mamajek, E. E., & Hillenbrand, L. A. 2008, ApJ, 687, 1264

Mandel, K., & Agol, E. 2002, ApJ, 580, L171

Mandushev, G. et al. 2011, ApJ, 741, 114

——. 2005, ApJ, 621, 1061

Mann, A. W. et al. 2016, ApJ, 818, 46

Marois, C., Macintosh, B., Barman, T., Zuckerman, B., Song, I., Patience, J., Lafrenière, D., & Doyon, R. 2008, Science, 322, 1348

Marois, C., Zuckerman, B., Konopacky, Q. M., Macintosh, B., & Barman, T. 2010, Nature, 468, 1080

Martin, R. G., & Livio, M. 2013, MNRAS, 434, 633

Mayor, M. et al. 2011, ArXiv e-prints

Mayor, M., & Queloz, D. 1995, Nature, 378, 355

Mazeh, T., Perets, H. B., McQuillan, A., & Goldstein, E. S. 2015, ApJ, 801, 3

McLaughlin, D. B. 1924, ApJ, 60

McQuillan, A., Mazeh, T., & Aigrain, S. 2014, ApJS, 211, 24

Meibom, S. et al. 2011, ApJ, 733, L9

——. 2013, Nature, 499, 55

Mermilliod, J.-C., Mayor, M., & Udry, S. 2009, A&A, 498, 949

Mochejska, B. J. et al. 2006, AJ, 131, 1090

Morton, T. D., & Winn, J. N. 2014, ApJ, 796, 47

Muirhead, P. S. et al. 2015, ApJ, 801, 18

Naoz, S. 2016, ArXiv e-prints

Naoz, S., Farr, W. M., & Rasio, F. A. 2012, ApJ, 754, L36

Nesterov, V. V., Kuzmin, A. V., Ashimbaeva, N. T., Volchkov, A. A., Röser, S., & Bastian, U. 1995, A&AS, 110

Ngo, H. et al. 2015, ApJ, 800, 138

Nidever, D. L., Marcy, G. W., Butler, R. P., Fischer, D. A., & Vogt, S. S. 2002, ApJS, 141, 503

Nordstroem, B., Latham, D. W., Morse, J. A., Milone, A. A. E., Kurucz, R. L., Andersen, J., & Stefanik, R. P. 1994, A&A, 287, 338

Nutzman, P. A., Fabrycky, D. C., & Fortney, J. J. 2011, ApJ, 740, L10

Ogilvie, G. I., & Lin, D. N. C. 2004, ApJ, 610, 477

Orosz, J. A. et al. 2012, Science, 337, 1511

Pace, G., Pasquini, L., & François, P. 2008, A&A, 489, 403

Pasquini, L. et al. 2012, A&A, 545, A139

Patience, J., Ghez, A. M., Reid, I. N., & Matthews, K. 2002, AJ, 123, 1570

Patience, J., Ghez, A. M., Reid, I. N., Weinberger, A. J., & Matthews, K. 1998, AJ, 115, 1972

Paulson, D. B., Cochran, W. D., & Hatzes, A. P. 2004a, AJ, 127, 3579

Paulson, D. B., Saar, S. H., Cochran, W. D., & Henry, G. W. 2004b, AJ, 127, 1644

Paulson, D. B., Sneden, C., & Cochran, W. D. 2003, AJ, 125, 3185

Paulson, D. B., & Yelda, S. 2006, PASP, 118, 706

Pecaut, M. J., & Mamajek, E. E. 2013, ApJS, 208, 9

Pels, G., Oort, J. H., & Pels-Kluyver, H. A. 1975, A&A, 43, 423

Pepper, J., Stanek, K. Z., Pogge, R. W., Latham, D. W., DePoy, D. L., Siverd, R., Poindexter, S., & Sivakoff, G. R. 2008, AJ, 135, 907

Perryman, M. A. C. et al. 1998, A&A, 331, 81

——. 2001, A&A, 369, 339

Petigura, E. A., Marcy, G. W., & Howard, A. W. 2013, ApJ, 770, 69

Pont, F., Husnoo, N., Mazeh, T., & Fabrycky, D. 2011, MNRAS, 414, 1278

Queloz, D., Eggenberger, A., Mayor, M., Perrier, C., Beuzit, J. L., Naef, D., Sivan, J. P., & Udry, S. 2000, A&A, 359, L13

Queloz, D. et al. 2001, A&A, 379, 279

Quinn, S. N. et al. 2012, ApJ, 756, L33

——. 2014, ApJ, 787, 27

——. 2015, ApJ, 803, 49

Raghavan, D. et al. 2010, ApJS, 190, 1

Rasio, F. A., & Ford, E. B. 1996, Science, 274, 954

Rauer, H. et al. 2014, Experimental Astronomy, 38, 249

Reiners, A., Bean, J. L., Huber, K. F., Dreizler, S., Seifahrt, A., & Czesla, S. 2010, ApJ,

710, 432

Ricker, G. R. et al. 2014, in Proc. SPIE, Vol. 9143, Space Telescopes and Instrumentation 2014: Optical, Infrared, and Millimeter Wave, 914320

Röser, S., Schilbach, E., Piskunov, A. E., Kharchenko, N. V., & Scholz, R.-D. 2011, A&A, 531, A92

Rossiter, R. A. 1924, ApJ, 60

Saar, S. H., & Donahue, R. A. 1997, ApJ, 485, 319

Sanchis-Ojeda, R., Winn, J. N., Holman, M. J., Carter, J. A., Osip, D. J., & Fuentes, C. I. 2011, ApJ, 733, 127

Sato, B. et al. 2007, ApJ, 661, 527

Schlaufman, K. C. 2010, ApJ, 719, 602

Schultheis, M. et al. 2015, A&A, 577, A77

Shara, M. M., Hurley, J. R., & Mardling, R. A. 2016, ApJ, 816, 59

Shen, Y., & Turner, E. L. 2008, ApJ, 685, 553

Shporer, A., Brown, T., Mazeh, T., & Zucker, S. 2012, New A, 17, 309

Siverd, R. J. et al. 2012, ApJ, 761, 123

Socrates, A., Katz, B., Dong, S., & Tremaine, S. 2012, ApJ, 750, 106

Sozzetti, A., Torres, G., Charbonneau, D., Latham, D. W., Holman, M. J., Winn, J. N., Laird, J. B., & O'Donovan, F. T. 2007, ApJ, 664, 1190

Spalding, C., & Batygin, K. 2015, ApJ, 811, 82

Stassun, K. G., Pepper, J. A., Paegert, M., De Lee, N., & Sanchis-Ojeda, R. 2014, ArXiv

e-prints

Stauffer, J. R., Schultz, G., & Kirkpatrick, J. D. 1998, ApJ, 499, L199

Stern, R. A., Schmitt, J. H. M. M., & Kahabka, P. T. 1995, ApJ, 448, 683

Storch, N. I., Anderson, K. R., & Lai, D. 2014, Science, 345, 1317

Struve, O. 1952, The Observatory, 72, 199

Sullivan, P. W. et al. 2015, ApJ, 809, 77

Swift, J. J., Johnson, J. A., Morton, T. D., Crepp, J. R., Montet, B. T., Fabrycky, D. C., & Muirhead, P. S. 2013, ApJ, 764, 105

ten Brummelaar, T. et al. 2014, in Proc. SPIE, Vol. 9148, Adaptive Optics Systems IV, 91484Q

ten Brummelaar, T. A. et al. 2005, ApJ, 628, 453

ten Brummelaar, T. A. et al. 2012, in Proc. SPIE, Vol. 8447, Adaptive Optics Systems III, 84473I

Thies, I., Kroupa, P., Goodwin, S. P., Stamatellos, D., & Whitworth, A. P. 2011, MNRAS, 417, 1817

Torres, G., Fischer, D. A., Sozzetti, A., Buchhave, L. A., Winn, J. N., Holman, M. J., & Carter, J. A. 2012, ApJ, 757, 161

Torres, G., Konacki, M., Sasselov, D. D., & Jha, S. 2005, ApJ, 619, 558

Triaud, A. H. M. J. 2011, A&A, 534, L6

Triaud, A. H. M. J. et al. 2010, A&A, 524, A25

Tsantaki, M., Sousa, S. G., Santos, N. C., Montalto, M., Delgado-Mena, E., Mortier, A.,

Adibekyan, V., & Israelian, G. 2014, A&A, 570, A80

Valenti, J. A., & Piskunov, N. 1996, A&AS, 118, 595

van Altena, W. F. 1966, AJ, 71, 482

van Bueren, H. G. 1952, Bull. Astron. Inst. Netherlands, 11, 385

van Eyken, J. C. et al. 2012, ApJ, 755, 42

van Leeuwen, F. 2007, A&A, 474, 653

——. 2009, A&A, 497, 209

van Saders, J. L., & Gaudi, B. S. 2011, ApJ, 729, 63

Vaughan, A. H., Preston, G. W., & Wilson, O. C. 1978, PASP, 90, 267

Vogt, S. S. et al. 1994, in Proc. SPIE, Vol. 2198, Instrumentation in Astronomy VIII, ed. D. L. Crawford & E. R. Craine, 362

von Braun, K. et al. 2014, MNRAS, 438, 2413

Walkowicz, L. M., & Basri, G. S. 2013, MNRAS, 436, 1883

Walsh, K. J., Morbidelli, A., Raymond, S. N., O'Brien, D. P., & Mandell, A. M. 2011, Nature, 475, 206

Wang, J., Fischer, D. A., Xie, J.-W., & Ciardi, D. R. 2014, ApJ, 791, 111

Wang, J., & Ford, E. B. 2011, MNRAS, 418, 1822

Weiss, L. M. et al. 2013, ApJ, 768, 14

Welsh, W. F. et al. 2012, Nature, 481, 475

Winn, J. N., Fabrycky, D., Albrecht, S., & Johnson, J. A. 2010a, ApJ, 718, L145

Winn, J. N., & Fabrycky, D. C. 2015, ARA&A, 53, 409

Winn, J. N. et al. 2010b, ApJ, 723, L223

——. 2007, ApJ, 665, L167

Wolszczan, A., & Frail, D. A. 1992, Nature, 355, 145

Wright, J. T. et al. 2011, PASP, 123, 412

Wright, J. T., Marcy, G. W., Howard, A. W., Johnson, J. A., Morton, T. D., & Fischer, D. A. 2012, ApJ, 753, 160

Wu, Y., & Lithwick, Y. 2011, ApJ, 735, 109

Yi, S., Demarque, P., Kim, Y.-C., Lee, Y.-W., Ree, C. H., Lejeune, T., & Barnes, S. 2001, ApJS, 136, 417

Yoder, C. F., & Peale, S. J. 1981, Icarus, 47, 1

Yu, L. et al. 2015, ApJ, 812, 48

Zakamska, N. L., Pan, M., & Ford, E. B. 2011, MNRAS, 410, 1895